21654727

This is to certify that the

dissertation entitled

Finite Size Effects in Copper Manganese Spin Glasses

presented by

Gregory G. Kenning

has been accepted towards fulfillment
of the requirements for

Ph.D degree in Physics

J. A. Cowen
Major professor

Date Sept 16/88

O-12771

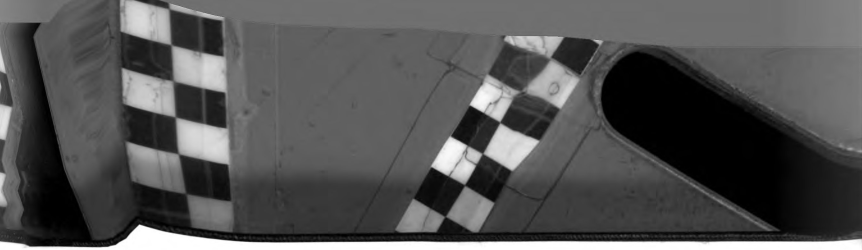

FINITE SIZE EFFECTS
IN
COPPER MANGANESE SPIN GLASSES

By

Gregory George Kenning

A DISSERTATION

Submitted to
Michigan State University
for the degree of

DOCTOR OF PHILOSOPHY

Department of Physics

1988

ABSTRACT

FINITE SIZE EFFECTS
IN
COPPER MANGANESE SPIN GLASSES

By

Gregory George Kenning

Using UHV sputtering we have produced $Cu_{1-x}Mn_x/Cu$ and $Cu_{1-x}Mn_x/Si$ multilayered systems (MS) with $x=$ .04, .07, and .14. Structural analysis of these systems including SAXD, EDX, SAD, imaging, high angle x-ray, and parallel resistivity confirm that these samples are layered and there is minimal chemical diffusion between the layers in the CuMn/Cu MS, but some intermixing of the layers in the CuMn/Si MS. We have shown that the 300 A^o Cu thickness used in the CuMn/Cu Ms and the 70 A^o of Si used in the CuMn/Si MS magnetically decouple the CuMn layers. By systematically decreasing the CuMn thickness (L_{CuMn}) we observe that the CuMn layers retain their spin glass properties to $L_{CuMn} \leq 20$ A^o. The spin glass transition temperature T_g (as defined by the DC magnetic susceptibility) begins to decrease from its bulk value T_g^b ($L_{CuMn} = 5000$ A^o) at $\approx 1000 A^o$ and approaches zero at $L_{CuMn} \approx 10$ A^o in the CuMn/Cu MS and $L_{CuMn} \approx 36$ A^o in the CuMn/Si MS. These results have been interpreted in terms of finite size scaling analysis, the droplet excitation model, and conduction electron mean free path effects. We believe that these results represent the first experimental observation that the Lower Critical Dimension (LCD) of CuMn spin glass systems is between two and three.

To my family, always.

ACKNOWLEDGEMENTS

I would like to thank Professor Jack Bass for his support and guidance during my term at Michigan State University.

I would like to thank Professor Jerry Cowen for his guidance and for many helpful discussions.

There were many other people who contributed to this thesis, either through helpful discussions or experimental assistance. Special thanks go to J. Slaughter for teaching me about sputtering. I would also like to thank A. R. Day, W. Repko, T. Kaplan, D. Leslie-Pelecki, L. Hoines, B. Leach, V. Schull, W. Abdul-Razzaq, D. Gregory and C. Bruch for their contributions.

Table of Contents

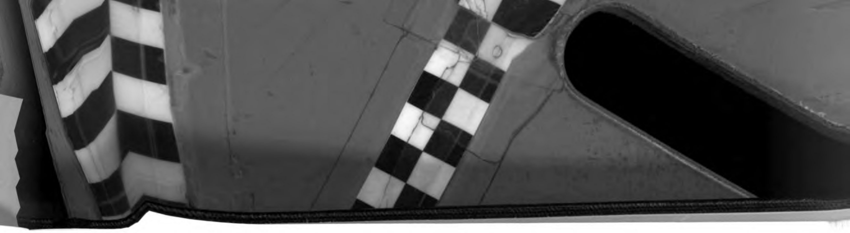

LIST OF TABLES

LIST OF FIGURES

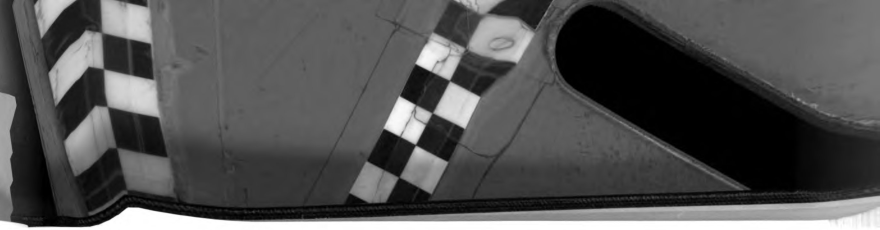

CHAPTER I

INTRODUCTION

Magnetic phase transitions have been one of the most intensely studied areas in condensed matter physics this century.[1,2] Experimentally, it has been found that most ordered ferromagnetic and anti-ferromagnetic materials have discontinuities in such important physical properties as their magnetic susceptibilities and specific heat at a well defined magnetic transition temperature.[3] In 1972 a type of disordered magnetic material termed a spin glass was found[4] to have a cusp in its' susceptibility vs temperature curve, at a temperature defined as the spin glass transition temperature T_g. In general these materials are spatially disordered alloys or insulators, composed of magnetic ions in a (generally) non-magnetic host. Several important physical properties such as the specific heat and resistivity show no anomalies at T_g. There is therefore some controversy[5] about the existence of a true phase transition and about the nature of the transition itself. Recent experiments on the non-linear part of the magnetic susceptibility have shown power law divergences, rather convincing evidence that the spin glass transition is a thermodynamic phase transition in three dimensions.

Great theoretical interest in effects of dimensionality on phase transitions[5,6,7], especially crossover effects in going from a higher dimension to a lower one have led

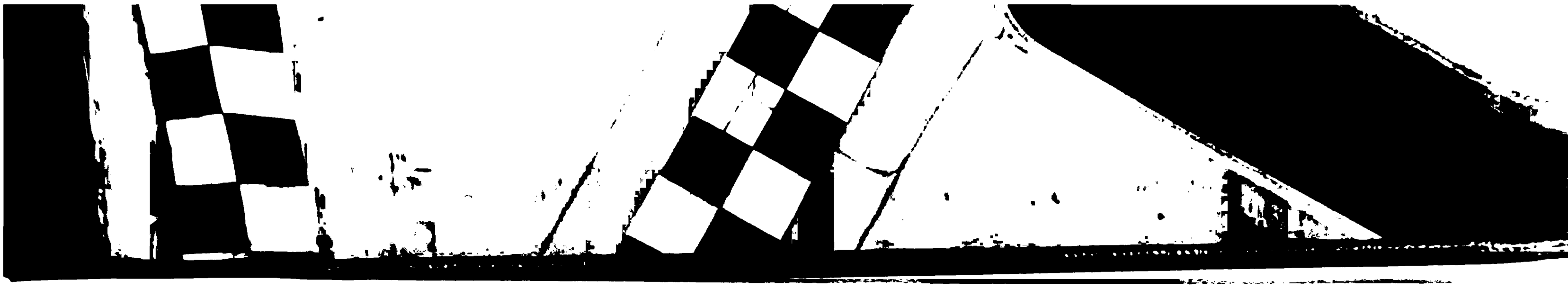

us to investigate how the spin freezing temperature T_g, and other properties of a spin glass (SG) change as the dimensionality is decreased from three to two. This study was stimulated by:

1) The desire to explore effects of finite sample size on a magnetic system with inherent spatial disorder.
2) The fact that a combination of experimental and theoretical evidence in 3D and 2D suggests that the lower critical dimension (ie. the dimension below which a phase transition no longer occurs at a finite temperature) for a phase transition in both Ising and Heisenberg like SG's with long range RKKY interactions is likely to lie between 2 and $3^{5,7}$.

Experimentally, SG's thus provide an almost unique opportunity to study both the static and dynamic behaviour across a lower critical dimension boundary, under conditions involving intrinsic spatial disorder. We have chosen CuMn SG materials to carry out this study for the following reasons:

1) These materials have spin glass properties over Mn concentrations of $40\ ppm \leq c \leq 30 percent$,corresponding to a wide range of transition temperatures T_g, between $\approx 10^{-4}K$ and $\approx 120K^8$.
2) CuMn is believed to be a Heisenberg SG system, with small spatial anisotropy, and RKKY coupling between the magnetic Mn ions.
3) The metallic nature of the CuMn alloy allows for DC sputtering.
4) CuMn has been the most intensely studied spin glass material.

In order to achieve magnetization signals large enough to measure with a SQUID susceptometer, we have had to produce Multilayer Systems (MS) in which many layers of CuMn spin glass films are separated by a decoupling medium such as Si, which is an insulator at low T, or a layer of Cu thick enough to decouple the layers magnetically (Fig. I-1). The advent of U.H.V. sputtering technology has made it feasable to produce high enough quality MS to study the spin glass transition of metallic spin glass films as the film thickness L_{CuMn} is decreased so that the film

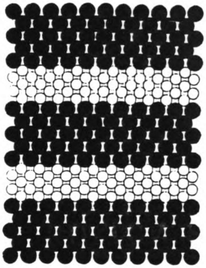

Figure I-1a: Multilayer System composed of alternating layers of crystalline materials.

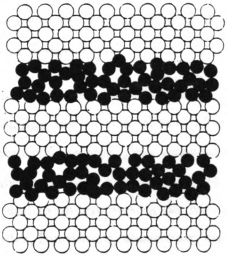

Figure I-1b: Multilayer System composed of alternating layers of crystalline and amorphous materials.

approaches a two dimensional state. We observed, for the first time, a dramatic decrease in the spin glass transition temperature from its bulk value of T_g^b to $T_g^L \rightarrow 0$ at film thicknesses, L, of only a few atoms (Fig. I-2), strongly suggesting that the lower critical dimension of this type of spin glass is between two and three. We can fit the shifted transition temperature, $T_g^b - T_g^L$, as a function of L_{CuMn} with a power law form suggestive of a thermodynamic phase transition and from this fit we have obtained a value of the universal correlation exponent ν. It is the purpose of this thesis to study the decrease in T_g, determine the associated critical exponents, and test for universality of these exponents as a function of Mn concentration.

The first step in understanding the sputtered CuMn/Cu and CuMn/Si MS is structural characterization of the layers and the layering. This includes determining layer thicknesses, crystal structure in the layers, and the amount of interfacial mixing between the CuMn layers and the decoupling layers (Cu and Si). Since we are changing a fundamental parameter of the system (ie. the dimensionality), other physical properties which help define the spin glass state (eg. hysteresis) are characterized to see if there are any fundamental changes in the SG other then the decrease in the transition temperature.

This chapter will be mainly concerned with outlining the experiments and concepts necessary for understanding the current picture of the spin glass state. It starts with a discussion of some of the spin glass materials, the defining experiments of the state, and then discusses some of the major physical concepts thought to be relevant to this thesis and to understanding the materials and experiments. These concepts include disorder, frustration, anisotropy, and lower critical dimension.

I.1) Materials

Spin glass behaviour has now been observed[8] in many different types of materials with different types of interactions. Non-metallic crystalline materials such as $Eu_xSr_{1-x}S$ show a cusp in the magnetic susceptibility, no long range order, time dependent effects, and have other physical properties typical of spin glass materials.

approaches a two dimensional state. We observed, for the first time, a dramatic decrease in the spin glass transition temperature from its bulk value of T_g^b to $T_g^L \rightarrow 0$ at film thicknesses, L, of only a few atoms (Fig. I-2), strongly suggesting that the lower critical dimension of this type of spin glass is between two and three. We can fit the shifted transition temperature, $T_g^b - T_g^L$, as a function of L_{CuMn} with a power law form suggestive of a thermodynamic phase transition and from this fit we have obtained a value of the universal correlation exponent ν. It is the purpose of this thesis to study the decrease in T_g, determine the associated critical exponents, and test for universality of these exponents as a function of Mn concentration.

The first step in understanding the sputtered CuMn/Cu and CuMn/Si MS is structural characterization of the layers and the layering. This includes determining layer thicknesses, crystal structure in the layers, and the amount of interfacial mixing between the CuMn layers and the decoupling layers (Cu and Si). Since we are changing a fundamental parameter of the system (ie. the dimensionality), other physical properties which help define the spin glass state (eg. hysteresis) are characterized to see if there are any fundamental changes in the SG other then the decrease in the transition temperature.

This chapter will be mainly concerned with outlining the experiments and concepts necessary for understanding the current picture of the spin glass state. It starts with a discussion of some of the spin glass materials, the defining experiments of the state, and then discusses some of the major physical concepts thought to be relevant to this thesis and to understanding the materials and experiments. These concepts include disorder, frustration, anisotropy, and lower critical dimension.

I.1) Materials

Spin glass behaviour has now bee ent types of materials
with different types of inte materials such as
$Eu_xSr_{1-x}S$ show a cusp range order, time
dependent effects, and b pin glass materials.

In this system magnetic Eu atoms ($J = \frac{7}{2}, g = 2$) placed randomly on an fcc lattice interact through direct ferromagnetic exchange with their nearest neighbors and antiferromagnetic exchange with their next nearest neighbors. Amorphous metallic and nonmetallic materials such as $Al_{.63}Gd_{.37}$ and $MnO \cdot Al_2O_3 \cdot SiO_2$ (respectively) also show spin glass properties. Although the magnetic interactions in these amorphous materials are not well understood, it is generally believed that a competition between ferro and antiferromagnetic bonds, coupled with a disordered array of magnetic ions, is essential in the formation of a spin glass state. This thesis will discuss only CuMn which is a long range metallic spin glass. Such materials are characterized by a concentration c of magnetic atoms (ie. Mn,Cr,Fe) randomly dispersed on a lattice of a metallic host (ie. Cu,Ag,Au) and interacting through long range, oscillatory RKKY exchange.

At very low concentrations, the magnetic impurities are far enough apart that they are non-interacting. This is called the Kondo[9] regime. For Mn in Cu this occurs when $c \leq 4$ ppm. At concentrations larger than this, the impurities interact through the long ranged oscillatory RKKY interaction which decays asymptotically as $\frac{1}{R^3}$[10] from the impurity ions. When the average energy of interaction becomes comparable to the ambient temperature, the local moments tend to "freeze out" in random directions. There is evidence[11] that this "freezing out" is a collective process corresponding to the growth in correlations of the spins. As the concentration is increased further the statistical probability of the magnetic atoms becoming nearest and next-nearest neighbors increases. The near neighbor position of Mn atoms in FCC Cu strongly favors antiferromagnetic alignment while the next nearest neighbor position favors ferromagnetic alignment[12]. X-ray studies[13], in AgMn, have shown that there is local chemical ordering which strongly prefers the next nearest neighbor position. It has been proposed[14] that ferromagnetic clustering occurs and that these clusters interact in much the same way as the individual magnetic ions in the dilute spin glass state. At a critical concentration $c_{crit} \approx 30$ percent, a percolation network of nearest neighbors occurs and the material becomes antiferromagnetic[8].

1.2) Experimental Properties

In 1972 Canella and Mydosh[4] made a series of low field ac susceptibility measurements on AuFe. They found a cusp in the susceptibility reminicent of a second order magnetic phase transition. This behaviour was subsequently found in other dilute magnetic alloys (CuMn,AuMn,etc) and also in some short range spin glasses (ie. EuSrS).[5] The non-linear terms in the ac susceptibility (ie. $M/H - \chi_1 = A\chi_3 + B\chi_5 + \ldots$) have been measured in AgMn by Levy and Ogielski[11]. They found that $\chi_3, \chi_5, \chi_7 \ldots$ diverge with an algebraic form $[\chi^n_{nonlinear} \sim (T - T_c)^{-n\gamma-(n-1)\beta}]$, and measured values of $\gamma = 2.1 \pm .1$ and $\beta = 0.9 \pm .2$. This divergence in the susceptibility, and hence in the free energy ($F = -\frac{\partial^2 \chi}{\partial H^2}$), is the most convincing evidence to date that the spin glass transition is a real thermodynamic phase transition.

Low field ac susceptibility vs. temperature curves are similar for spin glasses and anti-ferromagnets[4]. Below the transition temperature, ferro and anti-ferromagnetic materials show long range order as evidenced by Bragg peaks in neutron diffraction studies[15]. Until recently, no evidence of long range order below T_g had been observed in spin glasses, suggesting that the spins freeze out in random directions. Werner et. al.[16,17] have recently seen several satellite Bragg peaks in CuMn, suggesting magnetic ordering on the length scale of $40A^o$. They have attributed this ordering to a frustrated spin density wave in the Cu host. This work however is still in its infancy and the interpretation is dependent on several significant extrapolations in the data. Nonetheless the observation of possible ordering in CuMn is very interesting.

Since 1972, many measurements have been made of the specific heat of spin glass materials to look for evidence of a phase transition. To date, no discontinuities have been found in the zero field specific heat at the freezing temperature. The specific heat exhibits a broad peak about 20 percent higher than T_g [5]. It has been, argued[5], however that this does not necessarily rule out a phase transition. Several possibilities exist: 1) The transition may show up as a non-linear effect in the specific heat. 2) The width of the critical region may be very narrow and below present experimental resolution. These arguments have been used to explain the lack of a divergence in the specific heat at the Curie temperature of the dilute ferromagnet $Co_xZn_{1-x}(C_5H_5NO_6)(ClO_4)_2$ [18].

In 1976 Ford and Mydosh[19] measured the electrical resistivity of several long ranged spin glass materials. The resistivity difference between the pure host and the alloy

$$\Delta\rho(T) = \rho_{alloy}(T) - \rho_{host}(T)$$

has a broad peak at a temperature approximately twice the transition temperature. Within experimental error no indication of any significant change in $\Delta\rho(T)$ or $\frac{d\Delta\rho(T)}{dT}$ was observed at the transition temperature. They interpreted this behaviour to mean that there is no long range cooperative magnetic ordering.

Time dependent effects have been observed using different techniques to measure the relaxation times of individual spins and of the whole spin glass state. To measure the former, three different techniques (neutron echo[20,21], Mossbauer effect[22], and muon spin resonance (μSR)[23]) corresponding to different time scales ($10^{-12} \leq t \leq 10^{-8}, t \leq 10^{-7}, t \leq 10^{-5}$ respectively) have been used. The results suggest that the spin relaxation times increase rapidly near the critical temperature. These data have been fit[23] to a ln(t) dependence suggesting a gradually freezing glass-like system. The data can also be fit[24] to an algebraic form $t^{-\zeta}$ suggesting a phase transition. Several different methods have been used to measure time dependence of the spin glass state. Malozemoff and Imry[25] made susceptibility measurements on bulk CuMn and $Al_{.63}$ $Gd_{.37}$ on time scales from minutes to twenty four hours. They found no shift in the spin glass transition temperature over these time scales. The time scale of our susceptibility measurements vary from $10^2 - 10^3$ seconds per temperature point. The relaxation of the spin glass state below T_g has been observed[26] in the Thermoremnant Magnetization (TRM) (cooling in a field and then removing the field) and the Isothermal Remnant Magnetization (IRM) (cooling in

possibilities exist: 1) The transition may show up as a non-linear effect in the specific heat. 2) The width of the critical region may be very narrow and below present experimental resolution. These arguments have been used to explain the lack of a divergence in the specific heat at the Curie temperature of the dilute ferromagnet $Co_xZn_{1-x}(C_5H_5NO_6)(ClO_4)_2$ [18].

In 1976 Ford and Mydosh[19] measured the electrical resistivity of several long ranged spin glass materials. The resistivity difference between the pure host and the alloy

$$\Delta\rho(T) = \rho_{alloy}(T) - \rho_{host}(T)$$

has a broad peak at a temperature approximately twice the transition temperature. Within experimental error no indication of any significant change in $\Delta\rho(T)$ or $\frac{d\Delta\rho(T)}{dT}$ was observed at the transition temperature. They interpreted this behaviour to mean that there is no long range cooperative magnetic ordering.

Time dependent effects have been observed using different techniques to measure the relaxation times of individual spins and of the whole spin glass state. To measure the former, three different techniques (neutron echo[20,21], Mossbauer effect[22], and muon spin resonance (μSR)[23]) corresponding to different time scales ($10^{-12} \leq t \leq 10^{-8}, t \leq 10^{-7}, t \leq 10^{-5}$ respectively) have been used. The results suggest that the spin relaxation times increase rapidly near the critical temperature. These data have been fit[23] to a ln(t) dependence suggesting a gradually freezing glass-like system. The data can also be fit[24] to an algebraic form $t^{-\zeta}$ suggesting a phase transition. Several different methods have been used to measure time dependence of the spin glass state. Malozemoff and Imry[25] made susceptibility measurements on bulk CuMn and $Al_{.63}$ $Gd_{.37}$ on time scales from minutes to twenty four hours. They found no shift in the spin glass transition temperature over these time scales. The time scale of our susceptibility measurements vary from $10^2 - 10^3$ seconds per temperature point. The relaxation of the spin glass state below T_g has been observed[26] in the Thermoremnant Magnetization (TRM) (cooling in a field and then removing the field) and the Isothermal Remnant Magnetization (IRM) (cooling in zero field, applying a field for a short period of time, and then removing the field). These measurements show a dependence on the temperature, field, and the sample magnetic history suggesting that the zero field cooled (zfc) magnetization is not a thermal equilibrium state. The field cooled (fc) magnetization shows only weak time dependence leading the authors[26] to suggest that it is an equilibrium state.

Below the transition temperature hysteretic effects are observed[27] as a function of magnetic field (Fig. I-3, reproduced from ref. 27). The magnetization vs. magnetic field curve is a shifted symmetric loop with hysteretic behaviour. This behaviour is explained in terms of the Dzyaloshinskii Moriya (DM) and uniaxial anisotropies discussed in the next section.

There has been one experiment, that we are aware of, to observe cross-over behaviour between three and two dimensions in a spin glass system. Awschalom[28] has reported that the magnetic susceptibility cusp in CdMnTe rounds out and eventually disappears as L_{CdMnTe} is decreased below 80 A^o. He has interpreted this as evidence for an LCD of three in this type of spin glass. It has been pointed out[29] however that even in the spin glass state there is an antiferromagnetic correlation length of $\xi_{antiferromagnetic} \approx 100\ A^o$, [illegible] is in the same direction that the sample thickness was decreased. It is thus not clear that he has seen spin glass finite size effects, as opposed to effects due to the reduction of this antiferromagnetic correlation length.

I.3) Concepts

I.3.1) Disorder

Quenched spatial disorder, a property of all spin glasses, means that the magnetic atoms are fixed in space (substitutionally or interstitially) and are located randomly throughout the material. Experimentally, randomizing the material constituents is probably the biggest problem in the production of real spin glass systems. Ideally, disorder is achieved by a series of annealing treatments to thoroughly randomize

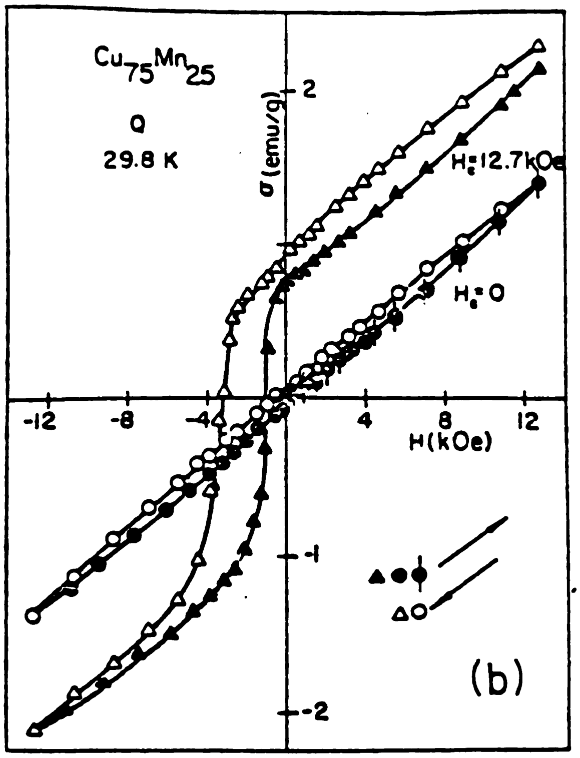

Figure I-3: Magnetization vs. Magnetic Field for CuMn with 25 percent Mn after field cooling (fc) and after after zero field cooling (zfc). (After Beck[27])

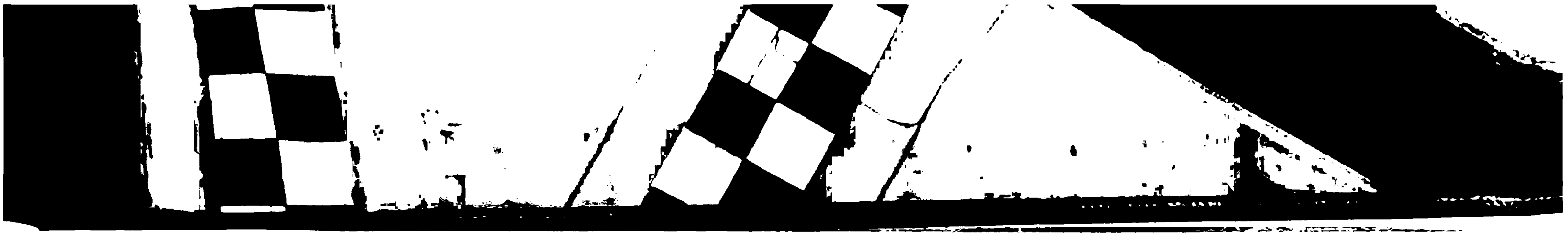

the alloy constituents and then quenching the sample to freeze in this disorder. For a more complete discussion of how we obtain spatially disordered samples see II.1. Incorporating disorder into spin glass theories is the main theoretical challenge in a comprehensive theory. This will be discussed in further detail in chapter III.

I.3.2) Frustration

Spatially disordered magnetic atoms coupled through a long range oscillatory exchange interaction leads to frustration. D.Sherrington[30] has described frustration as 'The global inability to simultaneously satisfy all local ordering requirements'. On a global energy scale frustration allows the possibility of a highly degenerate ground state. The evolution of the spin glass systems' free energy as a function of temperature is probably responsible for the observed time dependent effects[5] as the system seaches for its true equlibrium energy minima. On the macroscopic scale, frustration combined with spatial disorder produces an absence of long range magnetic order, and thus an apparent randomness of the spins.

The simplest example of a locally frustrated set of spins can be illustrated as follows:

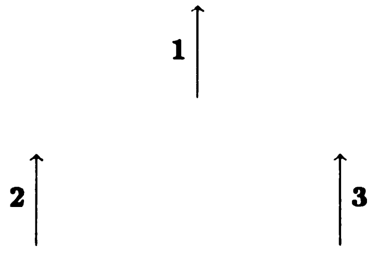

Consider a system of three spins with one degree of freedom (ie. up or down) all interacting antiferromagnetically. If spin 1 is up then spins 2 and 3 want to point down with respect to it. But spins 2 and 3 also want to point in opposite directions hence frustration. This example was given for an Ising model (one spin degree of freedom). In the case of a Heisenberg system (three spin degrees of freedom) it is easier to satisfy local energy requirements since the spins have more degrees of freedom. This lowers the tendency toward frustration in the system.

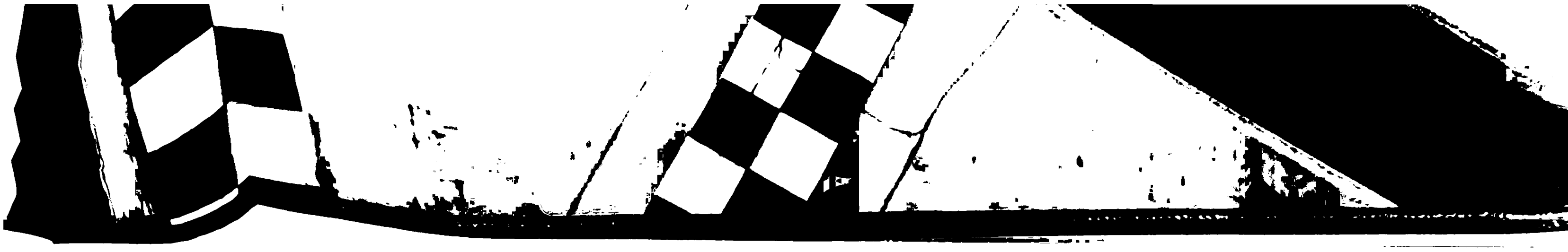

I.3.3) Anisotropy

There are other interactions which increase the amount of frustration by limiting the degrees of freedom of the individual spins, and which thus affect the formation of the spin glass state. These are the anisotropic interactions. Without anisotropic interactions CuMn is Heisenberg like which, early calculations suggested, had no phase transition in three dimensions[31]. With anisotropy, CuMn becomes more Ising like, which has been shown to have a phase transition in three dimensions[31]. The Dzyaloshinskii Moriya (DM) interaction is unidirectional in nature, coupling the spin directionality to the host lattice atoms through spin orbit scattering of a third atom[32,33]. Below the transition temperature, in an applied magnetic field, the DM interaction attempts to maintain the frozen in random spin alignment. This alignment can only be overcome with a reversed magnetic field, large enough to flip all of the by spins 180°. This "flipping" or coercive field (Fig.I-3) is equal to the displacement in a hysteresis loop[34] and in experiments where impurities are added to the SG material the coercive field is proportional to the impurity concentration and the strength of the impurity spin orbit coupling. Another anisotropy found in CuMn is uniaxial dipolar anisotropy, which is due to the direct magnetic coupling of the moments. As mentioned above, early theoretical calculations[31], have found that without a 'pseudo-dipolar' anisotropy the three dimensional Heisenberg spin glass does not 'order' (ie. have a phase transition); recent calculations suggest, however, that anisotropy may not be fundamental to the ordering of the Heisenberg spin glass[7].

I.3.4) Lower Critical Dimension (LCD)

The earliest calculations of systems undergoing phase transition have shown that the system dimensionality is a fundamental parameter of the phase transition. In his 1925 thesis[35], E. Ising showed that the one dimensional Ising model of a ferromagnet has no phase transition at a finite temperature (it was later shown[36] that there is a phase transition at T=0). Onsager[37] calculated, exactly, the solution to the Ising

model in two dimensions and found that it does support a finite temperature phase transition. Therefore the Lower Critical Dimension (LCD) of this system is said to be between one and two (ie. the dimension below which the system cannot support a phase transition at a nonzero temperature). The theoretical evidence which discusses the LCD of spin glass systems will be presented in Ch. III-1,2.

I.4) Thesis Outline

The rest of this thesis is organized as follows:

Chapter II is the experimental chapter. It is divided into three parts: The first part includes target production, a description of the sputtering facility, a description of an argon purification system that was designed and built to clean the Ar that is introduced into the sputtering chamber as part of the sputtering process, and a description of the sputtering process itself. The second part of chapter II discusses structural characterization of the MS. This includes small and large angle x-ray analysis, resistivity in both the 4-probe and Van de Pauw geometries, and various characterization techniques using a Field Emission-Scanning Transmission Electron Microscope (FE-STEM). The final section of this chapter is a synopsis of the structural characteristics of the CuMn/Cu and CuMn/Si MS.

Chapter III is the theoretical chapter. Theoretical calculations on SG models in three and two dimensions have been done within SG mean field theories; therefore the first section of chapter III is a description of SG mean field theories. This includes bond disorder models such as the Edwards-Anderson EA model and the Sherrington-Kirkpatric model, and site disorder models. The second section of this chapter outlines the uniform quenched model and the application of this model to the layered geometry. We used this model to try to understand the effect on the transition temperature of the diffusion of Si impurities into the CuMn layer. The final section of chapter III includes an introduction to scaling theory and progresses to the droplet-excitation model which has been used by Fisher and Huse to describe our results..

In Chapter IV we analyze the magnetic susceptibilities of our samples. The first section of this chapter describes the susceptibility data. The second section is an analysis of the susceptibility data in terms of finite size scaling, mean free path effects and the structural properties of our samples.

CHAPTER II

SAMPLE PREPARATION
AND
STRUCTURAL CHARACTERIZATION

The sample production goal of this thesis was to make as perfect as feasible Multilayered Systems MS using our sputtering system. The ideal sample would include no chemical mixing at the interface, perfectly planar interfaces, and single crystal layers, possibly with some lattice strain at the interface. The structural characterization experiments discussed in this chapter show that our samples have polycrystalline or amorphous layers, some chemical mixing at the interface, and irregular interface boundaries. Although the ideal MS is difficult to make by sputtering, an ideal sample is not essential to observe the important magnetic effects that are discussed in Chapter IV.

The first section of this chapter describes the target production, sputtering facility, sputtering, and sample production. The second section describes the experiments done to characterize the samples and an analysis of these experiments. The final part of this chapter is a synopsis of the inferred structural characteristics of the CuMn/Cu and CuMn/Si MS.

II.1) Sample Production

II.1.1) Target Production

The CuMn sputtering targets were produced from 6 $9'^s$ Cu and 4 $9'^s$ Mn melted into an alloy in a Lepel induction furnace. Selected amounts of each constituent were etched in nitric acid and then weighed to give approximately the desired composition. The metals to be alloyed were placed into a cylindrical graphite crucible of radius 6.5 cm. and depth 2 cm., which had first been coated with boron nitride to ensure that the carbon from the graphite didn't enter the target. The crucible with constituents was placed in a vycor enclosure inside the RF coils and pumped down to $\leq$ 2x10^{-6} torr. The graphite served as the active heating element.

As the holder was heated, the Cu melted at 1083°C and the Mn floated to the top. The Mn melted at 1244°C and the system was held at this temperature for approximately five minutes to ensure good mixing. The target was then cooled over several hours and turned on a lathe to a radius of 5.7 cm, the correct size for the sputtering machine. Before use, the target was cleaned in alcohol and then sputtered for several minutes to remove any iron that may have entered the surface during the latheing process. After sputtering, it was found that the target was composed of CuMn crystallites of diameter approximately 2 cm in the middle of the target and approximately 0.5 cm near the edge of the target. Four different concentrations of $Cu_{1-x}Mn_x$ targets were made: x=.04, .07, .14, and .21.

Two methods were used to more closely establish the alloy compositions. Shavings from the lathe were sent away for chemical analysis. Chemical analyses of the same sample, by the same company (Galbraith Laboratories Inc.), yielded markably different results. Chemical analysis of a sample sent to a different company (Schwarzkopf Microanalytical Laboratory) gave a total percentage of constituents significantly larger than 100 percent. We therefore, had limited faith in these results. Our main method of determining the Mn concentration in the targets was to compare the bulk (shavings) spin glass transition temperature T_g with the known

T_g vs. concentration curve Fig. II-1. Results from this analysis are listed in Table II-1.

The Si target was commercially made from 6 9's Si which had a room temperature resistivity much greater than 10 Ω-cm. The semiconducting properties of this target allowed for D.C. sputtering at room temperature.

II.1.2.) Sputtering

II.1.2.1.) The Sputtering Gas

Sputtering is the emission[38] of surface atoms of a target by bombarding it with radiation, generally particle radiation. In our case we use Ar^+ ions to bombard the target, removing several atoms of target material for every incoming Ar ion.

Sputtering is done in a cylindrical stainless steel tank of height 48 cm and radius 23 cm. Four L.M. Simard 'Tri-Mag' sputtering sources are mounted 90^o from each other, on a circle of radius 14 cm.. The sputtering sources sputter ions towards the top of the tank onto substrates mounted on the Substrate Positioning and Monitoring Apparatus (SPAMA), 4" above the sputtering targets. The SPAMA holds eight substrate holders containing two substrates each. Two samples of each MS are made simultaneously; one for structural characterization, one for susceptibility measurements. To make MS, the SPAMA is positioned alternately over two sputtering sources by a stepping motor which is controlled by an IBM PC. The sputtering tank is pumped down to $\leq 2x10^{-8}$ torr first using a mechanical roughing pump and then a CTI cryo-torr8 cryopump. The pressure in the tank is then raised to $2.5x10^{-3}$ torr by introducing Ar into the system through the sputtering guns. The upper limit of the gaseous impurity percent per monolayer deposited by this system, for a sputtering rate of 10 A^o/s, has been estimated to be 1.7 percent[39].

Prior to entering the guns, the ultra-pure Ar is further cleaned by passing through a cold trap to be discussed next, and then through a Hydrox [MAT] gas purifier

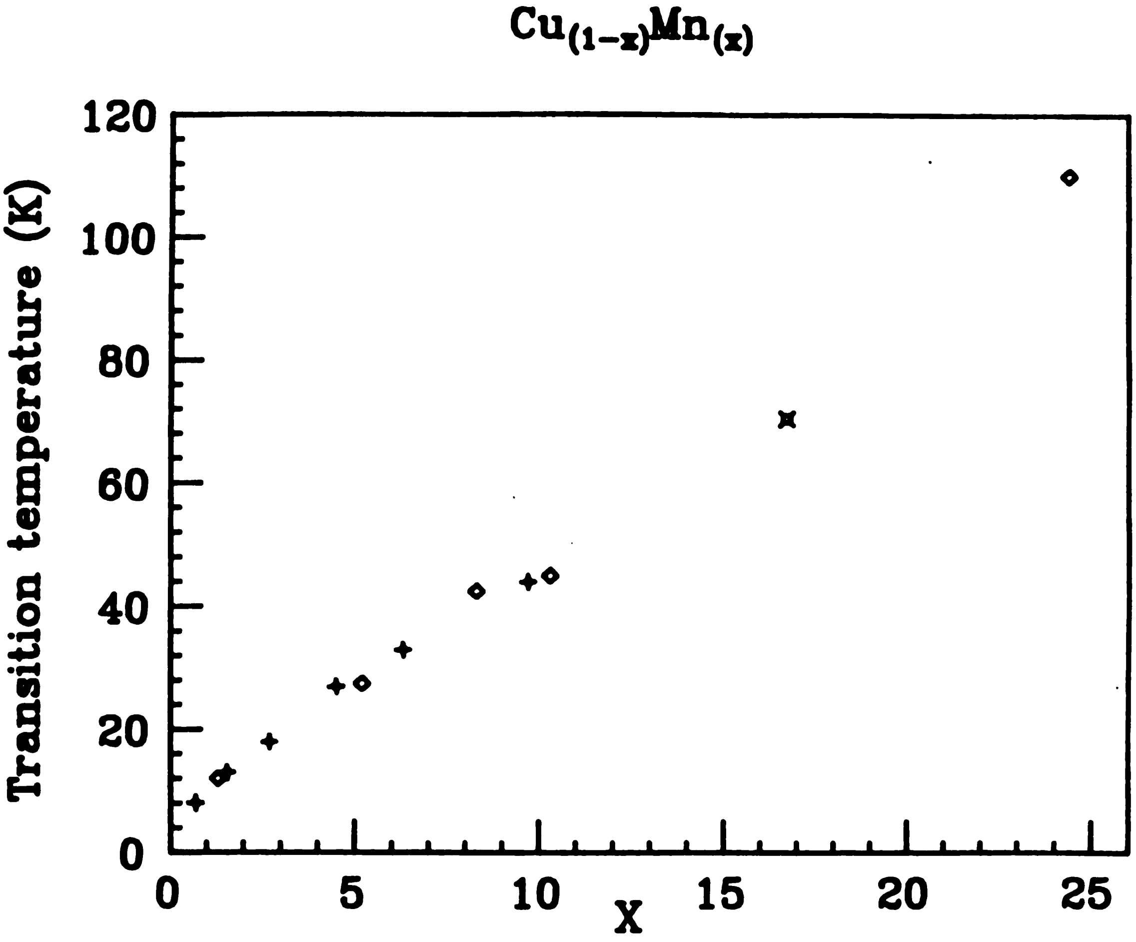

Figure II-1: Transition temperature vs. Mn concentration in bulk CuMn alloys. Compiled from the Landolt-Bornstein tables[40].

Table II-1 Comparison of methods used to establish target composition.

Target 1	Elements	Percent
Nominal constituent composition	Cu	96
	Mn	4
Chemical Analysis*	Cu	93.34
	Mn	3.51
	C	.078
From Fig. II-1	Mn	4±1
Target 2		
Nominal constituent composition	Cu	90
	Mn	10
Chemical Analysis*	1) Cu	90.61
	Mn	6.03
	C	.005
	2) Cu	93.43
	Mn	6.39
	3) Cu	93.1
	Mn	6.72
From Fig. II-1	Mn	7±1
Target 3		
Nominal constituent concentration	Cu	85
	Mn	15
From Fig. II-1	Mn	14±1
Target 4		
Nominal constituent composition	Cu	75
	Mn	25
Chemical Analysis@	Cu	76.69
	Mn	29.45
	C	.02
From Fig. II-1	Mn	21±2

* Galbraith
@ Schwarzkopf

which removes impurities such as O_2 and N_2 by reacting with a hot Ti filament. The Ar gas then passes through a flow controller into the gun assembly. For a more complete discussion of the sputtering tank, SPAMA, flow controllers and gun assembly see J. Slaughter, thesis[39].

II.1.2.1.1.) The Trap and Temperature Controller

To remove impurities from the Ar gas entering the sputtering chamber, and increase the lifetime of the Ti purifier, an Ar purification system was constructed. This system has two parts: A trap which is kept a few degrees above the liquid N_2 boiling temperature to freeze out H_2O and other impurities, and a temperature control system which controls the temperature at the bottom of the trap with an accuracy of ±1 K.

A diagram of the Ar trap is shown in Fig. II-2. The trap is made entirely of Cu to ensure good thermal contact with the N_2 bath. As the boiling temperature of Ar, 87.3 K[41], is 10 K higher then the boiling temperature of N_2, 77 K, it necessary to always keep the trap at least 11 K above the N_2 boiling point. Ar enters the trap through a 1/2" stainless steel tube and flows down through to the bottom of the trap. Simple calculations based on a flow rate of 120 cc/s of Ar at a pressure of 760 torr show that no significant deviation from the input pressure occurs in this tube, and that the Ar is cooled to within a few degrees of the trap temperature by the time it leaves the input pipe. The trap is filled with Ag and Cu shavings to provide a large surface area for impurity atoms to plate out on. The Ar then leaves the trap by way of another 1/2" stainless steel tube located at the top of the trap.

A feedback temperature controller was constructed to ensure that the incoming Ar never drops below its boiling temperature. A schematic of the controller is shown in Fig. II-3. The heater generates a maximum of 12 watts continous power. The sensing thermocouple is located at the side of the trap. The distance between the heater and the sensing themocouple gives the feedback loop an approximately two minute time constant. With three liters of N_2 in the N_2 reservoir, the system is

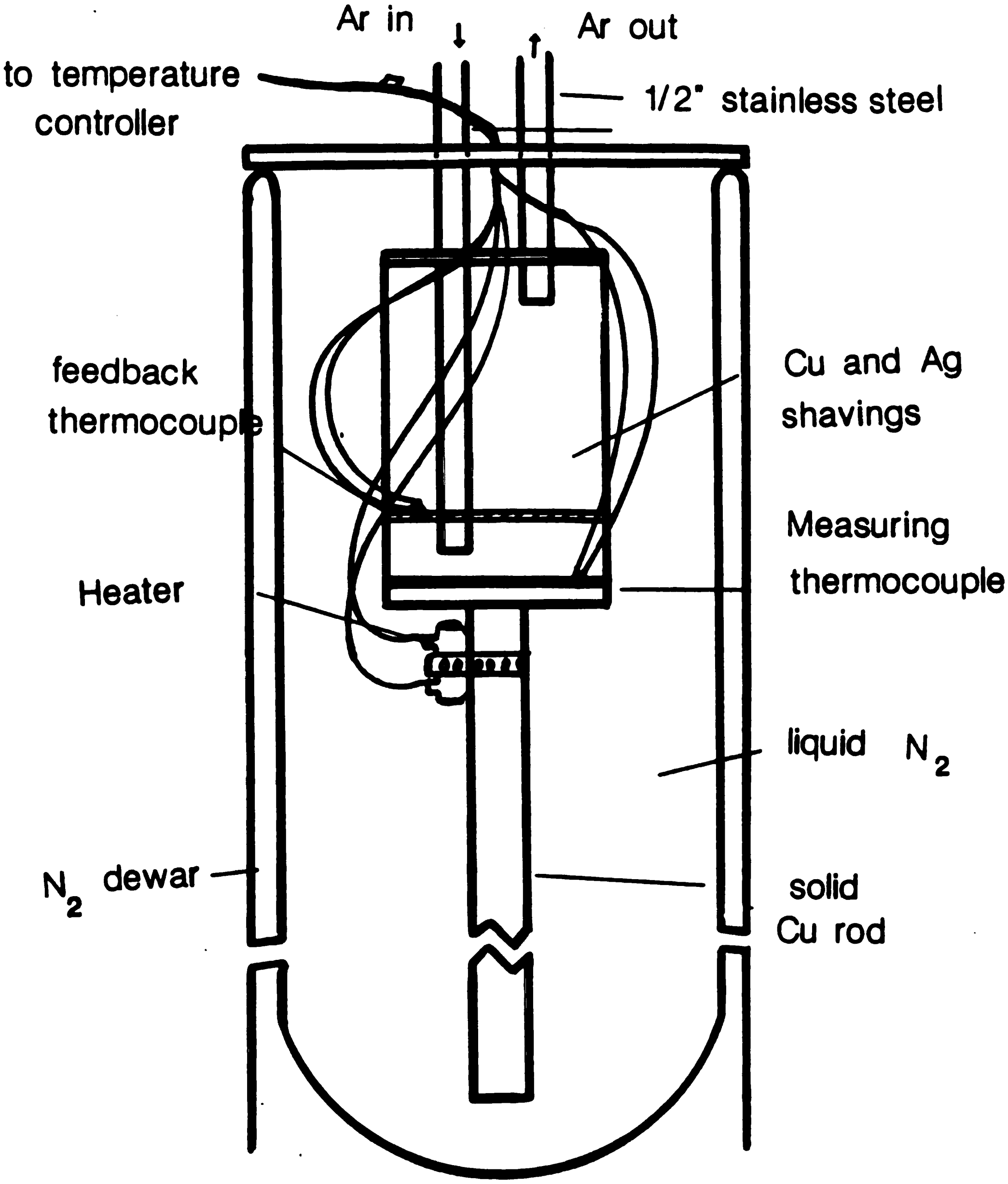

Figure II-2: Cold trap for purifying Ar gas.

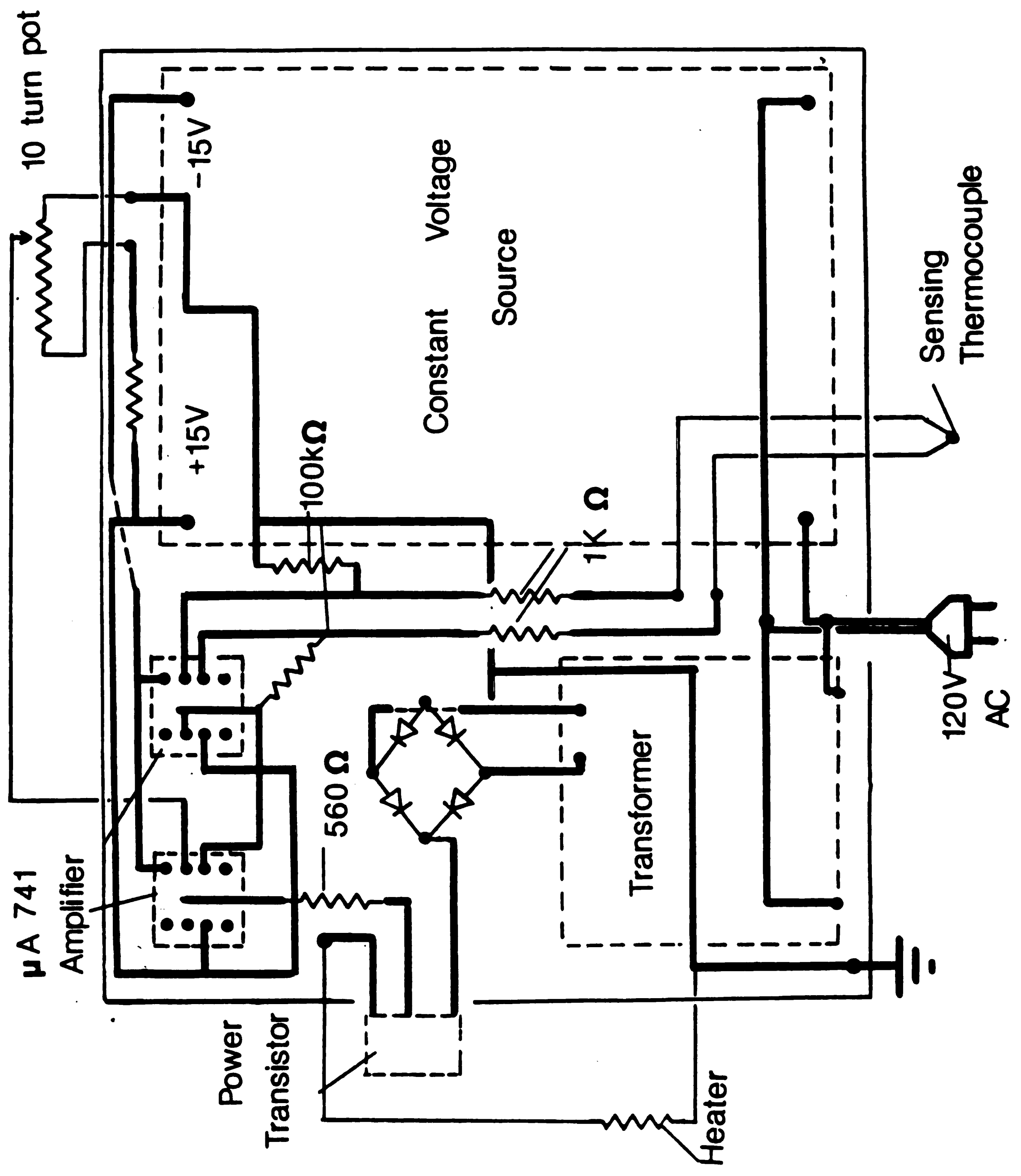

Figure II-3: Circuit diagram of the feedback temperature controller.

able to maintain a temperature of between 88-100 K, depending on the variable set point, to within an error of ± 1 K, for about four hours.

II.1.2.2.) Sputtering Process

To create an Ar plasma, a current is passed through the Ar flowing over the target. The target is then lowered to a negative potential, which causes the positive Ar ions to accelerate and bombard it. To make our samples, the guns were programed to produce incoming Ar ions with kinetic energies in the range 250-400 eV for sputtering CuMn and Cu, and 300 eV for sputtering the Si target. This is enough energy to knock several atoms out of the target per incoming ion, Fig. II-4. Keeping the surface of the Si substrates cool was the main criteria which determined sputtering gun parameters. We found that if the Ar energies or total flux of sputtered atoms were too large, the samples were annealed (ie no layering was observed with SAXD, see II.2.1). Ideal sputtering parameters for making MS were found by trial and error. The theoretical curve in Fig. II-4 is based on a collision cascade model of sputtering[42]. The incoming Ar ion collides with a surface target atom, which collides with other target atoms in a collision cascade. Some of this cascade momentum returns to the surface atoms through elastic collisions. If the surface atoms recover kinetic energy sufficient to overcome their binding energy they eject from the surface, Fig. II-5. Sputtering rates are therefore inversely proportional to the surface binding energy and proportional to the incoming Ar energy.

Preferential sputtering of one type of target atom over another type of target atom, in alloyed targets is possible if the binding energies of the different types of sputtered atoms are different. We infer from the comparison of the spin glass transition temperatures of target shavings and 'bulk' (5000 A^o) sputtered films that little or no preferential sputtering has occurred.

The magnetic atoms in a spin glass should be randomly located throughout the material. We believe that we have achieved this in our samples through the randomization of the sputtering process, and by keeping the substrates as cool as

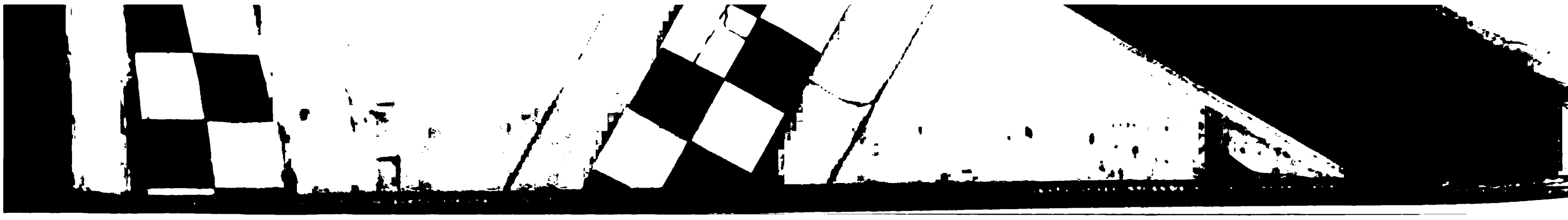

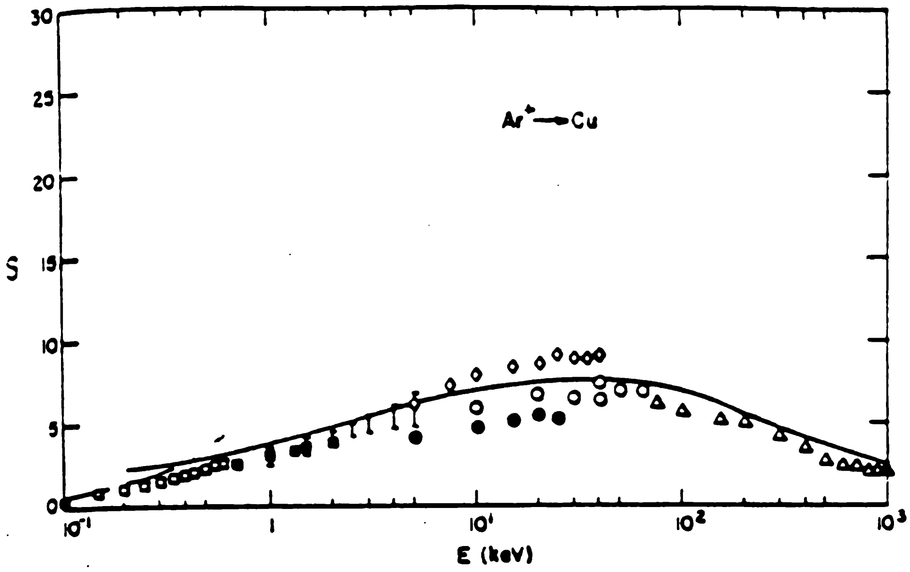

Figure II-4a: Measured and calculated sputtering rates of Cu as a function of incoming Ar energies. S is the number of sputtered atoms per incoming Ar atom. From Sigmund[42].

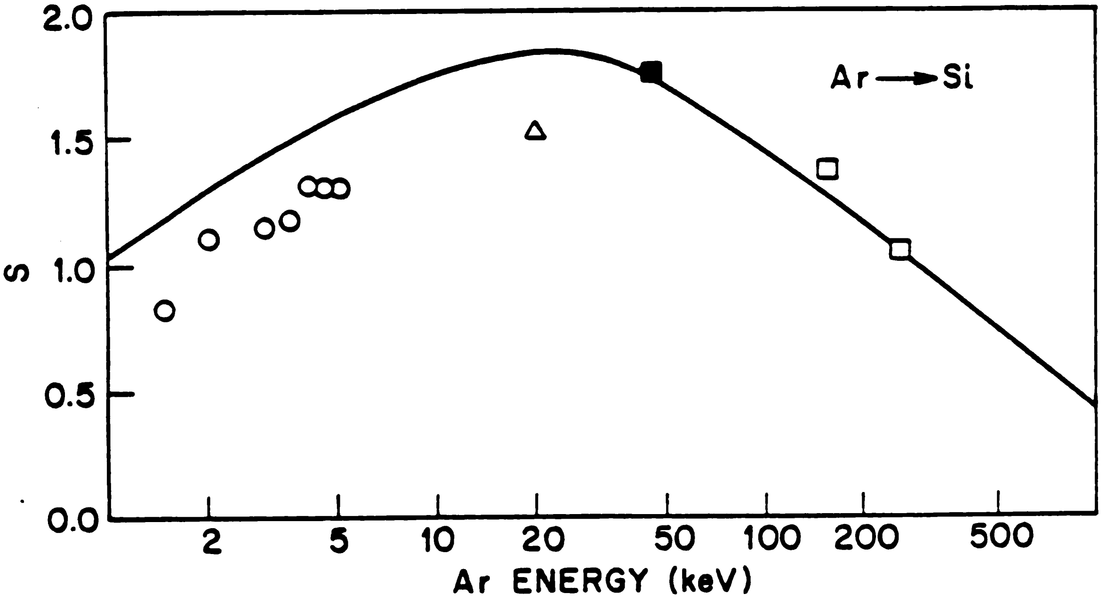

Figure II-4b: Mesured and calculated sputtering rates of Si as a function of incoming Ar ion. S is the number of sputtered atoms per incoming Ar atom. From Sigmund[42].

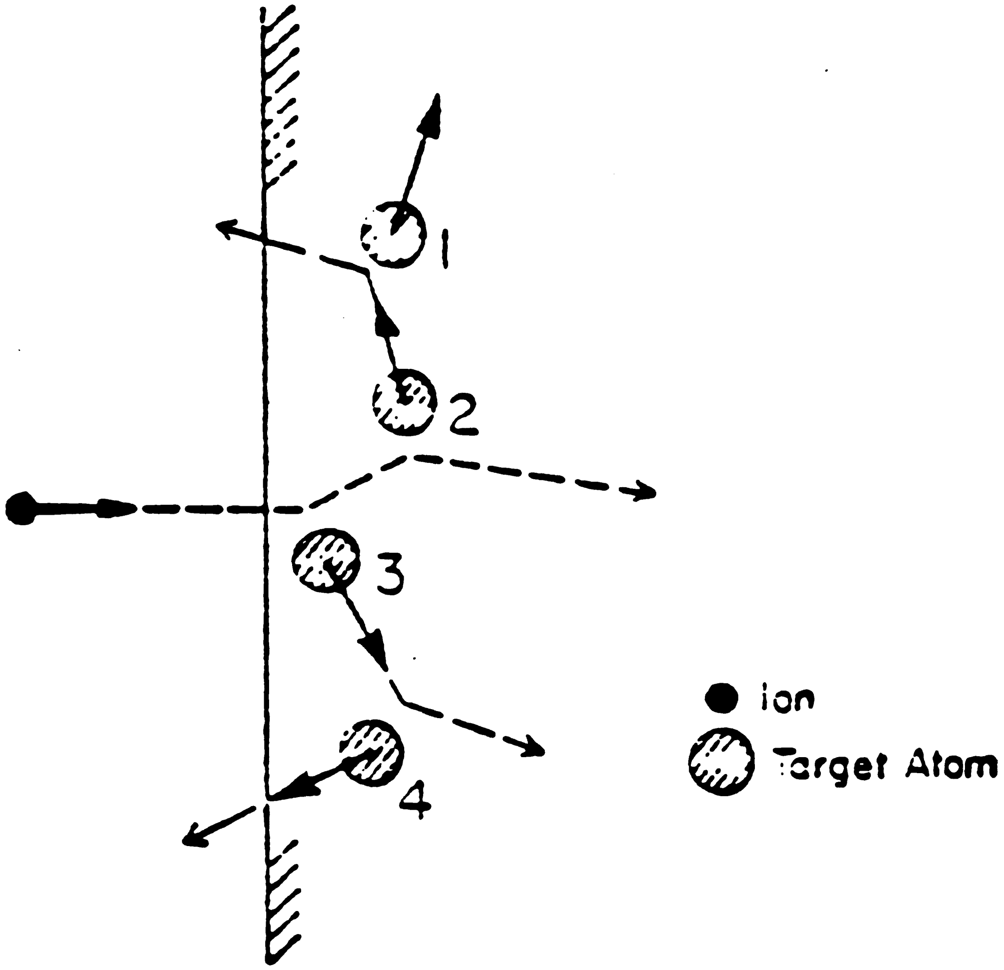

Figure II-5: Diagram of the sputtering process.

possible to minimize movement of the sputtered atoms on the substrate. In our system the sputtered atoms are focussed through a chimney assembly onto room temperature substrates located about 4" above the target. As the sputtered atoms deposit their energies on the substrates, the substrate temperature increases. In order to keep the substrates as cool as possible, only one or two samples were made at a time and then the system was allowed to cool for several hours.

The sputtering rates were determined using Temescal FTM-3000 quartz crystal film thickness monitors (FTM), which could be lowered into the substrate positions 4" over the guns. The geometry of the sputtering system only allows measurement of the sputtering rates prior to or directly after making a sample. Desired layer thicknesses in the MS are programed into the software which controls the stepping motor attached to the substrate plate. The stepping motor positions the substrate over an individual gun for a prescribed amount of time corresponding to the required thickness. Typical sputtering rates were $1-3\ A^o/s$ for the Si target and $12-16\ A^o/s$ for the CuMn and Cu targets.

The substrates used in these studies were the [100] and [111] faces of Si, single crystal sapphire, and cleaved NaCl. All substrates except the NaCl were cleaned in the following manner. The substrates were:

1) Wiped with alcohol and visual observation was used as an aid to remove spots.
2) Cleaned for ten minutes in Alconox detergent in an ultrasonic cleaner.
3) Cleaned for ten minutes in distilled water in the ultrasonic cleaner.
4) Cleaned for ten minutes in alcohol in an ultrasonic cleaner.

II.2) Structural Characterization

We characterized the structural properties of our samples in several different ways. Small Angle X-ray Diffraction (SAXD) was used to determine the average bi-layer thickness. Cross-sections of the MS $\sim 500 A^o$ thick were made for Field Emission-Scanning Transmission Electon Microscope (FE-STEM) analysis[43,44]. Imaging of

these cross-sections and Energy Dispersive X-rays (EDX) helped determine the integrity of the layering. Selected Area Diffraction (SAD) and high angle x-ray studies were done to analyze the structure of the layers. The resistivities of our samples were measured for two reasons:

1) To determine whether the thin films and metallic layers were continuous.
2) To determine the extent to which interfacial mixing deposited impurities in the higher conductivity layers of the MS.

II.2.1.) Small Angle X-ray Diffraction (SAXD)

SAXD was used as a tool to confirm the layered structure of our samples and to measure the bi-layer thickness. SAXD was done on a Rigaku [RIG] Geigerflex diffractometer and a Rigaku 1U-200B series diffractometer. These machines have an angular resolution of $.1^o$, using Cu-K_α radiation (λ=1.541 A^o).

Fig. II-6. shows SAXD scans CuMn/Si MS for four different Mn concentrations. Usually between four and nine Bragg peaks were seen. The scans were typically made from 2^o to 8^o. Angles below 2^o are dominated by the main beam while the diffraction intensity for angles greater than 8^o are too small to interpret. It has been pointed out[45] that the registry of layers defines the coherence length of the x-rays in SADX on multilayer samples. Any deviations in the registry due to imperfect interfaces, slight variations in the layer thickness, etc., can significantly alter the intensity and width of the diffracted beam.

The bi-layer thickness, d, was determined from Bragg's equation $2dsin\theta = n\lambda$, where d is the bi-layer thickness. A program was written which compared peak angles through the equation $2d(sin\theta_{n_x} - sin\theta_{n_y}) = (n_x - n_y)\lambda$, where n_x and n_y are the orders of the Bragg peaks. This analysis has the advantage of eliminating the machine zero from the equation. This technique is only useful for determining bi-layer thicknesses $d <\approx 500A^o$, because the diffracted beam intensity drops rapidly due to the smaller number of layers (which decreases the diffracted intensity), and larger d (which decreases θ).

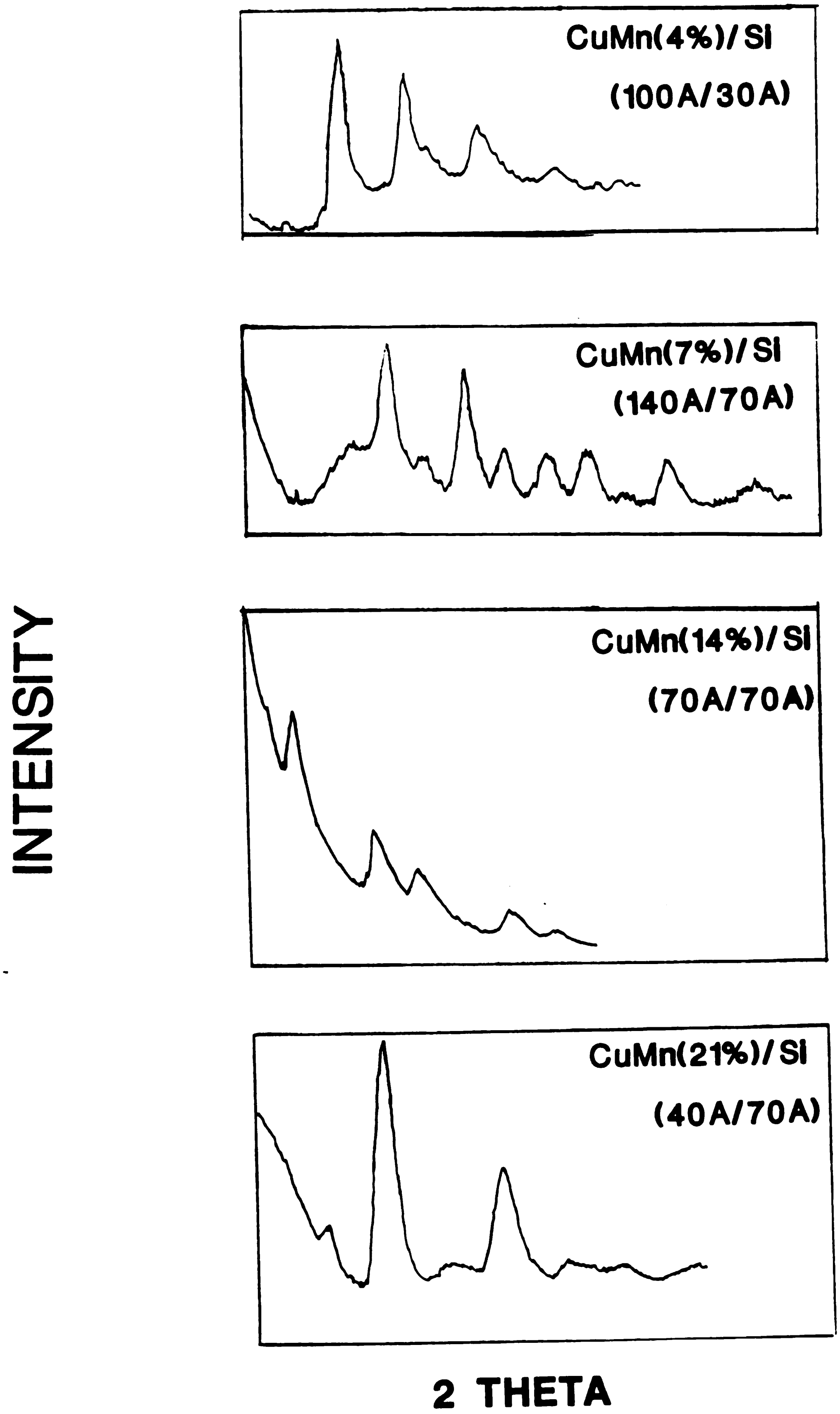

Figure II-6: SAXD scans of $Cu_{1-x}Mn_x/Si$ MS for $x = .04, .07, .14,$ *and* $.21$.

The electron densities of the CuMn/Si layers are sufficiently different for the x-ray scattering to determine a bi-layer thickness. Unfortunately this is not true for the CuMn/Cu MS; we were unable to see any SAXD even for Mn concentrations as large as 21 percent. SAXD scans on all CuMn/Si samples ($d <\approx 500\ A^o$) used in this study show good chemical layering. These range from samples with a d value as large as $570 A^o$, to a sample with Si layer thicknesses of $L_{Si} = 30\ A^o$. The absence of SAXD intensities for $L_{Si} < 30 A^o$ is interpreted as due to the lack of sufficient coherence of layers due to interfacial mixing of the constituents. Tables II-2,3,4,5 compare values of bi-layer thicknesses determined from the FTM and SAXD for the different Mn concentrations. It can be seen that these values are within a few percent of each other.

II.2.2) High Angle X-rays

High Angle x-ray analysis was done on $Cu_{.86}Mn_{.14}/Cu$ MS and $Cu_{.86}Mn_{.14}/Si$ MS of varying CuMn layer thicknesses. Several high angle peaks are observed in each scan. Most of these are due to the Si substrate. After the Si substrate peaks are subtracted from the scan we observe only the $< 111 >$ peak of Cu or CuMn, indicating stong preferential orientation of crystallites in the plane perpendicular to the layers. As the CuMn layer size is decreased in the CuMn/Si MS, the intensity of the $< 111 >$ peak decreases and the width of the peak increases. We interpret these effects as due to a reduction in the crystallite sizes. Table II-6 displays the intensity and widths of the peaks as a function of CuMn layer thickness, and estimates the crystallite sizes. The lack of superlattice lines, usually observed in MS with alternating layers of crystalline material, suggests that the Si interlayers are amorphous.

The situation in CuMn/Cu is more difficult to analyze quantitatively as there are now two peaks very close together, one from the CuMn and one from the Cu. In the samples with large L_{CuMn} ($L_{CuMn} > 300\ A^o$), and large Mn concentration (ie. 14 percent), the peaks are far enough apart to obtain a reasonably accurate de-

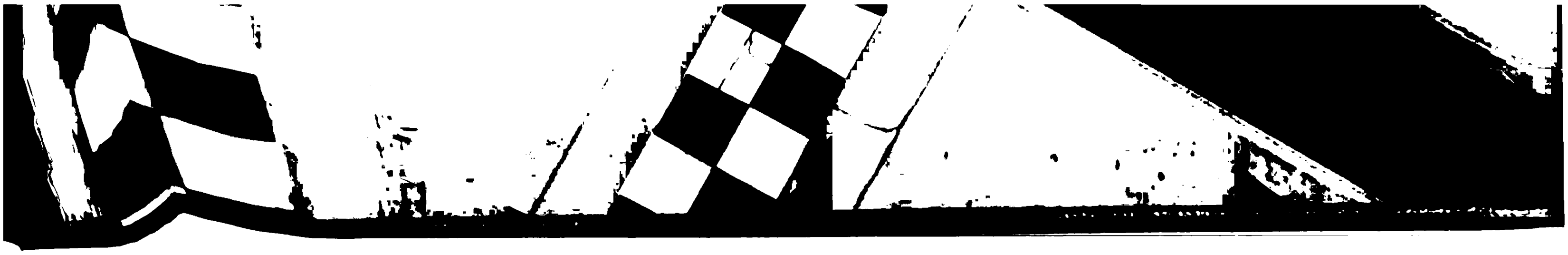

Table II-2: SAXD analysis of $Cu_{.96}Mn_{.04}/Si$ MS. Layers = total no. of bilayers in MS. Peaks = no. of observed Bragg peaks. d_{sputt} = nominal bilayer thickness. d_{x-rays} = bilayer thickness determined from x-ray analysis.

$Cu_{.96}Mn_{.04}/Si$				
SampleNo.	*Layers*	*Peaks*	d_{sputt} A^o	d_{x-rays} A^o
93-5a	100	5	120	135±7
86-6a	71	9	140	145±7
86-6b	71	7	140	138±7
86-2a	50	5	170	177±9
86-8a	33	7	220	230±12
86-4a	25	5	270	270±14
86-7a	10	5	570	614±31
96-5a	125	3	110	128±7
96-6a	50	4	130	140±7
96-7a	50	0	120	–
96-8a	50	0	110	–

Table II-3: SAXD analysis of $Cu_{.93}Mn_{.07}/Si$ MS. Layers = total no. of bilayers in MS. Peaks = no. of observed Bragg peaks. d_{sputt} = nominal bilayer thickness. d_{x-rays} = bilayer thickness determined from x-ray analysis.

$Cu_{.93}Mn_{.07}/Si$				
SampleNo.	*Layers*	*Peaks*	d_{sputt} A^o	d_{x-rays} A^o
30-b	60	6	100	101±5
32-b	84	6	120	119±6
56-b	60	4	120	122±6
28-b	67	4	130	134±7
55-b	43	6	140	139±7
33-b	44	9	210	210±11
24-b	31	5	170	169±8
23-b	25	10	270	277±14
55-b	15	3	270	256±13

Table II-4: SAXD analysis of $Cu_{.86}Mn_{.14}/Si$ MS. Layers = total no. of bilayers in MS. Peaks = no. of observed Bragg peaks. d_{sputt} = nominal bilayer thickness. d_{x-rays} = bilayer thickness determined from x-ray analysis.

$Cu_{.86}Mn_{.14}/Si$				
SampleNo.	*Layers*	*Peaks*	d_{sputt} A^o	d_{x-rays} A^o
120-1a	60	5	120	122±6
120-3b	43	5	140	152±8
120-5b	30	6	170	150±8
120-5b*	30	6	170	170±9
120-5a	30	5	170	167±8

* (rotated 90^o)

Table II-5: SAXD analysis of $Cu_{.79}Mn_{.21}/Si$ MS. Layers = total no. of bilayers in MS. Peaks = no. of observed Bragg peaks. d_{sputt} = nominal bilayer thickness. d_{x-rays} = bilayer thickness determined from x-ray analysis.

$Cu_{.79}Mn_{.21}/Si$				
SampleNo.	*Layers*	*Peaks*	d_{sputt} A^o	d_{x-rays} A^o
106-6b	75	4	110	110±5
106-2b	60	5	120	135±7
106-4b	50	3	130	136±7
101-2b	43	4	140	132±7
101-5b	30	4	170	154±8
101-7b	15	4	270	264±13

Table II-6: High Angle X-ray analysis of $Cu_{.86}Mn_{.14}/Si$ MS. Bragg peak intensity, width and calculated crystallite size are displayed.

Sample No.	L_{CuMN} A^o	*Intensity*	Width	Size A^o
120-1a	50	153	2.37	40
120-1b	50	175	2.28	42
120-3b	70	684	1.69	56
120-5a	100	937	1.48	64
120-5b	100	1280	1.45	65
120-4a	500	2034	0.81	150
120-4b	500	2213	0.78	150
120-2a	1000	1531	0.64	190
120-2b	1000	1258	0.70	170
120-6b	5000	3084	0.56	210

termination of crystallite sizes. Samples with small L_{CuMn} ($L_{CuMn} \leq 30\ A^o$) have a relatively sharp Cu peak and correspondingly large crystallite sizes ($> 300\ A^o$), suggesting that the CuMn layer is forced into large Cu crystallites with the Cu lattice parameter. In between these two extreme regions the data are more difficult to analyze but estimates of crystallite sizes have been obtained by a simple peak extrapolation method. Tables 7,8,9 display peak intensities, estimated peak widths, and estimated crystallite sizes for the CuMn/Cu MS.

II.2.3.) Cross Sections

In order to analyze the structural and chemical compositions of the MS in the FE-STEM, a technique was developed for preparing thin film cross sections. Initially we attempted to prepare the cross sections using a technique developed by Sheng and Marcus[46]. This technique was very time consuming and the samples usually broke before the sample and substrate could be thinned enough to be transparent in the electron microscope ($\leq 500\ A^o$).

A much simpler procedure using a Reichert-Jung Ultracut E microtome was developed by J. Heckman at the MSU Centre for Electron Optics Studies. The layered sample was coated with epoxy while it was still on the substrate. The epoxy and sample were then removed from the substrate and placed in an epoxy mold. The mold was allowed to harden and then shaped to fit into the microtome. The microtome sliced the sample on a diamond knife edge to thicknesses $\leq 1000\ A^o$. These slices were then floated on water and picked up on Ni microscope grids. The grids were then placed into the microscope. If the thin films were opaque to the electron beam the grid was removed from the microscope and the sample further thinned in a VCR Group Inc., Model 306, Ion Reactive Gas Milling System.

II.2.3.1.) Imaging

Selected MS cross sections were imaged with a VG HB501 (FE-STEM) and a JEOL JEM-100CX II Transmission Electron Microscope (TEM). Imaging was used both to

Table II-7: High Angle X-ray analysis of $Cu_{.96}Mn_{.04}/Cu$ MS. Bragg peak intensity, width and calculated crystallite size are displayed.

Sample No.	L_{CuMN} A^o	*Intensity*	*Width*	Size A^o
107-2b	20	194629	0.24	400
97-6b	70	14877	0.28	330
102-2b	200	13006	0.33	*
107-3b	300	6696	0.41	*
102-5b	300	7003	0.42	*
107-5b	500	4044	0.48	*
107-4a	1000	3834	0.46	*

* (Peak composed of two unseparated peaks)

Table II-8: High Angle X-ray analysis of $Cu_{.93}Mn_{.07}/Cu$ MS. Bragg peak intensity, width and calculated crystallite size are displayed.

Sample No.	L_{CuMn} A^o	*Intensity*	*Width*	*Size* A^o
121-5b	20	99619	0.21	440
121-6b	30	51696	0.22	430
121-1b	50	47498	0.27	370
121-4b	100	14121	0.37	*
121-2b	500	4156	0.54	*

* (Peak composed of two unseparated peaks)

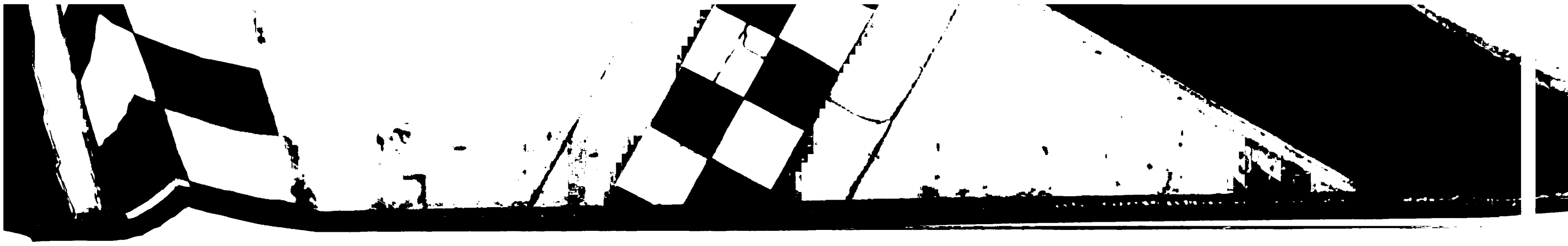

Table II-9: High Angle X-ray analysis of $Cu_{.86}Mn_{.14}/Cu$ MS. Bragg peak intensity, width and calculated crystallite size are displayed.

Sample No.	L_{CuMn} (A^o)	*Intensity*	*Width*	*Size* A^o
113-3b	30	86992	0.30	320
113-6b	50	8244	0.56	*
113-4a	70	15294	0.60*	*
113-1a	100	4260	0.61	*
113-5a (Cu)	300	2640	0.6	200
$(CuMn))$	200	1440	0.5	200
113-2b (Cu)	300	2574	0.4	200
$(CuMn)$	500	4021	0.4	200
113-8a	10000	4542	0.65	180

* (Peak composed of two unseparated peaks)

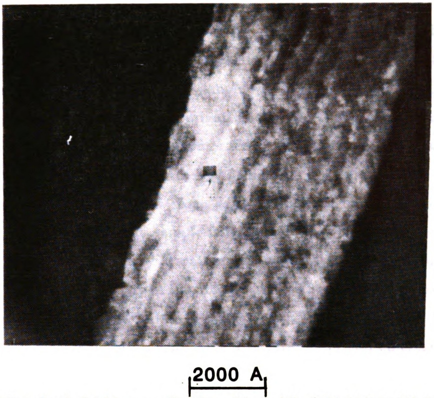

Figure II-7a: Dark field image of a $Cu_{.79}Mn_{.21}/Cu$ $(300A^o/300A^o)$ MS taken on the FE-STEM. Magnification = 100k.

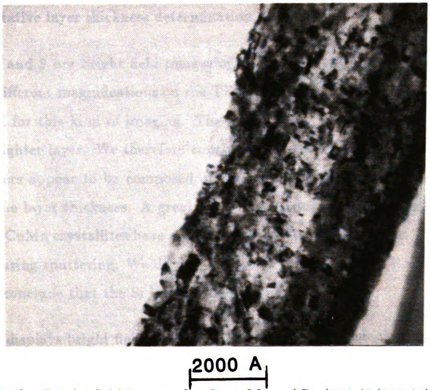

Figure II-7b: Bright field image of a $Cu_{.79}Mn_{.21}/Cu$ $(300A^o/300A^o)$ MS taken on the FE-STEM. Magnification = 100k.

view the integrity of layering and to check the individual layers. Figs. II-7 displays both the bright field and dark field images of a $Cu_{.79}Mn_{.21}/Cu$ (300 A^o/300 A^o) MS, at a magnification of 100k. This sample was microtomed thin enough so that ion milling was not necessary. The bright field image is produced by the directly transmitted electron beam. It is therefore sensitive to thickness fluctuations in the cross section. The dark spots in the bright field image are believed to be crystallites that have been preferentially cut along grain boundaries, by the microtome. We infer from this image that the sample is composed of crystallites $\leq 500A^o$. The dark field image is produced by a scattered beam. It is therefore sensitive to differences in the electron density of the cross section. The most direct observation of sample layering comes from dark field images. Fig. II-7a shows that there is layering in the electronic densities consistent with layering of two different materials. The thicknesses of the individual layers, as estimated from the magnification, are consistent with thicknesses programmed into the sputtering control system during sample preparation. Beam broadening in the sample limits the use of this technique for quantitative layer thickness determination.

Figs. II-8 and 9 are bright field images of a $Cu_{.93}Mn_{.07}/Si$ (200 A^o/70 A^o) MS, taken at different magnifications on the TEM. The TEM has better resolution then the STEM for this kind of imaging. The darker layer is electronically more dense then the lighter layer. We therefore conclude that the darker layer is CuMn. The CuMn layers appear to be composed of crystallites with diameters approximately equal to the layer thickness. A great deal of structure is observed at the interface where the CuMn crystallites have apparently grown into the Si layer. This probably occured during sputtering. We do not observe any crystallites in the Si layer, from which we conclude that the Si layer is amorphous.

Fig. II-10 displays bright field images of a $Cu_{.96}Mn_{.04}/Si$ (40 A^o/40 A^o) MS. The tranverse thickness variations of this cross section are probably due to ion milling. Both the CuMn layer (dark) and the Si layer (lighter) appear to be continous, but there is some evidence of deformation of the layers by the microtome (Fig.II-8).

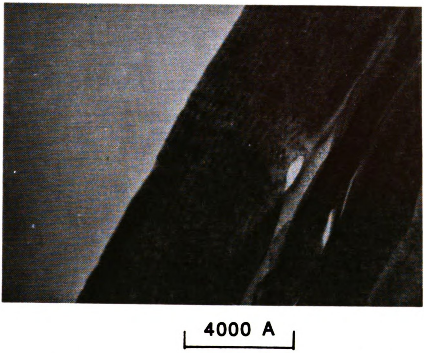

Figure II-8a: Bright field image of a $Cu_{.93}Mn_{.07}/Si$ ($200A^o/70A^o$) MS taken on the TEM. Magnification = 72k.

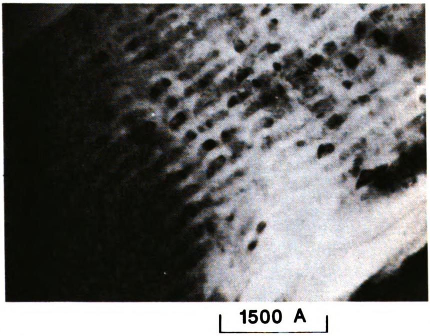

Figure II-8b: Bright field image of a $Cu_{.93}Mn_{.07}/Si$ ($200A^o/70A^o$) MS taken on the TEM. Magnification = 190k.

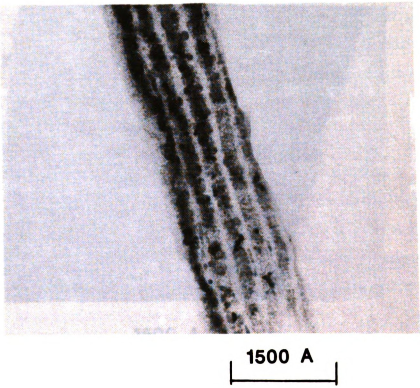

Figure II-9a: Bright field image of a $Cu_{.93}Mn_{.07}/Si$ ($200A^o/70A^o$) MS taken on the TEM. Magnification = 190k

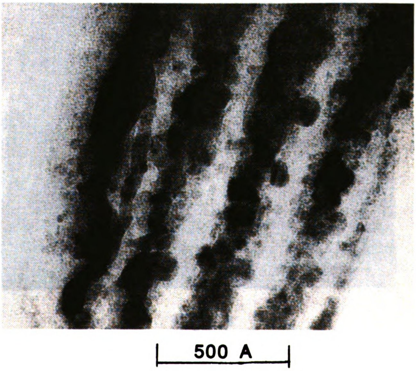

Figure II-9b: Same as above with but with magnification 700k.

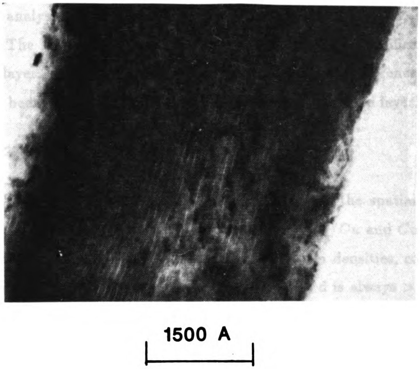

Figure II-10a: Bright field image of a $Cu_{.96}Mn_{.04}/Si$ ($40A^o/40A^o$) MS taken on the TEM. Magnification = 190k.

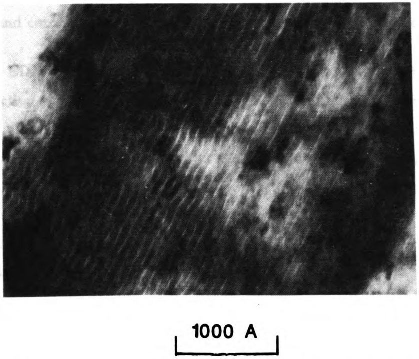

Figure II-10b: Bright field image of a $Cu_{.96}Mn_{.04}/Si$ ($40A^o/40A^o$) MS taken on the TEM. Magnification = 270k.

SAXD analysis of this sample confirms a bilayer thickness, d, of approximately 80 A^o. The TEM images suggest that the CuMn layer is significantly thicker than the Si layer. We believe, however, that this thickness difference is an artifact of greater beam broadening in the electronically denser CuMn layer.

II.2.3.2.) Energy-Dispersive X-Rays (EDX)

Energy-Dispersive X-ray analysis was used to check the spatial variation of the chemical composition of specially chosen $Cu_{.89}Mn_{.21}/Cu$ and $Cu_{.79}Mn_{.21}/Si$ layered systems, The similarity of Cu and Mn electron densities, combined with the fact that the Cu layers were 300 A^o thick (so that d is always > 300 A^o), did not allow SAXD studies of the CuMn/Cu MS.

High energy electrons (100kev) irradiating a small volume of the sample will knock core electrons out of their shells. As the atoms relax to their ground states, via the conduction electrons filling the empty core levels,they emit x-rays characteristic of the particular atom. An EDX detector (lithium-drifted Si) collects the emitted x-rays and converts them into current pulses proportional to the x-ray energy.

For our EDX analysis, the electron beam is scanned over the entire width of the cross section perpendicular to the layers. The intensities of the core energies of each element analyzed are plotted as a function of scanning distance, starting at the edge of the cross section. Sample line plots of a $Cu_{.79}Mn_{.21}/Cu$ (300A^o/300A^o) MS and a $Cu_{.79}Mn_{.21}/Si$ (70 A^o/70A^o) MS are shown in Fig. II-11 and II-12. It can be seen that the variation in the chemical composition of the elements is consistent with chemical layering. Beam spreading and poor resolution of low element concentrations (< 21 percent Mn) limited the application of EDX for microanalysis of our layered structures.

II.2.3.3.) Selected Area Diffraction (SAD)

Selected Area Diffraction (SAD) was performed on both CuMn/Si and CuMn/Cu

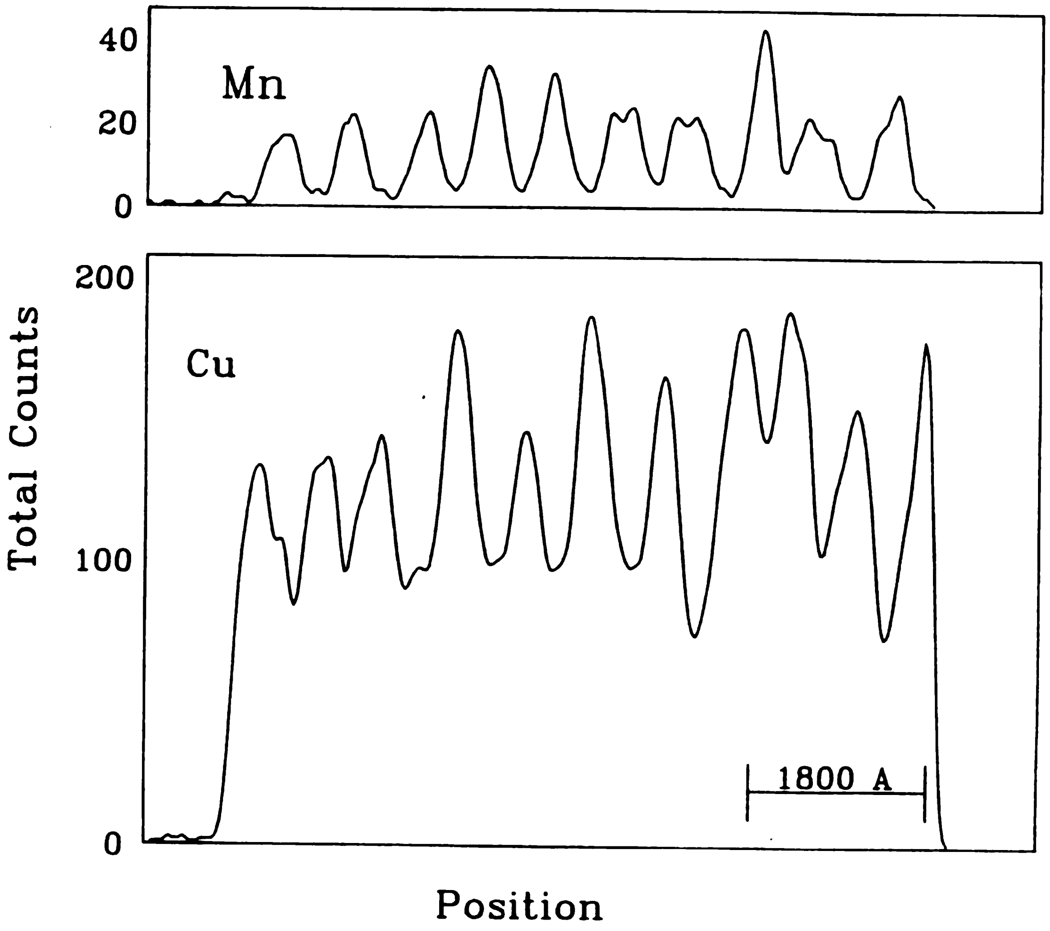

Figure II-11: EDX scan of a $Cu_{.79}Mn_{.21}/Cu$ ($300A^o/300A^o$) MS taken on the FE-STEM.

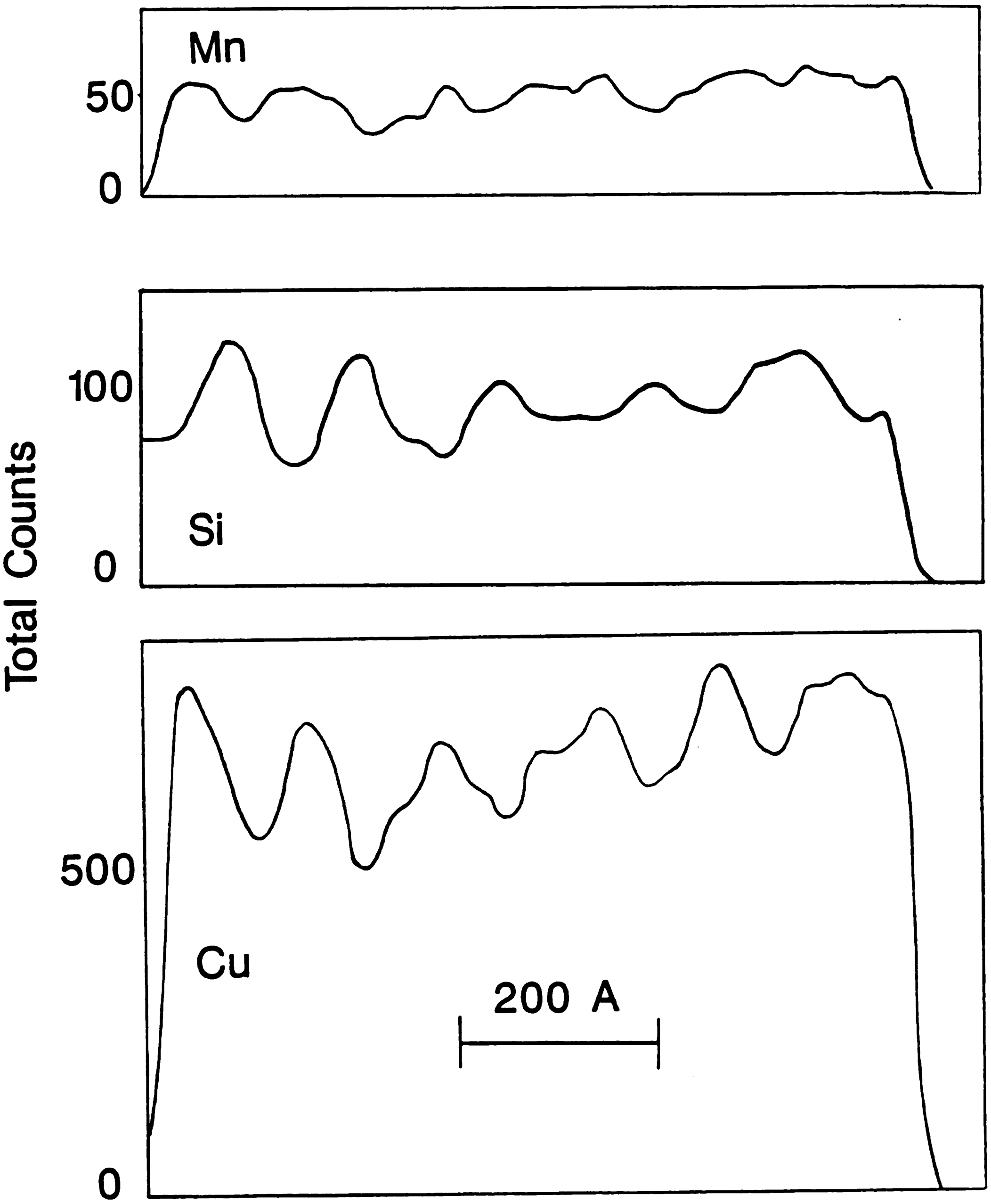

Figure II-12: EDX scan of a $Cu_{.79}Mn_{..21}/Si$ $(70A^o/70A^o)$ MS taken on the FE-STEM.

MS. This technique involves sending a parallel beam of electrons through a small area of the cross section $\approx 1\mu m^2$. The diffraction pattern which is produced allows analysis of the crystal structure orthogonal to the beam.

Fig II-13 shows the SAD pattern and corresponding line scan for a $Cu_{.86}Mn_{.14}/Cu$, 200 A^o/300 A^o MS. There is a systematic multiplicative factor between the measured diffraction ring diameter D_{obs} and the calculated diameter D_{cal} due to an incorrect setting on the camera focal length. The line scan has been analyzed in table II-10a. The observed diffraction peaks correspond to a fcc lattice with the lattice spacing of Cu, 3.61 A^o. The SAD pattern is grainy indicating that the sample is composed of crystallites. The non-uniform nature of the diffraction rings indicates that there are preferred crystallite directions in the plane of the layers.

Fig. II-14 shows the SAD pattern and a corresponding line scan of a $Cu_{.86}Mn_{.14}/Si$ (70 A^o/70 A^o) MS. The data indicates that the dominant structure is fcc with the lattice spacing of Cu. Preferred crystallite directions in the plane of the layers are also observed in these samples. The broad smoother rings observed in this pattern indicates that the crystallite sizes are significantly smaller than in the CuMn/Cu MS. No evidence of crystalline Si was found.

II.2.4.) Resistivity

The resistivities of the CuMn/Si MS were measured to determine layer continuity and to estimate the extent to which Si impurities penetrated the CuMn layers. The resistivities of the CuMn/Cu MS were measured to determine if Mn diffused into the Cu interlayer. The resistivities of our samples were measured with two techniques; standard 4-probe measurements on samples specially prepared with a 4-probe geometry, and Van de Pauw[47] measurements on sample films of arbitrary 2D geometry.

The Van de Pauw technique is a 4-probe method of measuring the resistivities of homogenous thin films of arbitrary shape. It was deduced in 1958 by L.J.Van de

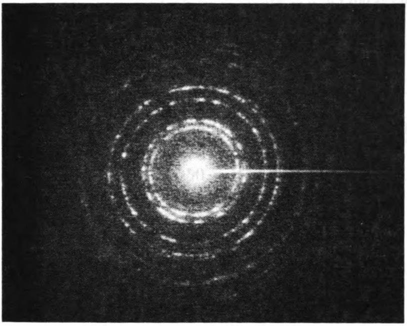

Figure II-13a: SAD pattern of a $Cu_{.86}Mn_{.14}/Si$ ($200A^o/300A^o$) MS taken on the FE-STEM.

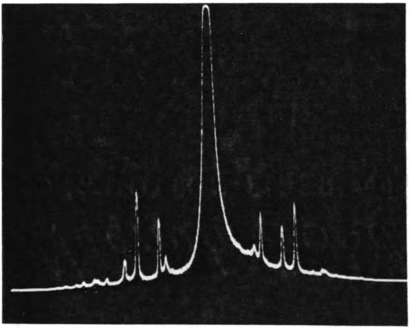

Figure II-13b: Line scan of above SAD pattern.

Table II-10a: Analysis of SAD line scan for $Cu_{.86}Mn_{.14}/Cu$ ($200A^o/300A^o$) MS.

$Cu_{.86}Mn_{.14}/Si$ 200 A^o/300 A^o				
Line ID	θ	D_{cal} (cm)	D_{obs} (cm)	*factor*
(111)	0.51°	1.775	2.35	1.324
(200)	0.59°	2.050	2.69	1.312
(220)	0.83°	2.900	3.83	1.320
(311)	0.97°	3.401	4.53	1.332
(222)	1.02°	3.552	absent	
(400)	1.17°	4.102	5.43	1.324
(331)	1.28°	4.470	6.10	1.365
(420)	1.31°	4.587	absent	
(422)	1.44°	5.026	6.65	1.323

Table II-10b: Analysis of SAD line scan for $Cu_{.96}Mn_{.04}/Si$ ($70A^o/70A^o$) MS.

$Cu_{.96}Mn_{.04}/Si$ 70 A^o/70 A^o				
Line ID	θ	D_{cal} (cm)	D_{obs} (cm)	*factor*
(111)	0.51°	1.775	2.42	1.363
(200)	0.59°	2.050	absent	
(220)	0.83°	2.900	3.92	1.352
(311)	0.97°	3.401	4.58	1.347
(222)	1.02°	3.552	absent	
(400)	1.17°	4.102	absent	
(331)	1.28°	4.470	6.07	1.358
(420)	1.31°	4.587	absent	
(422)	1.44°	5.026	6.75	1.343

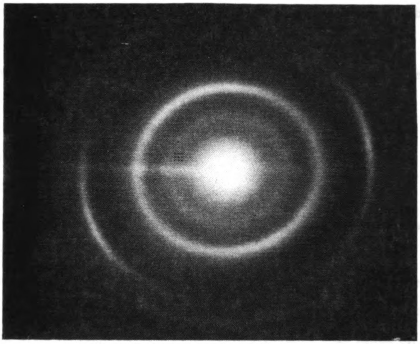

Figure II-14a: SAD pattern of a $Cu_{.96}Mn_{.04}/Si$ ($70A^o/70A^o$) MS taken on the FE-STEM.

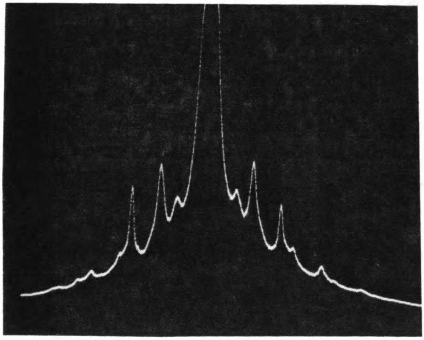

Figure II-14b: Line scan of above SAD pattern.

Pauw from conformal mapping arguments. This technique requires the following conditions:

1) The current and potential contacts are at the circumference of the sample.
2) The contacts are sufficiently small.
3) The sample is homogenous in thickness.
4) The surface is singly connected.

The sample was cut to a size and geometry that would fit onto a holder that could be inserted directly into a helium dewar. The holder is a simple rod shaped device that connects four leads from one end (the sample end) to the other end (the measuring end). The sample can then be lowered into a N_2 or He dewar and measurements made at 77 and 4.2 K, respectively. Four small scratches were made on the sample circumference with a diamond scribe. This ensured contact to all the layers. The four leads were attached at the scratch points with SC20 silver micropaint Fig. II-15a. Two resistances were obtained as follows. First current was put through leads 1 and 4 and the voltage drop was measured across leads 2 and 3, giving $R_{14,23}$. Current was then put through leads 1 and 2 and the voltage drop between 3 and 4 measured giving $R_{12,34}$. The resistivity was determined from

$$\rho = \frac{\pi d}{ln(2)} \frac{(R_{14,23} + R_{12,34})}{2} f\left(\frac{R_{12,34}}{R_{14,23}}\right)$$

where d is the total sample thickness and f is obtained from Fig. II-16. Errors are estimated as follows; geometrical error in the determination of d, 3 percent; resistance measurement error, 1 percent; and error in determining f, 3 percent.

The 4-probe technique is a standard method for measuring resistivities. We used this method on several samples to check the Van de Pauw method. Our samples were prepared by sputtering through a mask of the 4-probe geometry. This mask had the dimensions shown in Fig. 15-b. Current was passed from lead 1 to lead 4 and the voltage drop across leads 2 and 3 was measured. The resistivity was then determined from the equation $\rho = \frac{Rwd}{l}$ where $R = \frac{V}{I}$ and I is the current, V is

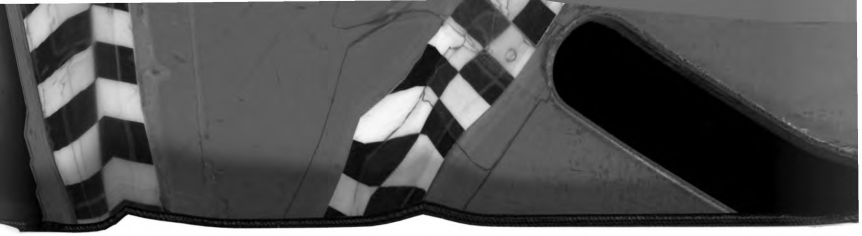

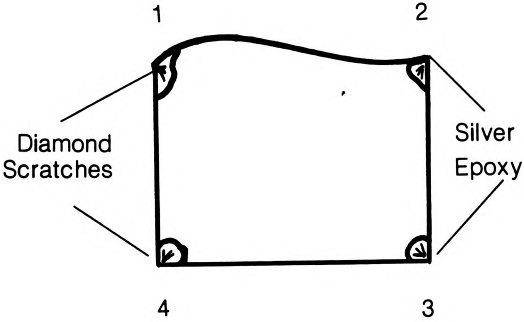

Figure II-15a: Sample geometry for Van de Pauw resistivity measurements.

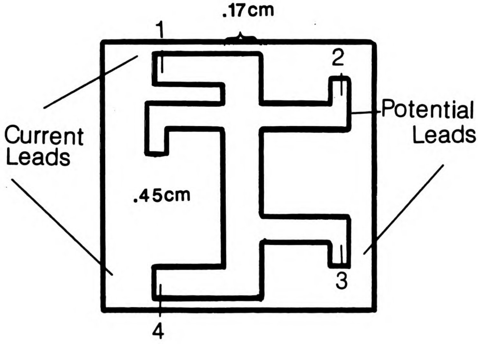

Figure II-15b: Sample geometry for 4-probe resistivity measurements.

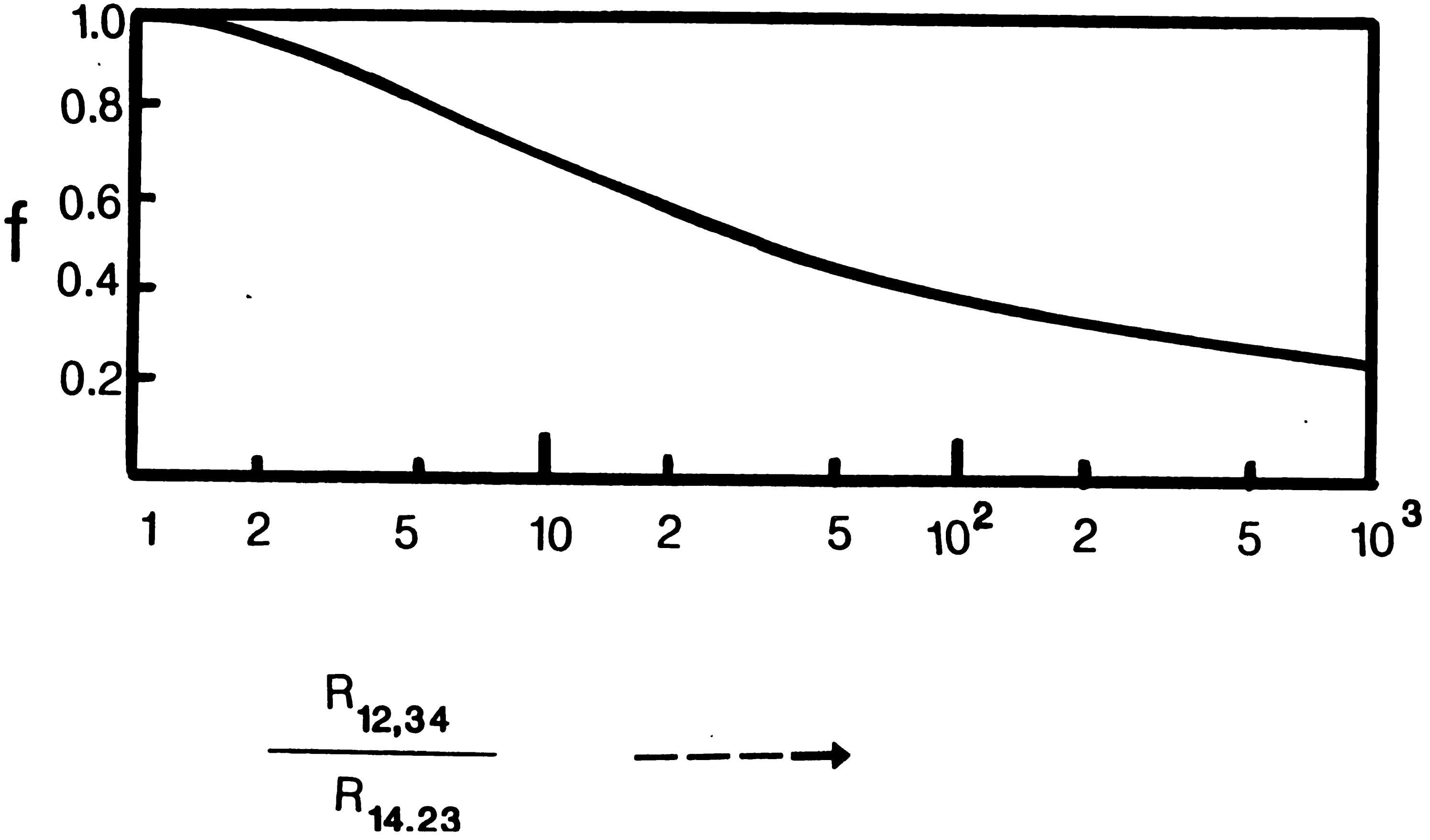

Figure II-16: Graph of f vs resistivity ratio for Van de Pauw measurements. From Van de Pauw[47].

the measured potential, d is the sample thickness, w the sample width, and l the sample length. Errors were determined as follows: error in d, 3 percent; error in w, 10 percent; error in l, 10 percent; error in V, .1 percent; error in I, .1 percent.

Resistivity measurements were made on four different types of samples: CuMn/Cu MS on Si substrates, CuMn thin films on Si and sapphire substrates, CuMn/Si MS, varying L_{CuMn}, on Si and sapphire substrates and CuMn/Si MS, varying L_{Si} on Si substrates.

Tables II-11, 12 and 13 compare the total resistivities (ρ_{Tot}) of the CuMn/Cu MS with: 1) ρ_{spec}; a model for the CuMn/Cu MS assuming only specular reflection from the interface between the CuMn and Cu layers. 2) ρ_{diff}; a model for the CuMn/Cu MS assuming only diffuse scattering at the interfaces. 3) $\rho_{uniform}$; a model for the CuMn/Cu MS, assuming that all of the Mn is distributed uniformly throughout the sample.

With only a few exceptions all of the values of ρ_{Tot} are within the limits set by ρ_{spec} and ρ_{diff}. We infer from this result that there is little diffusion of Mn out of the CuMn layer. The samples with large L_{CuMn} appear to be closer to the values of of ρ_{diff} while the smaller L_{CuMn} are nearer in value to ρ_{spec}. This shift in ρ_{Tot} coupled with the high angle x-ray data and imaging data suggest a model for the growth of the layers during sputtering.

The measured crystallite size is strongly dependent on L_{CuMn} in CuMn/Si MS. L_{CuMn} is determined by the length of time the substrate is held over the sputtering gun. Energy deposited at the surface of the MS, from the sputtered ions, causes the temperature of the layer to increase. The larger the layer the longer the layer atoms have to anneal and the larger the crystallites. The tendency towards diffuse scattering in the layer suggests that the growth of large crystallites causes a rough interface. This is confirmed by TEM images (see Fig. II-9).

Graphs of the resistivity vs. inverse layer thickness for the CuMn/Si MS are shown

Sample	L_{CuMn} A^o	ρ_{Tot}^{meas}	ρ_T^{spec}	ρ_T^{diff}	ρ_T^{un}
102-4	500	8.2±.4	4.36	6.57	9.90
102-5	300	3.6±.2	3.52	5.53	8.32
102-2	200	3.0±.1	3.06	4.91	7.06
97-7	70	3.0±.1	2.39	3.97	4.39
102-1	30	2.2±.1	2.17	3.64	3.14
102-5	20	1.6±.1	2.10	3.55	2.7

Table II-11: Table of the total resistivity ρ_{Tot} for the $Cu_{.96}Mn_{.04}/Cu$ MS, compared with a specular scattering model, a diffuse scattering model, and a uniform model for the MS. All resistivities are in $\mu\Omega - cm$

Sample	L_{CuMn} A^o	ρ_{TOt}^{meas}	ρ_T^{spec}	ρ_T^{diff}	ρ_T^{un}
121-3	5000	19.0±.8			
121-2	500	7.0±.3	4.54	7.00	15.83
121-4	100	4.3±.2	2.57	4.27	7.53
121-1	50	4.3±.2	2.29	3.84	5.16
121-6	30	3.4±.2	2.18	3.66	4.01
121-5	20	3.2±.1	2.11	3.57	3.38

Table II-12: Table of the total resistivity ρ_{Tot} for the $Cu_{.93}Mn_{.07}/Cu$ MS, compared with a specular scattering model, a diffuse scattering model, and a uniform model for the MS. All resistivities are in $\mu\Omega - cm$

$Sample$	$L_{CuMn}\ A^o$	ρ^{meas}_{T0t}	ρ^{spec}_{T}	ρ^{diff}_{T}	ρ^{un}_{T}
113-8	10000	41.±2.			
113-2	500	6.3±.3	4.93	7.96	29.65
113-4	70	3.4±.1	2.44	4.10	8.37
113-3	30	3.0±.1	2.19	3.70	6.02
113-7	20	2.1±.1	2.13	3.59	2.77

Table II-13: Table of the total resistivity ρ_{Tot} for the $Cu_{.86}Mn_{.14}/Cu$ MS, compared with a specular scattering model, a diffuse scattering model, and a uniform model for the MS. All resistivities are in $\mu\Omega - cm$

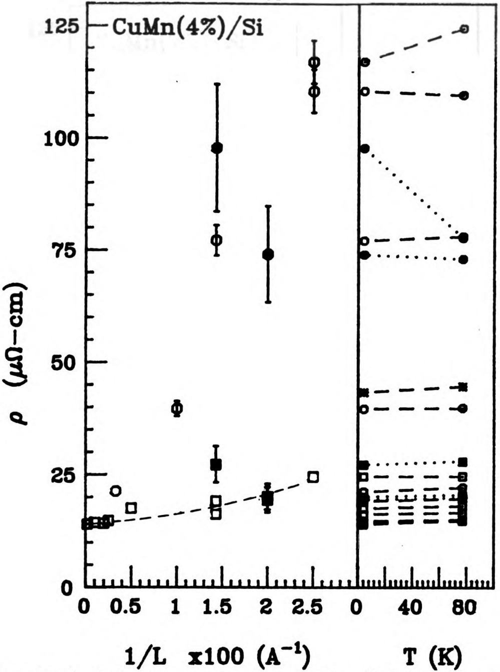

Figure II-17: Resistivity vs. $\frac{1}{L_{CuMn}}$ for $Cu_{.96}Mn_{.04}/Si$ MS. The open circles correspond to MS measured with the Van de Pauw technique. The solid circles correspond to MS measured with the 4-probe technique. The open squares correspond to thin films measured with the Van de Pauw technique. The solid squares correspond to thin films measured with the 4-probe technique. The dashed line is the fit to the Fuchs' model. Inset on the right; ρ at 4.2 K and 77 K.

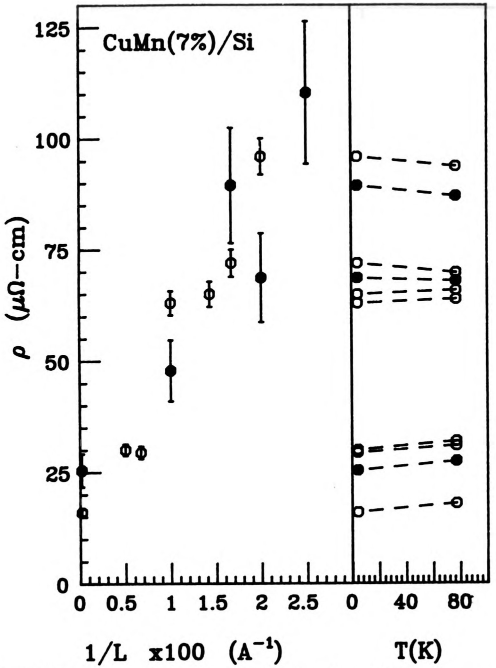

Figure II-18: Resistivity vs. $\frac{1}{L_{CuMn}}$ for $Cu_{.93}Mn_{.07}/Si$ MS. The open circles correspond to MS measured with the Van de Pauw technique. The solid circles correspond to MS measured with the 4-probe technique. Inset on the right; ρ at 4.2 K and 77 K.

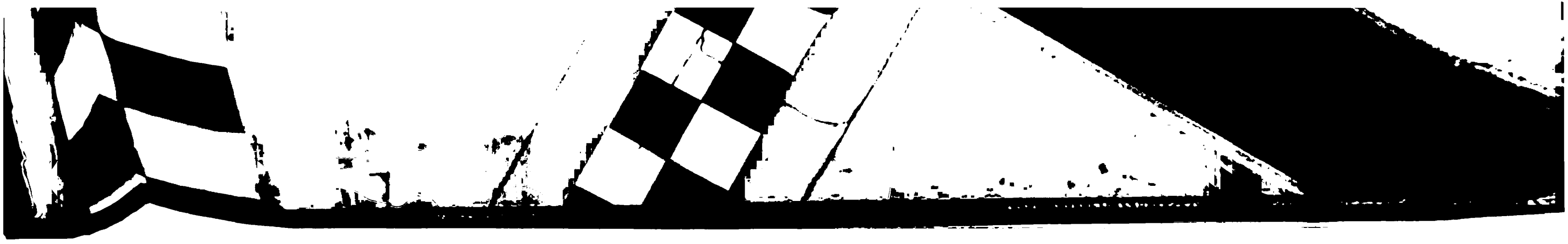

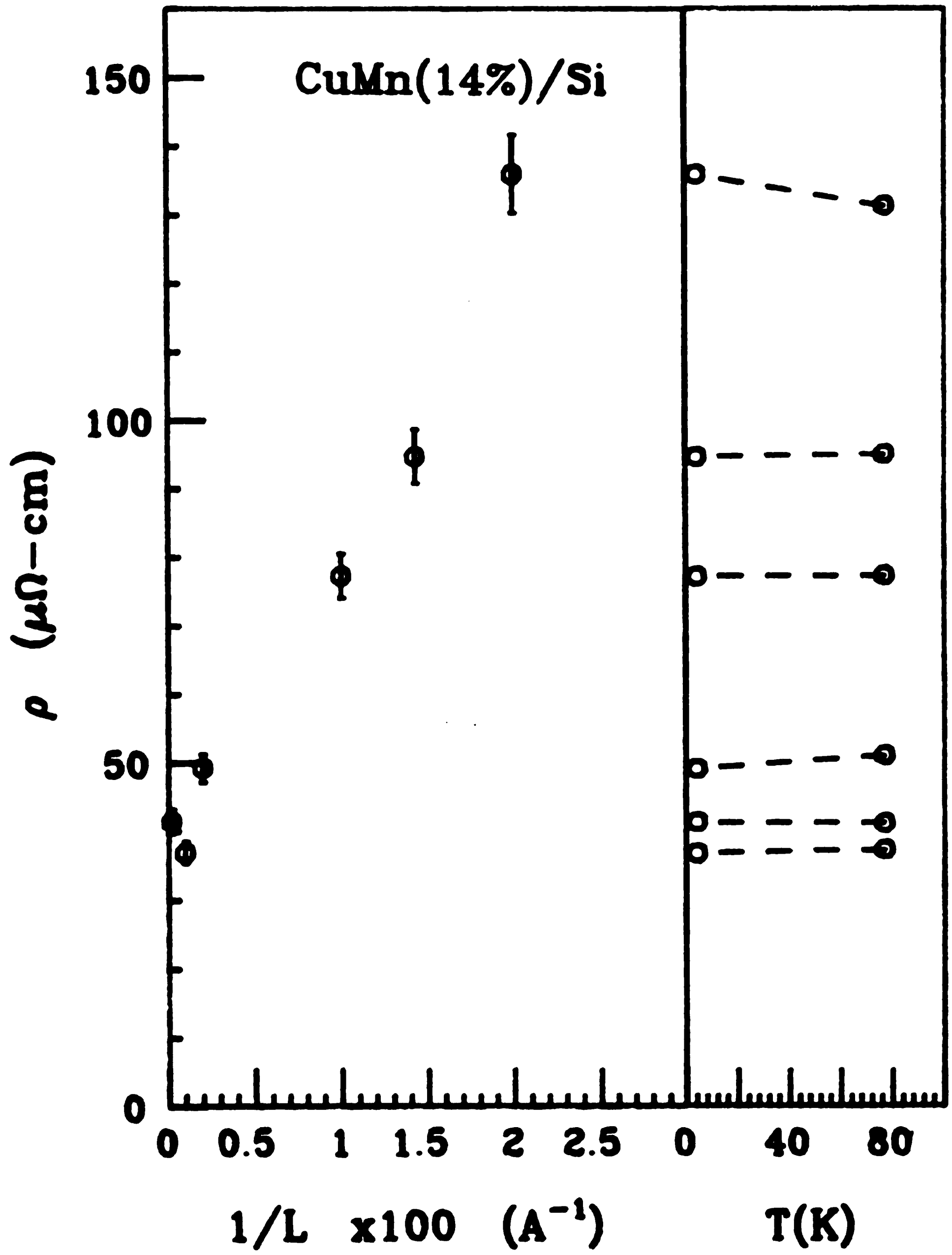

Figure II-19: Resistivity vs. $\frac{1}{L_{CuMn}}$ for $Cu_{.86}Mn_{.14}/Si$ MS. The open circles correspond to MS measured with the Van de Pauw technique. Inset on the right; ρ at 4.2 K and 77 K.

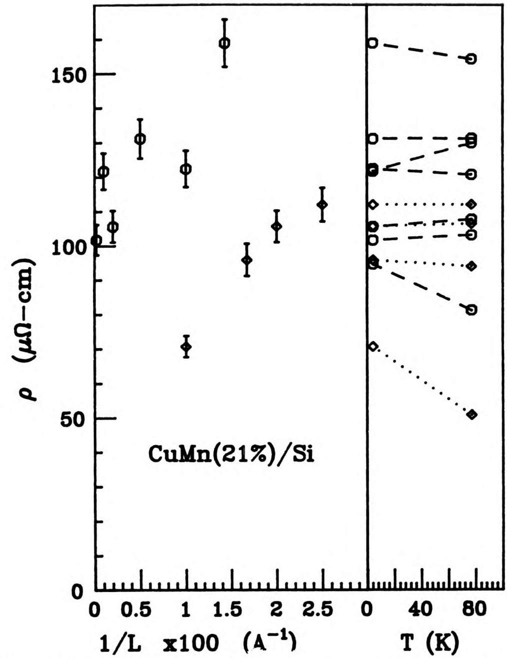

Figure II-20: Resistivity vs. $\frac{1}{L_{CuMn}}$ for $Cu_{.96}Mn_{.04}/Si$ MS. The different symbols correspond to samples made during different sputtering runs.Inset on the right; ρ at 4.2 K and 77 K.

in Figs. II- 17, 18, 19 and 20. The comparison of the resistivities of CuMn thin films with the resistivities of CuMn/Si MS in Fig II-17, show that there is definitely some penetration of Si into the CuMn layer. Using the value for ρ_{bulk} measured on samples 5000 A^o thick, the thin film data were fit to a simple Fuchs' model[48] with completely diffuse surface scattering, in the limit $L_{CuMn} >> l$ (where l is the estimated bulk conduction electron mean free path). As can be seen in Fig.II-17 the data fit the Fuch's curve fairly well. In contrast, similar thin films of CuCr and AgMn measured by Vraken et al.[49] show large increases in the resistivity as the sample size is decreased. The differences in the resistivity between our samples and their's may be alloy dependent but it is more likely that it is preparation dependent. Their films were prepared by quench-condensing small pieces of a master alloy onto a liquid nitrogen cooled glass substrate in a residual pressure of $\leq 10^{-5}$ torr. They have attributed the increase in resistivity with decreasing layer thickness to disorder inhanced electron-electron scattering. Considering the data just presented, they may be seeing the effects of island formation in their samples.

The resistivity measurements presented above have been made at 4.2 K. We have also made resistivity measurements at 77K. The resistivity of the $Cu_{.93}Mn_{.07}/Si$ MS show a systematic change in $\frac{d\rho}{dT}$ from positive (metallic) in our thicker samples to negative (nonmetallic) in the thinner samples. This result led us to investigate possible localization effects in the magneto-resistance of these dirty samples. The characteristic signature of localization[50] is a small negative magneto-resistance for magnetic fields perpendicular to the thin layers and much larger (at least an order of magnitude) magneto-resistance for a field parallel to the layer plane. No evidence of localization was observed in these experiments.

II.3) Synopsis: Structural Characteristics

II.3.1) CuMn/Cu MS

1) EDX and dark field images show chemical layering in the sample $Cu_{.79}Mn_{.21}/Cu$ $(200A^o/300A^o)$ consistent with layer thicknesses programmed during sputtering.
2) Dark field images show that interface topology is fairly rough.
3) No SAXD peaks are seen for any concentration.
4) Resistivities are consistent with CuMn/Cu layering.
5) High angle x-rays, SAD and the dark field images show evidence that the layers are polycrystalline with crystallite sizes ranging from $\approx$ 30 A^o in the 40 A^o/70 A^o MS to $\approx$ 350 A^o in 5000 A^o sample.

II.3.2 CuMn/Si MS

1) SAXD confirms compositional modulation in samples $(d \leq 500A^o)$ to within a few percent of the thicknesses selected during the sputtering process.
2) Dark field images and EDX on samples with thick layers show compositional modulation of layers with layer thicknesses consistent with SAXD.
3) Dark field images show that the topology of the interfaces is not planar.
4) High angle x-rays and line scans of SAD show fcc Cu lines with preferential directions in the layer, from which we infer that the layers are polycrystalline with crystallite sizes ranging from $\approx$ 40 A^o in the 50 A^o/70 A^o MS to $\approx$ 200 A^o in 5000 A^o sample.
5) Lack of observed crystallites in the TEM images indicate that the Si is amorphous.
6) Resistivities are finite down to at least $L_{CuMn} = 40A^o$ implying that the layers are continous.
7) Comparison of CuMn/Si and thin film CuMn resistivities imply diffusion of Si into the CuMn layers.

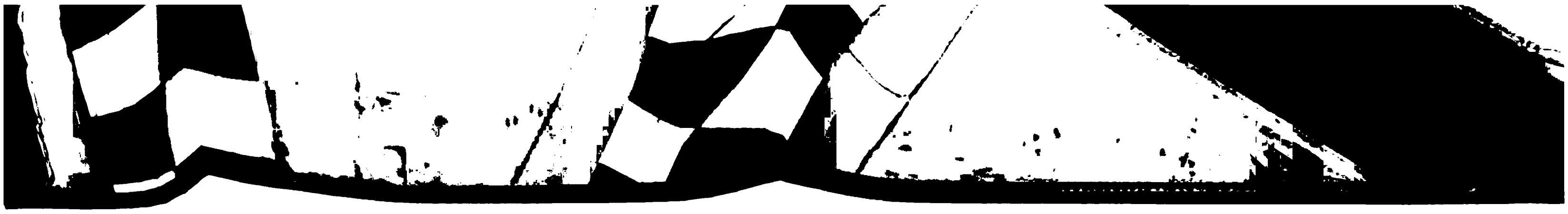

CHAPTER III

THEORY

The experimental motivation to study the three to two dimensional crossover in spin glasses was provided by theoretical studies of three and two dimensional spin glasses within SG mean field theories. SG mean field theories fall into two major catagories: 1) Bond disorder models such as the Edwards Anderson[51] (EA) model and Sherrington Kirkpatrick[52] (SK) models incorporate magnetic disorder by randomizing the bonds between magnetic ions on a fully occupied lattice. These models and their implications on dimensional crossover are discussed in the first section of this chapter. 2) Site disorder models incoroporate magnetic disorder by randomizing the location of magnetic ions on a lattice. These models have been used to analyze Heisenberg spin models with RKKY interactions in three dimensions. We have used a static site disorder model –the uniform quenched model– to help understand the effects on T_g of the diffusion of Si impurities into the CuMn layers in the CuMn/Si MS. Site disorder models including the uniform quenched model are discussed in the second section of this chapter. For a more complete discussion of spin glass mean field theories, see ref. 5.

The third section of this chapter starts with an introduction to phase transition scaling, and is based on lectures by M. Fisher[53], presented at the Advanced Course

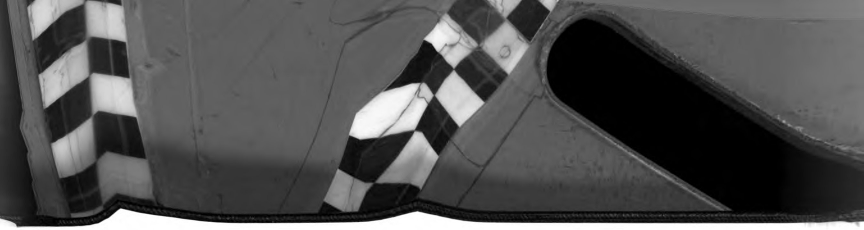

on Critical Phenomena. Through a modification of the early work of Landau, some of the present day scaling relationships are derived. There is then a discussion of finite size scaling and its relationships, derived from a scaling ansatz. The final part of this section is a fairly detailed discussion of the application of scaling in the droplet excitation model (Fisher and Huse[54]) as applied to the three to two dimensional cross-over behaviour of spin glasses.

III.1) Disorder Theories

In general, a mean field theory in a statistical mechanical treatment of many body problems attempts to average over all possible statistical probabilities. The major question as this applies to spin glasses is; how does one average over all possible states of a disordered system? The first problem is the technical difficulty of carrying out the proper type of disorder average and the second difficulty is that many equivalent 'ordered' (frozen) states exist. The details of these states depend on the exact nature of the physical interactions in the sample and are therefore sample dependent. The free energy equivalence of these states is an accidental consequence of the system randomness. Binder and Young[5] argue that all macroscopic properties are the same for these degenerate states.

In general the free energy of a statistical mechcanical system is calculated by averaging over all possible states in phase space.

$$F = -k_B T ln[Z]_{av}$$

This averaging can be done only when the fluctuation time scales of the system are very small compared to experimental time scales, $\tau_{fluc} << \tau_{exp}$. Under these circumstances all possible states in phase space have an equal probability of being sampled and the average is an equilibrium thermal average. This is called an annealed average.

In the case where $\tau_{exp} << \tau_{fluc}$ the experiment cannot average all possible states so averaging over the partition function does not make sense. Instead the averaging is done over an extensive variable such as the free energy. This type of averaging will encompass all possible random configurations with the same free energy. This is called a quenched average, $F = -k_B T [ln\ Z]_{av}$.

One possible solution employed by EA, to calculate the average over lnZ, comes in the form of a mathematical identity known as the n=0 replica trick.

$$[ln\ Z]_{av} = \lim_{n=0} \frac{[[Z^n] - 1]}{n}$$

If x is some random variable (ie concentration) describing the system then we can write

$$Z^n(x) = \prod_{\alpha=1}^{n} Z_\alpha(x) = exp[- \sum_{\alpha=1}^{n} [H(x, S_i^\alpha)/k_B T]$$

where the Hamiltonian is of the Heisenberg form;

$$H = \frac{-1}{2} \sum_{ij} J_{ij} \mathbf{S_i} \cdot \mathbf{S_j} - \mathbf{h} \sum_{\mathbf{i}} \mathbf{S_i^z} \qquad \textbf{III–1}$$

In a variation of Marshall's[55] mean field distribution EA proposed a model consisting of random magnetic bonds interacting between the nearest neighbors of a fully occupied lattice. The exchange interaction J_{ij} between nearest neighbor spins i and j is chosen according to a fixed gaussian distribution.

$$P(J_{ij}) = [2\pi(\Delta J_{ij})^2]^{-\frac{1}{2}} exp[(-J_{ij} - \bar{J}_{ij})/2\Delta J_{ij}^2]$$

Sherrington and Kirkpatrick (SK)[52] proposed extending the sum in the Hamiltonian, over all sites i and j.

In addition EA[51] (1976) suggested that while there does not appear to be any spatial correlations, between the moments, in a spin glass, there may be correlations in time. They proposed an autocorrelation function in time to describe the ordering of the spin glass state

$$q = \lim_{t \to \infty} \langle \langle S_i(0) S_i(t) \rangle \rangle$$

where the inner bracket denotes a thermal average and the outer bracket a spin average. This 'order parameter' measures the correlation of spin i at time $t = 0$

with the same spin at time t. As $t \rightarrow \infty$ all possible time scales of the system are averaged and q converges to a constant value. If q is non-zero below a certain T_g then correlations exist and a phase transition has occured.

Both of these models (EA and SK) have been studied extensively in Ising like systems. These models predict a second order phase transition and show a cusp in the zero field susceptibility and also in the specific heat. The EA correlation parameter q is found to decay to zero for $T > T_g$ (indicating paramagnetism) and decays to a finite value for $T < T_g$ (indicating temporal correlations). While these models are clearly different from real spin glass materials they may be seen as a reasonable starting point in a proper treatment of the inherent disorder. Ogielski and Morgenstern[56] (1986) did Monte Carlo simulations of a three dimensional short range Ising model with lattice sizes 16^3, 32^3, and 64^3. They have found the existence of a spin glass state at a finite temperature, through the convergence of the EA order parameter. Fitting the average correlation function

$$G(r) = V^{-1} \sum_{x} < S_x S_{x+r} >^2$$

to a standard three parameter form

$$G(r) = \frac{C[exp(\frac{-r}{\xi})]}{r^x},$$

they find the growth of the correlation function ξ described by the algebraic form

$$\xi \sim C|T - T_g|^{\nu},$$

with $\nu = 1.2 \pm .1$. Other groups have found using different methods, and smaller lattices, values for the Ising model of $\nu = 1.8 \pm .5$[57], $\nu = 3.3 \pm .6$[58], $\nu = 1.3 \pm .3$[59]. For a more complete discussion of short range Ising spin glass models in 2, 3, ... dimensions, see ref 5. The lower critical dimension of the short range Ising spin glass model is not yet known but it has been suggested that it lies in the range $d_c = 2 \rightarrow 4$[60,61,62].

Recently Reger and Young[7] extended the EA model to three dimensions with RKKY interactions by making the exchange interaction in Eq. III-1 spatially dependent, (ie. $J_{ij} \sim \frac{cos(2k_F R_{ij})}{R_{ij}^3}$). Using lattice sizes of $L^3 = 4^3$, 6^3, 8^3, 11^3, 16^3, they found that they could not rule out a non zero transition temperature and suggest that the LCD of a long range Heisenberg spin glass is ≈ 3. They also infer from their results that this RKKY Heisenberg model is in a different universality class then the short range model discussed by Ogielski and Morgenstern. Finite size scaling analysis[7] of these small systems gives a lower bound of $\nu > 2.3$.

III.2) Site Disorder Models

Chakrabarti and Dasgupta[63] applied the Hamiltonian

$$H(R_{ij}) = J_o \sum_{j<i} \left[\frac{cos(2k_F R_{ij})}{R_{ij}^3} \right] \mathbf{S_i} \cdot \mathbf{S_j}$$

to an LxLxL fcc lattice, where the Heisenberg spins ($\mathbf{S_i}$) are at randomly chosen sites on the lattice. Using a Monte Carlo technique, on lattice sizes with 20, 44, 81, 161, and 312 spins, they conclude that the RKKY model has a critical point at $T_g = 0$, and that the correlation length exponent is $\nu = .87 \pm .08$. Monte Carlo simulations of RKKY CuMn spin glasses in three dimensions show no spin glass ordering, at finite temperatures, if only pure isotropic exchange is employed. Walstead and Walker[31] have found a non-zero EA order parameter using a dipolar anisotropy. They find, fitting to experimental transition temperatures, that the strength of this anisotropy is much greater than experimental values.

Bray, Moore and Young[64] studied vector spin glasses with RKKY and anisotropic interactions, within a site disorder framework. They have concluded that the 'isotropic vector spin glass in three dimensions is at its lower critical dimension and lies in a different universality class from the case of short range interactions.'

Larsen[65] has developed several site disorder models of varying complexity including the uniform quenched model. Although this is a static model, it should give

reasonable estimates to the spin energetics and hence the transition temperature. This model relies on an RKKY interaction between lattice sites.

III.2.2) RKKY Interaction

Magnetic atoms in a dilute metallic alloy couple through the RKKY interaction. This interaction was first used by Ruderman and Kittel[10] to explain the coupling between nuclear moments through the hyperfine interaction. Kasuya[66] later explained how localized d electrons in transition metals scattered conduction electrons. Yosida[67] combined these to derive the Ruderman Kittel Kasuya Yosida (RKKY) interaction. The RKKY interaction couples separated magnetic atoms together through the conduction band electrons.

$$J(R_{ij}) = \frac{\mathbf{I_i} \cdot \mathbf{I_j} |\Delta_{k_F k_F}|^2 m}{4 \cdot (2\pi)^3 R_{ij}^4 \cdot h^2} [2k_F R_{ij} cos(2k_F R_{ij}) - sin(2k_F R_{ij})] \qquad \textbf{III-2}$$

It has an oscillatory nature, and decays as $\frac{1}{R^3}$ away from the impurity atom. For a complete derivation of the RKKY interaction in three and two dimensions see Appendix 1. Recently Levy and Zhang[68] went beyond the free electron RKKY derivation by incorporating the d state resonance of Mn in Cu, in a Friedel Anderson model. They found that the interaction is oscillatory and decays as $\frac{1}{R^3}$ in the asymptotic region but only decays as $\frac{1}{R^2}$ in the preasymptotic region, $R < 20 A^o$.

The effects of non-magnetic impurities on the strength of the RKKY interaction is now a matter of some discussion. DeGennes[69] incorporated mean free path (MFP) effects into the RKKY interaction by giving the free electrons, in the second order perturbation expansion, a finite lifetime. This has the effect of exponentially damping the RKKY interaction.

$$J_{RKKY}^{damped} = J_{RKKY} e^{-\frac{R}{l}} \qquad \textbf{III-3}$$

where l is the mean free path of the conduction electrons.

Larsen[65] has used this damped RKKY interaction to explain the effects of added non-magnetic impurities studied experimentally by Vier and Schultz[70]. Recently

Jagannathan, Abrahams and Stephen[71] have claimed that the DeGennes method is an incoherent phase average and therefore smears out any phase information. They claim that if the phase information is averaged 'properly' (i.e. by averaging the square of the oscillating potential) the disorder has little effect on the strength of the interaction. This suggests that the DeGennes model sets an upper bound on impurity effects.

III.2.3) Quenched-Uniform Model

Larsen[65] has developed several models to obtain the local energy scale of individual spins in the spin glass. This local energy scale is of the form of a root mean squared sum over the RKKY interaction between spin sites.

$$\Delta_i = \left[\sum_{j \neq i} [J(R_{ij})]^2 \right]^{\frac{1}{2}}$$

This can be modified to approximate a uniform environment by replacing the sum with an integral. Including the RKKY interaction Δ_i has the form:

$$\Delta_i = \left[\frac{3J_0^2 c}{a^3} \int_{r_o}^{\infty} R^2 \left(\frac{a}{R}\right)^6 dR \right]^{\frac{1}{2}} \qquad \text{III-4}$$

where c is the concentration and a is the lattice parameter.

Larsen points out that 'the essence of quenching is that a given spin never experiences a closer encounter then a definite nearest neighbor.' Quenching can therefore be incorporated into the model by letting the lower limit of integration r_o be concentration dependent and equal to nearest neighbor impurity distance.

Applying the quenched-uniform model to a layered geometry requires some modification to Eq. III-4. The layered geometry has cylindrical symmetry which can be used to simplify the derivation. This geometry can be employed with several small approximations. The volume that a single magnetic impurity occupies, defined by r_o in spherical symmetry, must remain the same as in the spherical system. It would be a difficult task to construct a sphere in the cylindrical geometry, so an approximation is made to a cylinder of the same volume. The best approximation can be made by realizing that a sphere minimizes the surface of a given volume. A minimum area cylinder is therefore employed in the calculation. It is easily shown that the radius $r_0^{cy}(c)$ = height $h_0^{cy}(c) = \frac{a}{(8\pi c)^{\frac{1}{3}}}$ where a is the lattice constant of Cu (3.61 A^o) and c is the impurity concentration.

The second problem that arises is that unlike the infinite spherical model all impurity sites in the layer are not equivalent. The atoms near the edge of the layer do not have the same number of near neighbor impurity atoms as those near the ceBntre of the layer. An average must therefore be taken over all possible lattice sites. Equation III-4 therefore becomes:

$$\Delta_i = \Bigg[\frac{c\rho}{N}\sum_{i=0}^{N}\Bigg[\Big[\int_{r_0(c)}^{\infty}\int_{a_i-h_o}^{a_i+h_o} J^2(r,z)drdz \qquad \textbf{III-5}$$

$$+ \quad \int_0^{\infty}\Big[\int_{a_i+h_0}^{\frac{L}{2}} J^2(r,z)dz + \int_{a_i-h_0}^{\frac{-L}{2}} J^2(r,z)dz\Big]dr\Big]_{\substack{first\\layer}}$$

$$+ \quad \Bigg[\sum_{j=-\infty}^{\infty}\int_{\frac{L}{2}+jT-a_i}^{\frac{3L}{2}+jT-a_i}\int_0^{\infty} J^2(r,z)drdz\Bigg]_{\substack{all\ other\\layers}}\Bigg]\Bigg]$$

where ρ is the density of lattice sites, L the layer thickness of the alloy, T the interlayer thickness, a_i the distance fron the center of the layer to the middle of the cylinder and $J(r,z)$ is the RKKY interaction given by Eq. III-2 or with exponential damping Eq. III-3.

Above T_0, the temperature that corresponds to the energy Δ_i, thermal fluctuations dominate and the spin looks paramagnetic. Below T_0 the RKKY interaction dominates and the spin is 'frozen'. The transition temperature is therefore defined $T_g = T_0 = A_0\Delta_i$ where A_0 is a proportionality constant found by equating Δ to a bulk experimental value of T_g.

It must be pointed out that this model assumes perfect boundaries and does not account for distortions of the Fermi energy due to the finite film size.

III.3) Scaling Theory

III.3.1) Introduction

Scaling theory is a phenomenological theory which mathematically models divergences in real systems. Scaling theory was first applied by Landau[72] to describe discontinuities near the critical temperature in systems undergoing phase transitions. The essence of a thermodynamic phase transition is nonanalytic behaviour in the free energy F. This nonanalytic behaviour manifests itself in physical quantities such as the specific heat and magnetic susceptibility. The divergences have been found, theoretically and experimentally, to be symetric about the critical point and completely reversible in the absence of a symmetry breaking field. The leading order of this nonanalytic behaviour manifests itself in the algebraic form $(T - T_c)^m$ where m is called a universal critical exponent. It was found experimentally that many different systems have the same critical exponents and are said to belong to the same universality class. An example of universality is the solubility phase transition of binary liquid mixtures. These systems are characterized at low temperatures by insoluble phases and at temperatures higher then the consolute point (ie. transition temperature) by a homogeneous liquid. The molar fractional difference between the two phases is found to scale as $(x^\alpha - x^\gamma) \sim |T - T_c|^\beta$. The same exponent $\beta = .33$ has been experimentally determined for the coexistence of CCl_4 and C_7F_{14}, Na, Li, Ca dissolved in NH_3 [73], and many liquid vapor coexistence systems. The similar form of the divergence suggests that the underlying physics for all of these different transitions is similar and therefore they all belong to the same universality class.

The Landau theory[53] assumes that near the critical point the system orders and that there is an identifiable order parameter which describes the growth in order near the critical point. The order parameter in ferromagnets is the magnetization. The ferromagnetic system will be used to elucidate the scaling concepts. Landau's prescription is as follows: 1) Expand the free energy in powers of the order parameter.

$$F(T,M) = F_0(T) + F_2(T)M^2 + F_4M^4 + \ldots$$

From thermodynamic arguments we know that $\frac{\partial F}{\partial M} = H$ the magnetic field. Therefore $\chi^{-1} = 2F_2(T) + O(M^2)$ 2) Assume $F_2(T)$ can be expanded in powers of $t = (T - T_c)$ where T_c is the critical temperature. Therefore one obtains

$$\chi^{-1} = 2F_{2,0} + 2F_{2,1}t + O(t^2)$$

or the magnetic susceptibility scales as $\chi \sim (T - T_c)^{\beta} = (T - T_c)^{-1}$ The equation of state can also be found from $(\frac{\partial F}{\partial M})$ which gives $H = M(cT + uM^2)$ where $c = 2F_{2,1}$ and $u = 4F_{4,0}$. At the critical temperature $H = uM^{\delta} = uM^3$ or $\delta = 3$.

The critical exponents obtained by Landau's theory are wrong when compared to real or simulated systems. The reasoning is that the expansions made by Landau assume that F is analytic, which is clearly not the case at the transition temperature. Widom[74] proposed that nonanalytic behaviour could be accounted for in the phenomenological approach by simply grafting in new critical exponents. For example the new equation of state would be $H = M(ct + uM^{\frac{1}{\beta}})$ where β is found from experiment or simulation. The scaling postulate states that the order parameter scaled by some appropriate temperature is a function of a scaled field.

$$ie. \quad \frac{M}{|t|^{\beta}} = BW\left(\frac{DH}{|t|^{\Delta}}\right) \qquad \text{III-6}$$

where W is a universal function.

Starting from Eq. III-6 we obtain

$$\chi = \left.\frac{\partial M}{\partial H}\right|_{H=0} = |t|^{\beta-\Delta}BDW'(0)$$

The susceptibility scales as

$$\chi \sim t^{\gamma}$$

therefore

$$\gamma = \Delta - \beta$$

This is the first of the so-called scaling relationships. A list of critical exponents and their relationships to physical quantities is given in Table III-1.

III.3.2) Finite Size Scaling

In thermodynamics, phase transitions and their associated singularities occur only in the limit that both the volume V and the number of particles N approach infinity while the density $\rho = \frac{N}{V}$ remains constant. In real experimental systems this thermodynamic limit is never reached. Quantities like the specific heat or magnetic susceptibility may appear to be divergent, but they are not. If one could follow the curves with perfect resolution it would be found that the the 'divergence' only grows to a finite height. One therefore asks 'What determines the height of the curve?'

Phase transition are characterized by an ordering in the system. The system orders by growth in correlations among the constituents. As the critical temperature is approached the spatial extent (correlation length) of these correlations approaches infinity. In real samples the growth in the correlations is limited by the finite size of the sample, limiting the divergent behaviour of the phase transition.

Finite size scaling is the theory that addresses the concepts of phase transitions and their singularities in thermodynamic systems of finite size. The development of Renormalization Group Theory (RGT) has lead to a very physical way of looking at this 'phenomenological' theory. From RGT the concept of universality follows naturally from intrinsic spatial symmetries and the form of the Hamiltonian. For a more complete discussion of RGT see ref. 53.

The discussion that follows is based on the phenomenological approach starting from the scaling *ansatz*[75]. This *ansatz* states that 'In the vicinity of the bulk critical temperature the behaviour of a system with at least one large but finite dimension is determined by the scaled variable $y = \frac{L}{\xi(t)}$ where $\xi(t)$ is the correlation length and L is the characteristic length scale of the system'. For our samples L is

Table III-1 Critical exponents and their relationships.

Name	Exponent	Relationship
Correlation Exponent	ν	$\xi \sim (T - T_c)^{-\nu}$
Magnetization Exponent	δ	$M \sim H^{\delta}$
Magnetic Susceptibility Exponent	γ	$\chi \sim (T - T_c)^{-\gamma}$
Specific Heat Exponent	α	$C \sim (T - T_c)^{-\alpha}$
Shift Exponent	λ	$(\frac{T_c - T_c^L}{T_c})^{-\lambda}$
Rounding Exponent	θ	$(\frac{T^*(L) - T_c}{T_c})^{-\theta}$

T_c is the bulk critical temperature.

M is the magnetization.

H is the magnetic field.

C is the specific heat.

$T^*(L)$ is the rounding temperature.

the thickness of the individual layers of spin glass. In general the argument to be presented is based on the review article by Barber.[75]

Let $P_L(T)$ be some thermodynamic function that diverges at the critical point (ie magnetization in ferromagnets, non-linear susceptibility in spin glasses). In the thermodynamic limit this function scales as

$$P_\infty(T) \sim C_\infty t^{-\rho}$$

where $t = \left[\frac{T-T_c^b}{T_c^b}\right]$, and ρ is an appropriate critical exponent. In the layered geometry a phase transition occurs but at shifted temperature T_c^L. Therefore

$$P_L(T) \sim C_L \dot{t}^{-\dot{\rho}}$$

where $\dot{t} \sim [T - T_c^L]$ and $\dot{\rho}$ is an appropriate two dimensional exponent. In general $\rho \neq \dot{\rho}$ and one should expect to see crossover behaviour at some finite L. The finite size scaling *ansatz* asserts that the behaviour of P is determined by y.

$$P_L(T) = L^\omega Q(y)$$

where Q is a universal function and the L out front scales the magnitude of the physical property with the system size. A more general way to write this is $P_L(T) \sim L^\omega Q_p(L^\theta \dot{t})$. By requiring that

$$Q(x) \sim C_\infty x^{-\rho} \qquad\qquad L \to \infty$$

it is easily determined that

$$\omega = \rho\theta = \frac{\rho}{\nu}, \quad or \quad \theta = \frac{1}{\nu}.$$

The correlation length ξ is postulated to grow as

$$\xi \sim (T - T_c)^{-\nu}.$$

Fisher and Ferdinand[76] have asserted that the criteria for determining finite size effects in the critical region is found by matching the correlation length to the thickness. Therefore the critical exponent λ which determines the shift in the critical temperature away from the bulk critical temperature T_c^b as a function of layer thickness should be equal to the inverse of the correlation exponent (ie.$\lambda = \frac{1}{\nu}$).

In the layered geometry we have been working with the quantity $\dot{t}$. We can redefine the universal function Q($\dot{\mathrm{t}}$) to be a function of t such that

$$P_L(T) = L^{\frac{\rho}{\nu}} \bar{Q}_P(L^\theta t)$$

by defining $\bar{Q}_P(x) = Q(x - \dot{x}_c)$ where $\dot{x}_c = L^\theta \frac{[T_c^L - T_c^b]}{T_c^b}$ or

$$\frac{[T_c^L - T_c^b]}{T_c^b} \sim \frac{\dot{x}_c}{L^\theta} = \dot{x}_c L^{-\lambda} \qquad \text{III-7}$$

This is the scaling relationship which we have used to determine the critical exponent λ from the shift in the transition temperature.

III.3.3) Droplet Excitation Model

Recently Fisher and Huse[54] used their droplet excitation model to understand our layered spin glass systems. In this model one looks at an infinite lattice (in a spin glass ground state at T=0) with spins placed randomly on the lattice. If one takes a volume in this system defined by the length scale L and flips all of the spins in that volume then that 'droplet' aquires a free energy which according to their fundamental ansatz scales as $F \sim YL^\theta$ where Y is the surface tension of the droplet. The theory then analyzes the relaxation of these excited droplets (of various L) back to the ground state within a scaling framework. The density of states of these excitations scales as $D \sim L^{-\theta}$.

III.3.3.1) Below Lower Critical Dimension: 2D

Below the LCD, θ_2 is assumed to be negative so that many large scale excitations exist at arbitrarily low energy, destroying the spin glass ordering. At temperature T all excitations of the scale YL^{θ_2} and larger occur. The correlation length is therefore defined as the length scale below which the excitations do not destroy the ordering. As $T \rightarrow 0$ the correlation length diverges as

$$\xi \sim \left(\frac{Y}{T}\right)^{\nu_2} \sim L \ , \qquad \textbf{III-8}$$

where $\nu_2 = \frac{1}{|\theta_2|}$.

Fisher and Huse assume that the energy barriers that must be overcome by a droplet of size L for it to relax back to it's unflipped state is

$$B_L \sim L^{\psi_2} \ ,$$

where $L \leq \xi$ and the newly defined critical exponent $0 \leq \psi \leq d-1$.

The relaxation time of these droplets is given by the Boltzman function

$$\tau_L \sim exp\left[\frac{B_L}{k_B T}\right] . \qquad \textbf{III-9}$$

Since the droplets of size ξ are the largest in the system the relaxation time of the full system will be

$$ln\tau \approx \frac{\xi^{\psi_2}}{T} \sim \frac{1}{T^{1+\psi_2\nu_2}} .$$

Experimentally one makes measurements on a time scale t_{exp}. For experimental time scales $\tau << t_{exp}$, the experiment measures the equilibrium properties of the system. On time scales $\tau >> t_{exp}$ the system falls out of equilibrium. This behaviour becomes important in the measurement of the susceptibility.

For time scales on the order of $ln(t_{exp}) << ln(\tau)$ the experiment senses droplets of the size $L \sim [Tln(t_{exp})]^{\frac{1}{\psi_2}}$. The contribution of these droplets to the susceptibilty is

$$\chi(t_{exp}) \sim L^{\theta} \sim [Tln(t_{exp})]^{\frac{1}{\psi_2\nu_2}} \ ,$$

which is a positively increasing function of time. At time $\tau >> t_{exp}$ the system relaxes as if it is at equilibrium and shows Curie-like behaviour $\chi \sim \frac{1}{T}$. χ will then show a maximum when $\tau \sim t_{exp}$ (ie. when the system falls out of equilibrium).

The time scale of the measurement is thus very important. If the dynamic critical exponent z_2 is large so that τ diverges rapidly then there will be a peak in the susceptibility. From Eq. III-9 and the consideration that the peak occurs at $t \sim \tau$ there should exist a peak for $d < d_c$ at

$$T_f(t_{exp}) \sim \left(\frac{1}{ln(t_{exp})}\right)^{\frac{1}{1+\psi_2\nu_2}} \quad , \qquad \text{III-10}$$

which approaches $T_g = 0$ as $t_{exp} \Rightarrow \infty$.

Recent experiments by Dekker et al.[77] on a two dimensional Ising spin glass system, $Rb_2Cu_{.728}Co_{.218}F_4$, have been analyzed within the spin droplet excitation model. As predicted they find a peak in the susceptibility at a temperature which is strongly time dependent. Analyzing their ac susceptibility in a phenomenological Cole-Cole approach, they are able to fit the relaxation time vs. temperature in Eq. III-9 over sixteen decades of time and have found a value of $\psi_2\nu_2 = 2.2 \pm .2$.

III.3.3.2) Cross-over Between Three and Two dimensions

There are two regions of interest: 1) $T << T_g$ 2) $T \sim T_g = T_g^b$

To start the discussion of $T << T_g$ consider a film of thickness w. For length scales of excitations $L < w$ the system will behave three dimensionally so that $F \sim w^{\theta_3}$. Setting $Y(0) \sim T_g = 1$ and rescaling the temperature (free energy) to length scale w one obtains $T_R(w) \sim Tw^{-\theta_3}$. For $L > w$ the system will behave two dimensionally and the excitation size can be broken up into regions of size w. The temperature can then be rescaled as a 2D system as

$$T_R(L) \sim T\left(\frac{L}{w}\right)^{\theta_2} w^{-\theta_3} \; .$$

The 2D system becomes disordered (from III-8) at length scales

$$\xi \sim T^{-\frac{1}{\theta_2}} w^{1+\frac{\theta_3}{\theta_2}} = T^{-\nu_2} w^{1+\nu_2\theta_3} \; .$$

Similarly the barrier energy can be scaled as

$$B_\xi \sim \left(\frac{\xi}{w}\right) w^{\psi_3} \quad , \qquad \text{III-11}$$

yielding relaxation times of order

$$ln\tau \sim T^{-(1+\nu_2\psi_2)} w^{\psi_3+\nu_2\psi_2\theta_3} \ .$$

The system will appear to freeze at a temperature $T_f(t_{exp})$ where $ln(t_{exp}) \sim ln\tau$. For $T_f << T_f$

$$\frac{T_f(t_{exp})}{T_g} \sim \left[\frac{w^{\psi_3+\psi_2\nu_2\theta_3}}{ln(t_{exp})}\right]^{\frac{1}{1+\nu_2\psi_2}} \ . \qquad \text{III-12}$$

This equation describes how the transition temperature behaves in the quasi two dimensional region (ie. very thin films).

We will now examine the thick film region where $T \sim T_g$ For length scales $L << w$ the system looks three dimensional and the free energy scales as $F_L^3 \sim Y_3 L^{\theta_3}$ where $Y_3 \sim |\epsilon|^{\nu_3\theta_3}$ and $\epsilon = (\frac{T-T_g}{T_g})$. For length scales $L >> w$ the system looks two dimensional and the free energy scales as $F_L^2 \sim Y_2 L^{\theta_2}$ The two dimensional surface tension can be found by matching the free energies at the crossover point $L \approx w$.

$$Y_2 w^{\theta_2} \sim Y_3 w^{\theta_3}$$

Using Eq. III-8 this yields a 2D correlation length

$$\xi \sim w^{(1+\nu_2\theta_3)} |\epsilon|^{\nu_3\theta_3\nu_2} \ .$$

From this and Eq. III-11 it is easily seen that the activation barriers for lengths $L \approx \xi$ are

$$B_\xi \sim \left[|\epsilon|^{\nu_3} w\right]^{\psi_3+\nu_2\psi_2\theta_3}$$

At long measuring times $t_{exp} >> \tau \sim w^{z_3}$ the shift freezing temperature will be given by

$$\frac{T_g - T_f(t_{exp})}{T_g} \sim w^{\frac{-1}{\nu_3}} \left[ln\left(\frac{t_{exp}}{w^{z_3}}\right)\right]^{[(\psi_3+\nu_2\psi_2\theta_3)\nu_3]^{-1}} \ , \qquad \text{III-13}$$

from Eq. III-10. To first order this equation is the same as Eq. III-7.

CHAPTER IV

DATA AND ANALYSIS

The preceeding chapters have summed up the experimental characterization of the layered samples and the theories which exist on three to two dimensional crossover in metallic spin glasses. The first section of this chapter starts with a description of the SQUID susceptometer which was used to measure; 1) the magnetic susceptibility as a function of temperature for all of our samples, and 2) the magnetization as a function of magnetic field data for the $Cu_{.93}Mn_{.07}/Si$ MS. There is then a discussion of the magnetic susceptibility vs temperature data on the $Cu_{1-x}Mn_x/Si$ and $Cu_{1-x}Mn_x/Cu$ MS where x = .04, .07, .14 and .21. The transition temperature T_g as a function of spin glass layer thickness is plotted and its main features are discussed.

The second section of this chapter is a theoretical analysis of the magnetic susceptibility data, beginning with a finite size scaling interpretation of the CuMn/Cu and CuMn/Si MS for all concentrations. Mean free path effects on T_g in CuMn/Si MS are looked at in the Quenched Uniform Model.

The third section of this chapter is a discussion of the magnetization vs. magnetic field data.

The chapter is concluded with a general discussion of the relation between the susceptibility results and the concepts of lower critical dimensionality, universality, and dimensional crossover.

IV.1) Magnetic Measurements

IV.1.1) SQUID Magnetometer

Magnetic susceptibility vs temperature and magnetization vs magnetic field measurements were made on a commercial S.H.E. corporation V.T.S. 800 series Superconducting Quantum Interference Device (SQUID) susceptometer. This machine is capable of measuring sample magnetic moments over a wide range of temperatures and magnetic fields with a resolution of $\leq 1\text{x}10^{-7}$ emu.

The 800 series magnetometer is a form of magnetization measuring device known as a fluxmetric magnetometer. In these devices the sample is pulled at a constant rate through two oppositely wound coils. The change in magnetic flux induces a current in the coil circuit related to the sample moment. The advent of SQUID technology allows for very sensitive detection of the coil current.

We have measured magnetic susceptibility vs temperature curves for all of our layered samples. The sample plus substrate had to be cut into .3 cm x 1cm strips in order to fit in the measuring coils. Initially the magnetic field was set to zero and the samples were loaded into the space between the measuring coils, which was at a temperature of 5 K. The magnetic field was then set at 100 gauss or 200 gauss. Magnetic susceptibility measurements were then made at various temperatures between 5 K and 100 K. These measurements are called the zero field cooled (zfc) data. The temperature was then reduced to 5 K, with susceptibility measurements made at various temperatures along the way. These measurements are called the field cooled (fc) data. It was shown by Nogata et al.[78] that the spin glass transition temperature could be determined from the peak in the zfc 'D.C.' susceptibility vs. temperature curve. D.C. susceptibility usually refers to susceptibility measurements made on time scales greater then 1s. In most types of magnetic systems, measuring time scales of $> 1s$ correspond to equilibrium measurements. As Edwards and Anderson[51] have pointed out (Ch.III.3.3), time scales of this magnitude do not necessarily correspond to an equilibrium state in a spin glass. The rounded spin glass transition peak limits the determination of the spin glass transition temperature to ±1 K.

Magnetization as a function of magnetic field was measured on several of our $Cu_{.93}Mn_{.07}/Si$ MS, to look for changes in the anisotropy field as a function of layer thickness, These measurements were made at a fixed temperature in fields up to 6 kG.

IV.1.2) Magnetic Susceptibility Data

Figs. IV-1 and IV-2 show sample plots of the zfc and fc data for several of the $Cu_{.86}Mn_{.14}/Cu$ and $Cu_{.86}Mn_{.14}/Si$ MS, respectively. These curves are representative of the susceptibility data of all of our CuMn/Cu and CuMn/Si MS. It can be seen that all of the zfc curves have peaks reminiscent of typical spin glasses. The peak position is defined as the spin glass transition temperature T_g. Starting from $T = 0\ K$ the zfc curves increase with increasing temperature up to T_g , with occasional evidence of anomalous increases in the susceptibility. We interpret these anomalous increases as time dependent effects (caused by different measuring times per temperature point) as the susceptibility tries to approaches the (nominally) equilibrium fc susceptibility (in the regime where the relaxation time approximates our measuring time) as time → ∞. Above T_g, the zfc susceptibility exhibits Curie-like behaviour (ie. $\chi \sim \frac{1}{T}$).

Above T_g, the fc susceptibility is also Curie like but slightly larger than the zfc susceptibility at the same temperature. By comparing the zfc and fc curves of a standard Pt sample we have found that this difference between the curves is due to a systematic machine error. In bulk spin glass materials the fc susceptibility below T_g is nominally constant[4]. It has been suggested that the fc state is the true

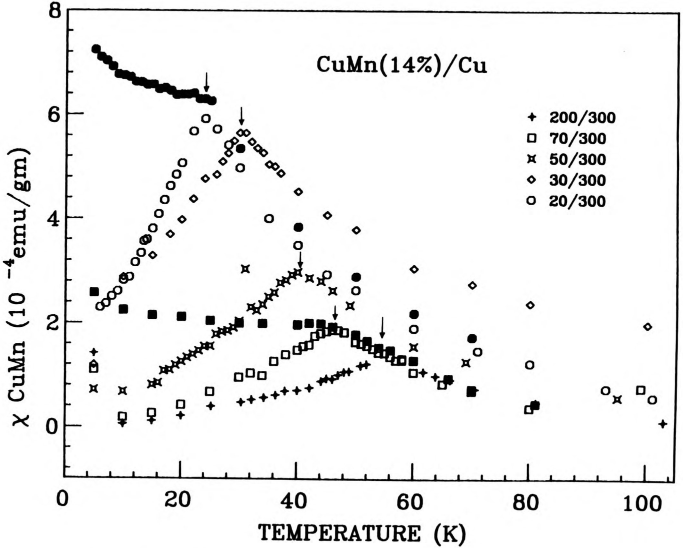

Figure IV-1: Magnetic susceptibility vs temperature for the $Cu_{.86}Mn_{.14}/Cu$ MS. Open symbols correspond to zero field cooled. Solid symbols correspond to field cooled. Arrows indicate the transition temperature.

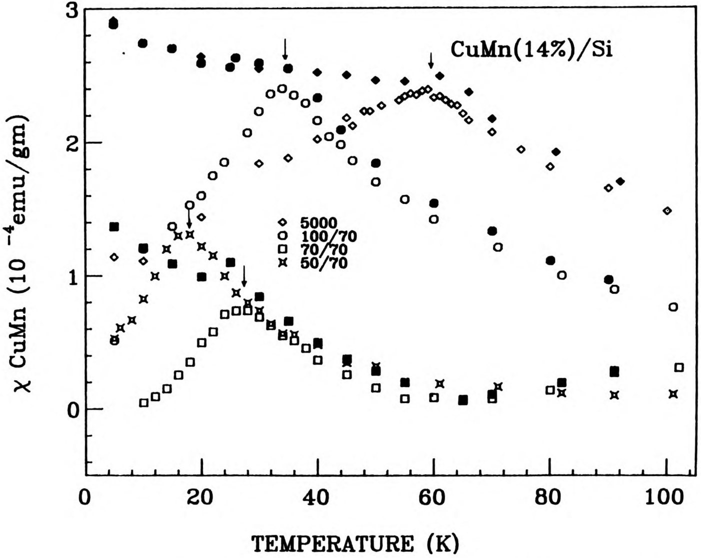

Figure IV-2: Magnetic susceptibility vs temperature for the $Cu_{.86}Mn_{.14}/Si$ MS. Open symbols correspond to zero field cooled. Solid symbols correspond to field cooled. Arrows indicate the transition temperature.

equilibrium state of the spin glass[26]. In our samples we generally observe that the fc susceptibility decreases slightly below T_g and then increases as T approaches zero.

The sharpness of the susceptibility peak appears to increase as the L_{CuMn} is decreased. This however is an artifact of the decrease in T_g with decreasing L_{CuMn} (since $\chi = 0$ at $T = 0$ for the zero field cooled curve). A more appropriate measurement of the peak width would involve normalizing the width by dividing each temperature by the transition temperature. When the normalized zfc susceptibility curves are plotted (Fig. IV-3) we cannot resolve any difference in the widths of the susceptibility peaks, to within experimental resolution.

The absolute values of the fc susceptibility ($T >> T_g^L$) of all the CuMn/Cu MS appear to follow similar Curie behaviour, corresponding to approximately the same number of paramagnetic moments. The differences in the susceptibility may be due to differences in susceptibility of the individual Si substrates backing the samples. These substrates are diamagnetic and have an approximately constant susceptibility of $-1x10^{-4}$ emu/gm, over the range of temperature considered in this study.

In contrast the absolute values of the susceptibility of the CuMn/Si MS are quite different from each other and do not appear to depend on the CuMn layer thickness. At this point it is unclear as to what is causing these differences. It is clear, however, that the absolute values of the susceptibility are the same order of magnitude as the CuMn/Cu MS, suggesting that the formation of silicides (MnSi; $\mu = 1.1\mu_B$[79], Mn; $\mu = 5.5\mu_B$[80]) is not extensive.

To determine what interlayer thicknesses of Cu and Si were sufficiently large to magnetically decouple the spin glass layers from each other, samples with varying interlayer thicknesses were made. Fig. IV-4 shows a plot of T_g vs. interlayer thickness for a fixed alloy thickness of 100 A^o in the $Cu_{.96}Mn.04/Cu$ MS. It is observed that no significant deviation from the transition temperature T_g^L occurs down to $L_{Cu} = 100A^o$. $300A^o$ of Cu was used to magnetically decouple the spin glass layers. Fig. IV-5 shows the variation of T_g with Si thickness in the CuMn/Si

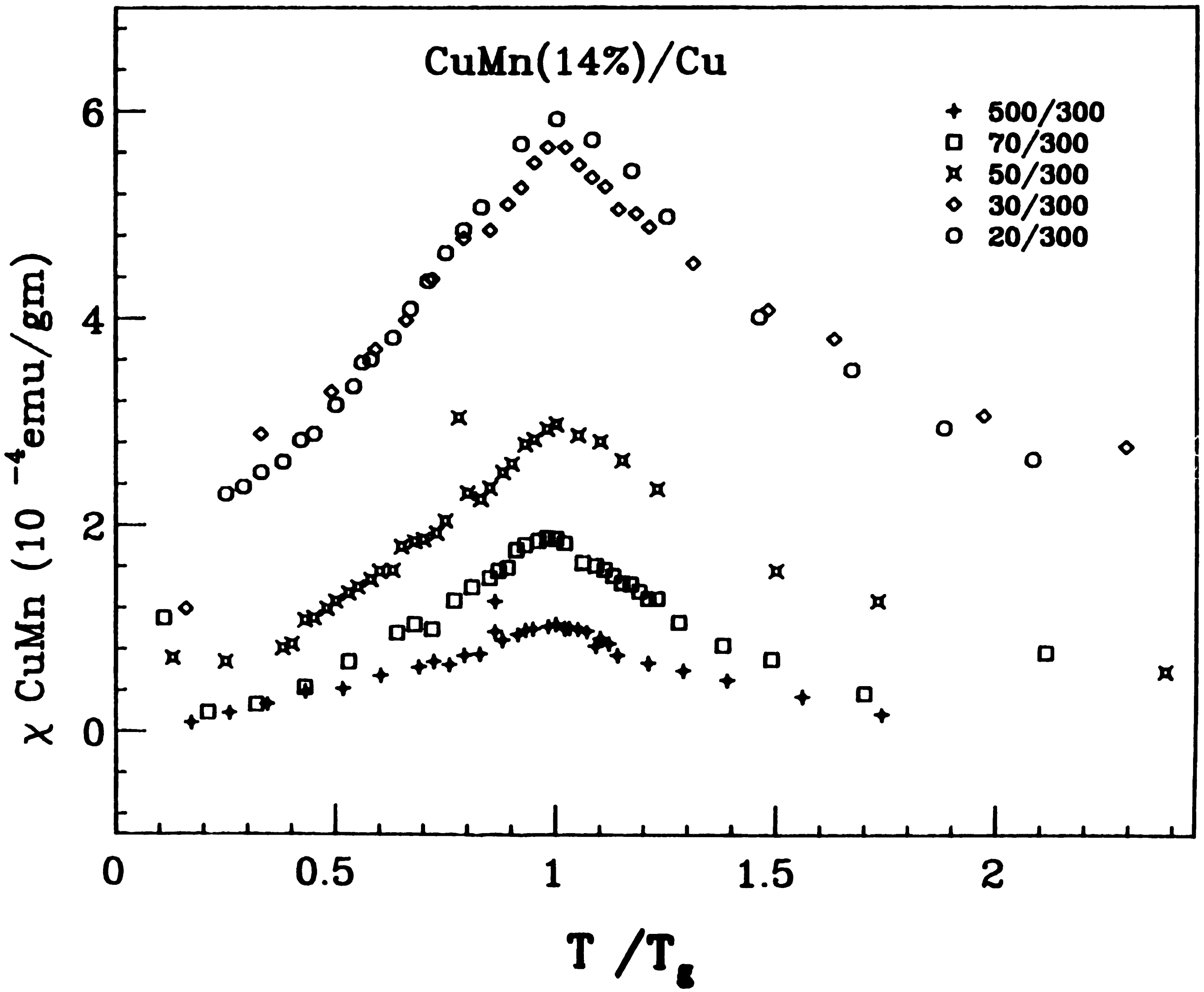

Figure IV-3: Magnetic susceptibility vs normalized temperature $\frac{T}{T_g}$ for the $Cu_{.86}Mn_{.14}/Cu$ MS.

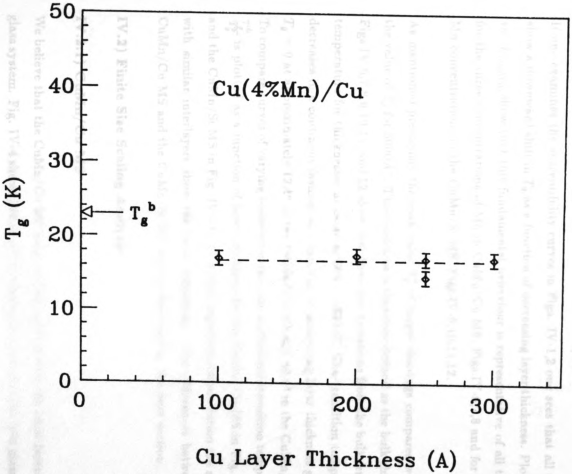

Figure IV-4: Transition temperature (fixed L_{CuMn}) T_g vs Cu interlayer thickness L_{Cu} for the $Cu_{.96}Mn_{.04}/Cu$ MS.

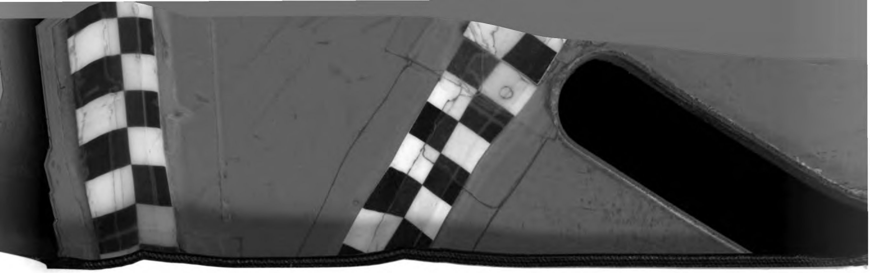

MS. SAXD confirms good layering down to $L_{Si} = 30A^o$ but no layering is observed for $L_{Si} = 20A^o$. The transition temperature T_g^L remains constant down to 30 A^o (Fig IV-5) but begins to shift upward towards the bulk transition temperature for $L_{Si} = 20A^o$ and $10A^o$.

If one examines the susceptibility curves in Figs. IV-1,2 one sees that all samples show a downward shift in T_g as a function of decreasing layer thickness. Plots of Tg vs. L_{CuMn} show that this fundamental behaviour is representative of all the data for the three concentrations of Mn in CuMn/Cu MS, Figs.IV-6,7,8 and for all four Mn concentrations in the CuMn/Si MS, Figs.IV-9,10,11,12.

As mentioned previously the bulk value T_g^b of target shavings compares well with the value of T_g for $5000A^o$. This thickness is therefore defined as the bulk thickness. Figs IV-6,7,8,9,10,11, and 12 show that there are deviations from the bulk transition temperature for thicknesses as large as $500 - 1000A^o$. The transition temperature decreases in a continous fashion as a function of decreasing layer thickness going to $T_g = 0$ at approximately $12A^o$ in the CuMn/Cu MS and $40A^o$ in the CuMn/Si MS. To compare curves of varying concentrations, the normalized transition temperature $\frac{T_g^L}{T_g^b}$ is plotted as a function of layer thickness for the CuMn/Cu MS in Fig. IV-13, and the CuMn/Si MS in Fig. IV-14. To within experimental resolution the samples with similar interlayers show the same behaviour. The differences between the CuMn/Cu MS and the CuMn/Si MS will be discussed in the next section.

IV.2) Finite Size Scaling Analysis

IV.2.1) CuMn/Cu MS

We believe that the CuMn/Cu MS most closely approximate the ideal layered spin glass system. Fig. IV-4 shows $300A^o$ of Cu effectively separates the spin glass layers magnetically from each other. The systems are not contaminated by impurities (ie. Si) and the Fermi surfaces should be similar to three dimensional Cu with small deviations due to the Mn impurities and grain boundaries due to the polycrystalline

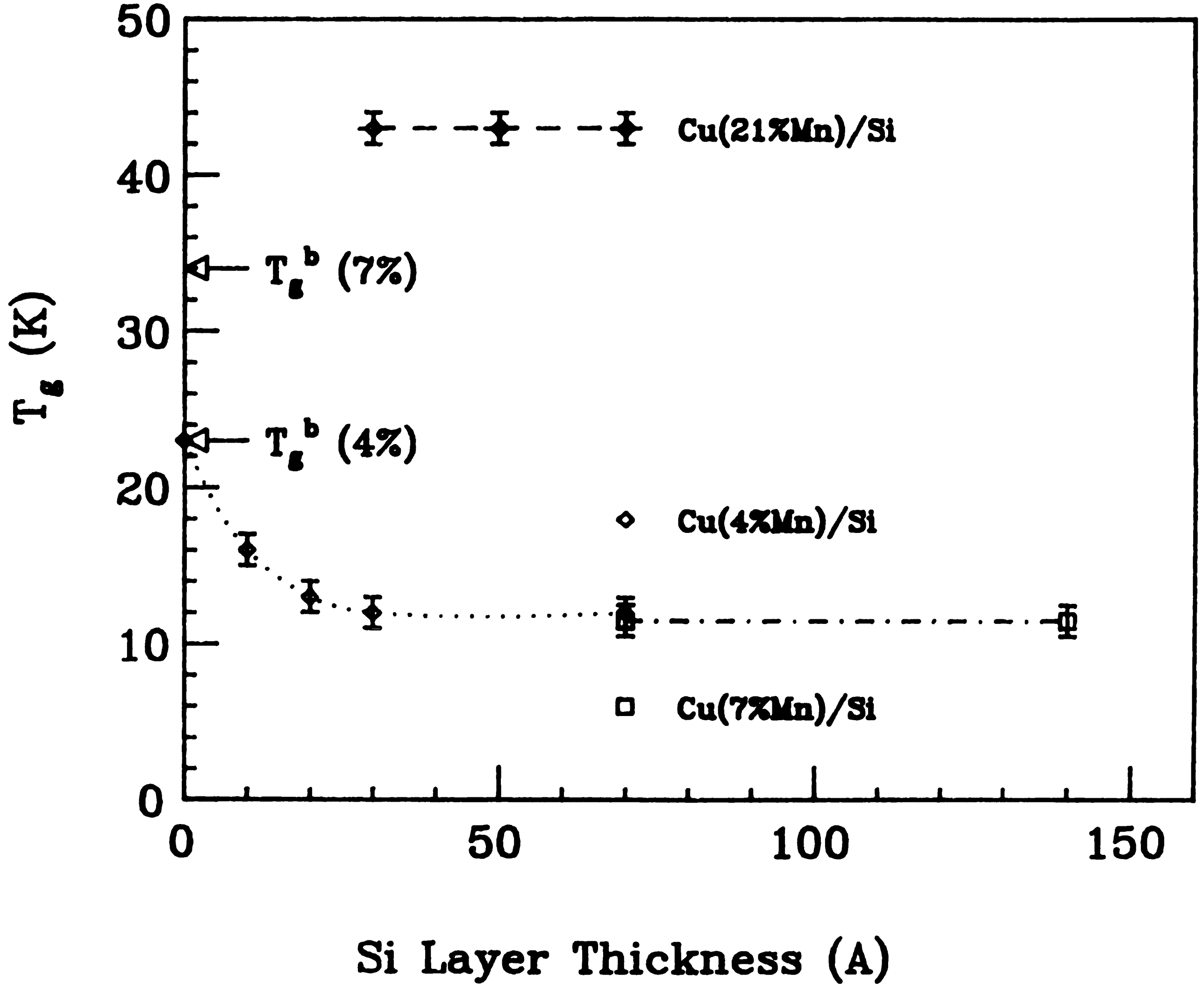

Figure IV-5: Transition temperature (fixed L_{CuMn}) T_g vs Si interlayer thickness L_{Si} for the $Cu_{.96}Mn_{.04}/Si$, $Cu_{.96}Mn_{.04}/Si$, and $Cu_{.96}Mn_{.04}/Si$ MS.

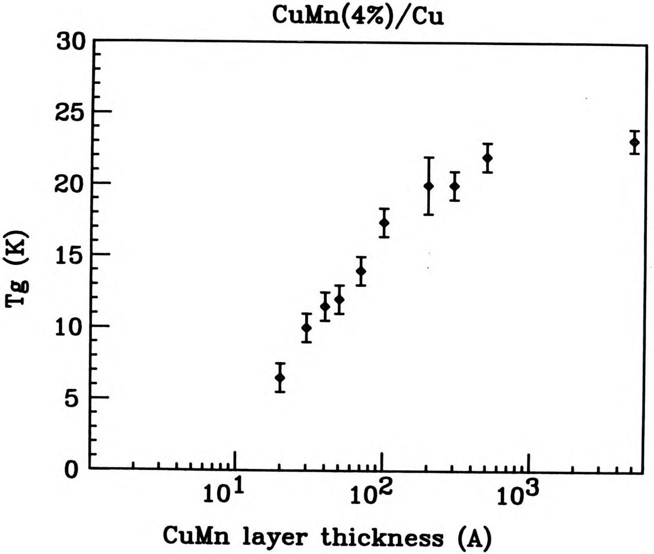

Figure IV-6: Transition temperature T_g vs CuMn layer thickness L_{CuMn} for the $Cu_{.96}Mn_{.04}/Cu$ MS.

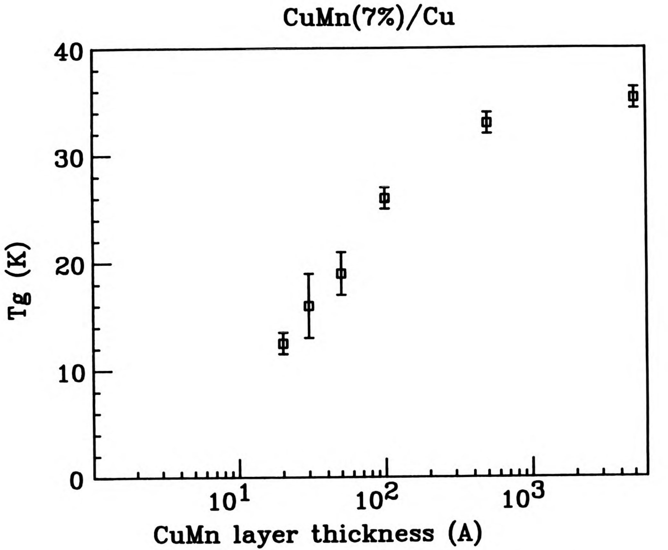

Figure IV-7: Transition temperature T_g vs CuMn layer thickness L_{CuMn} for the $Cu_{.93}Mn_{.07}/Cu$ MS.

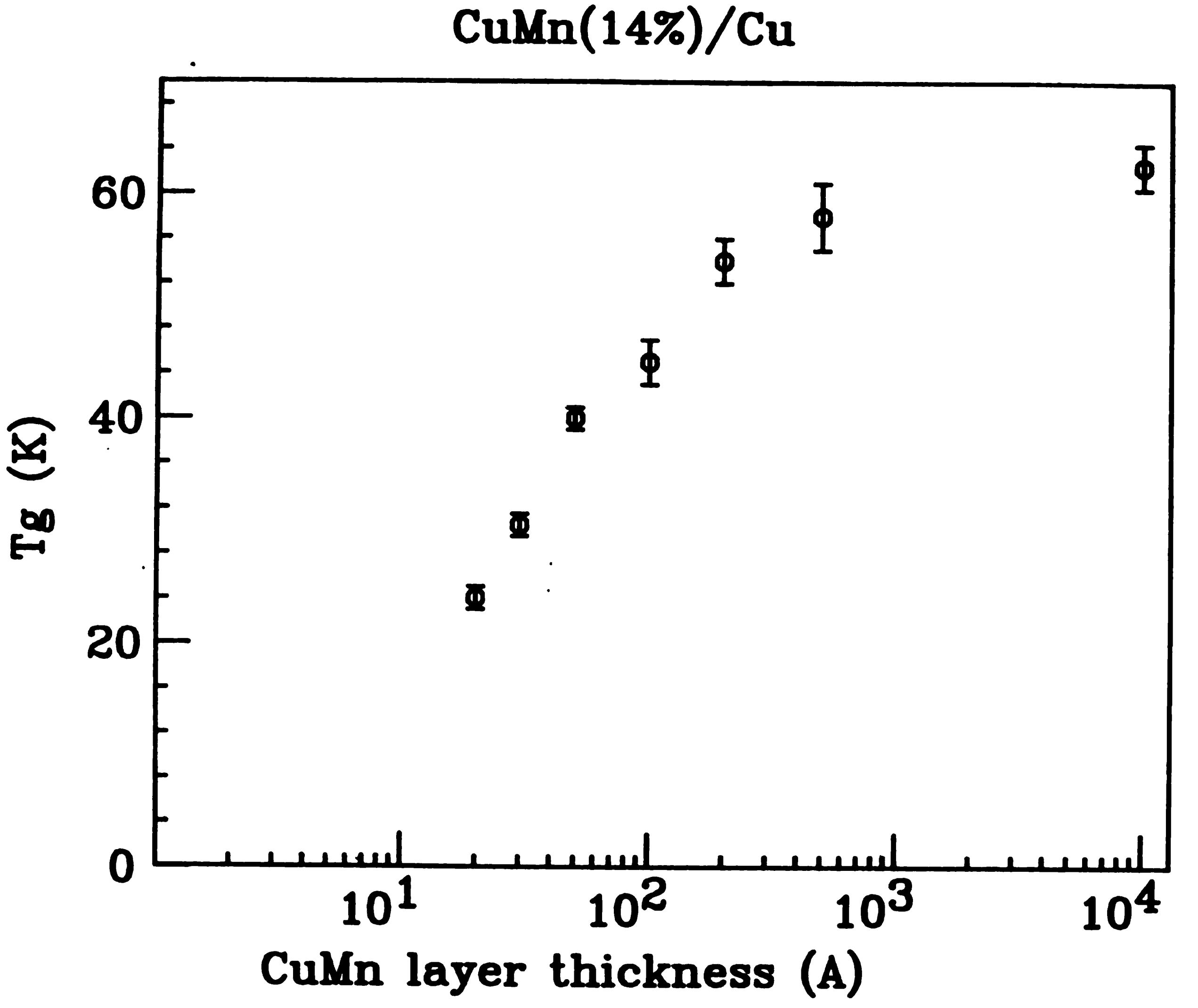

Figure IV-8: Transition temperature T_g vs CuMn layer thickness L_{CuMn} for the $Cu_{.86}Mn_{.14}/Cu$ MS.

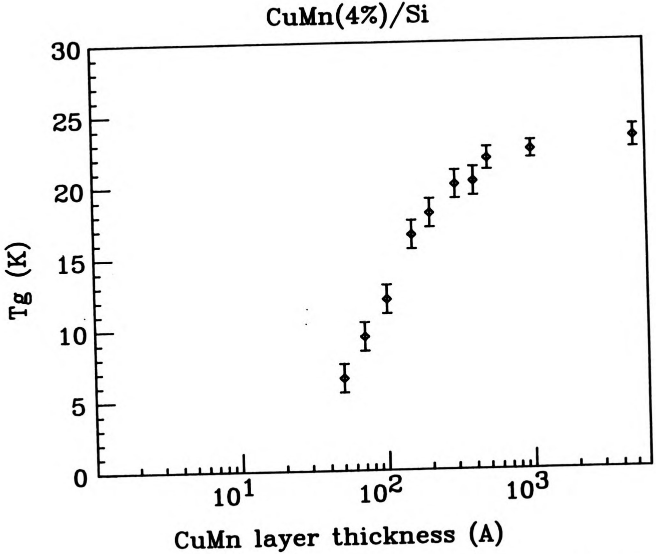

Figure IV-9: Transition temperature T_g vs CuMn layer thickness L_{CuMn} for the $Cu_{.96}Mn_{.04}/Si$ MS.

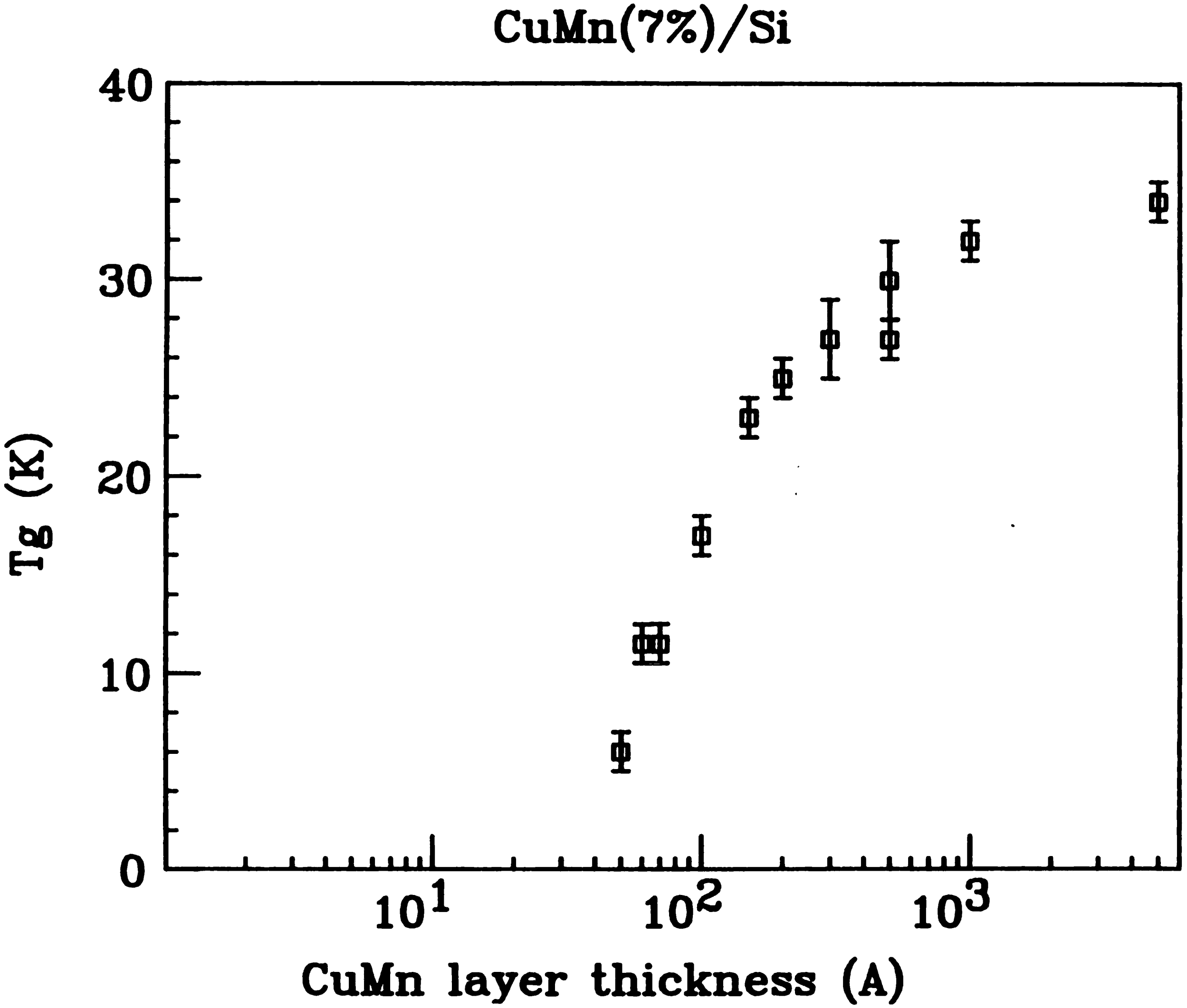

Figure IV-10: Transition temperature T_g vs CuMn layer thickness L_{CuMn} for the $Cu_{.93}Mn_{.07}/Si$ MS.

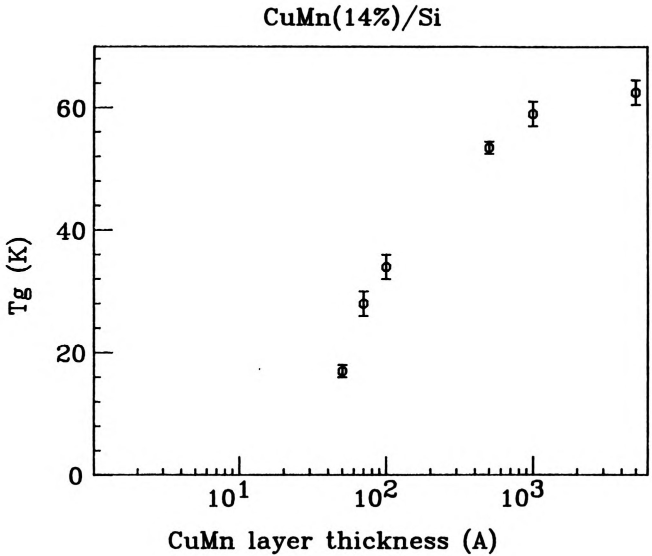

Figure IV-11: Transition temperature T_g vs CuMn layer thickness L_{CuMn} for the $Cu_{.86}Mn_{.14}/Si$ MS.

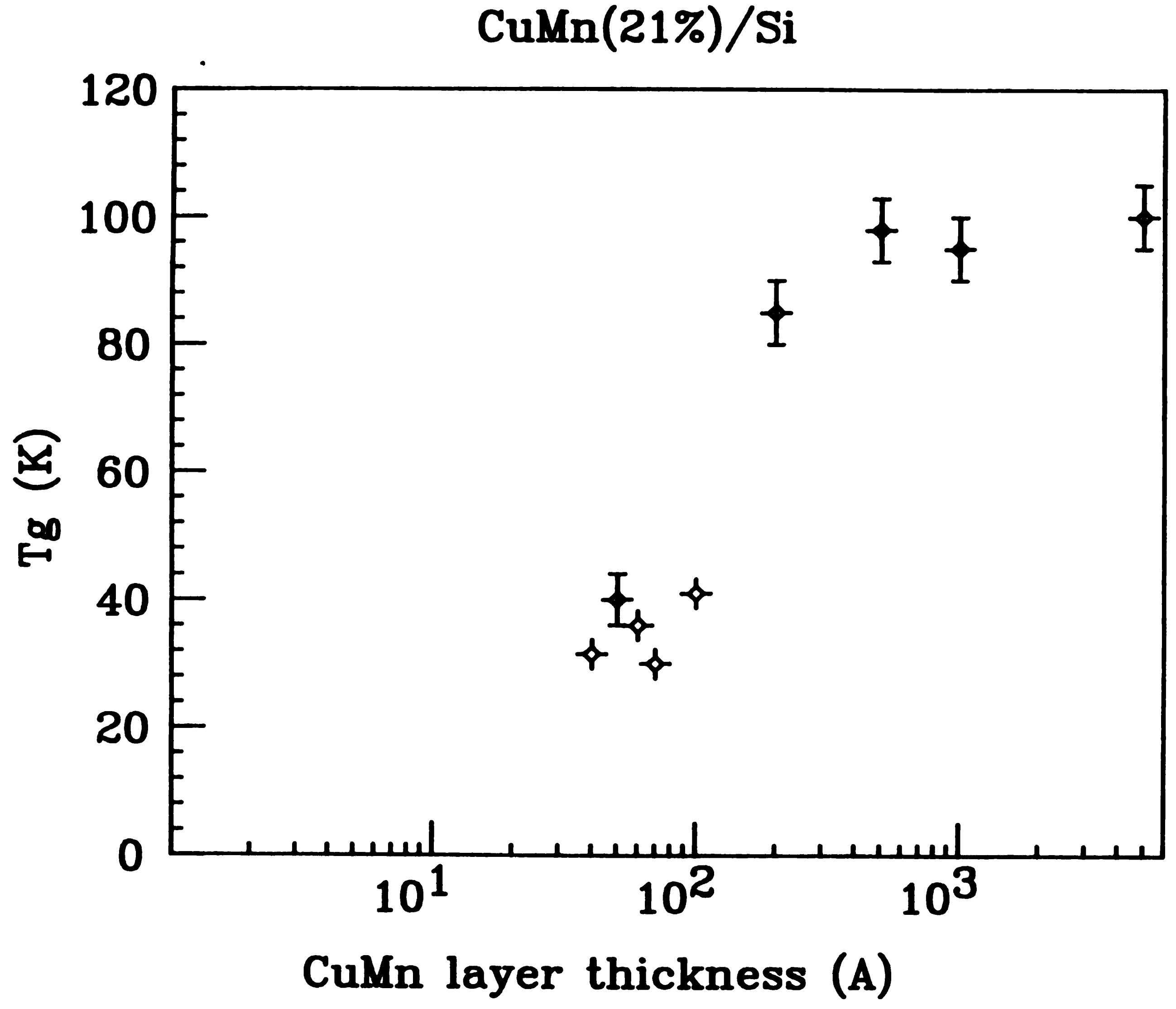

Figure IV-12: Transition temperature T_g vs CuMn layer thickness L_{CuMn} for the $Cu_{.79}Mn_{.21}/Si$ MS.

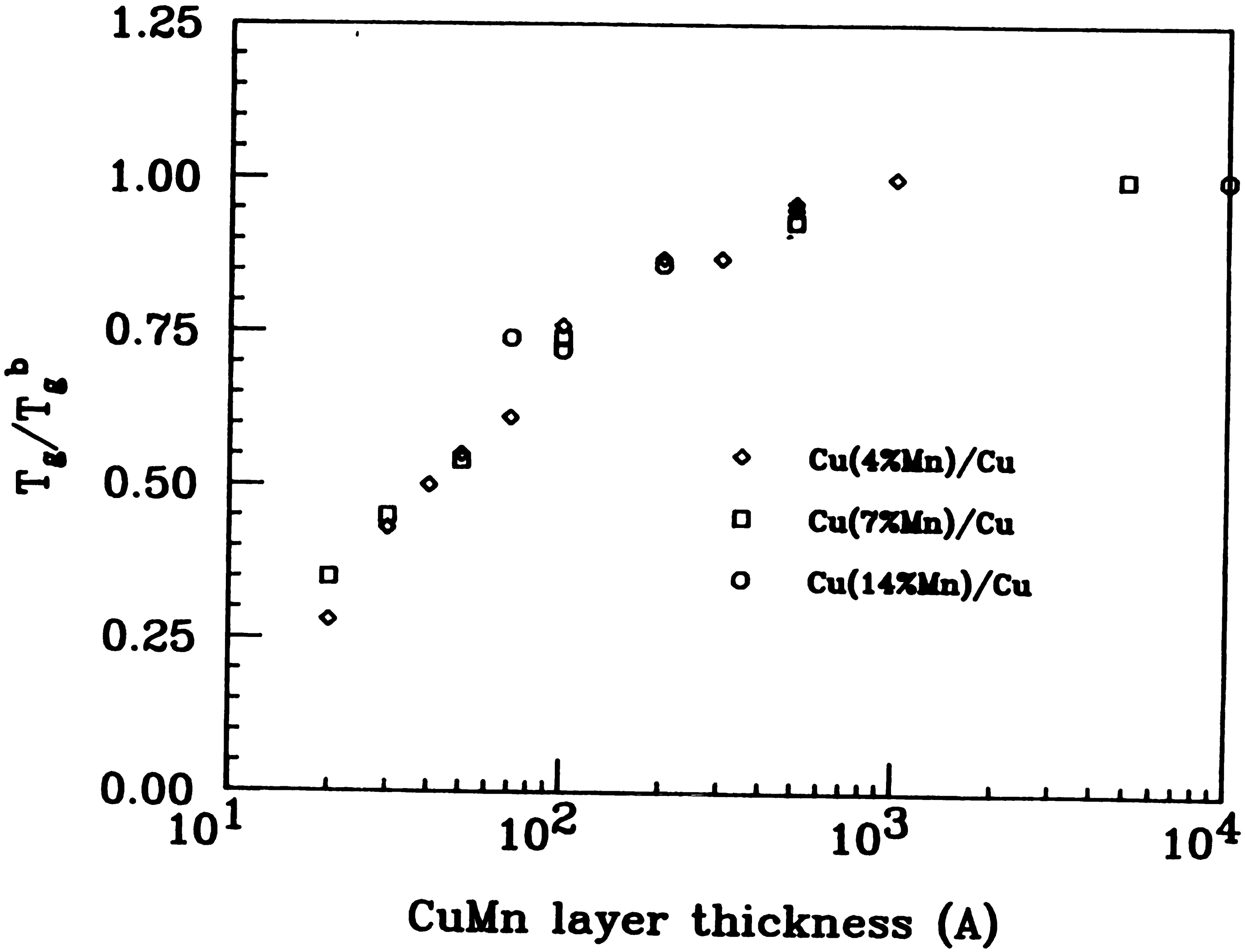

Figure IV-13: Normalized transition temperature $\frac{T_g}{T_g^b}$ vs CuMn layer thickness L_{CuMn} for all of the $CuMn/Cu$ MS.

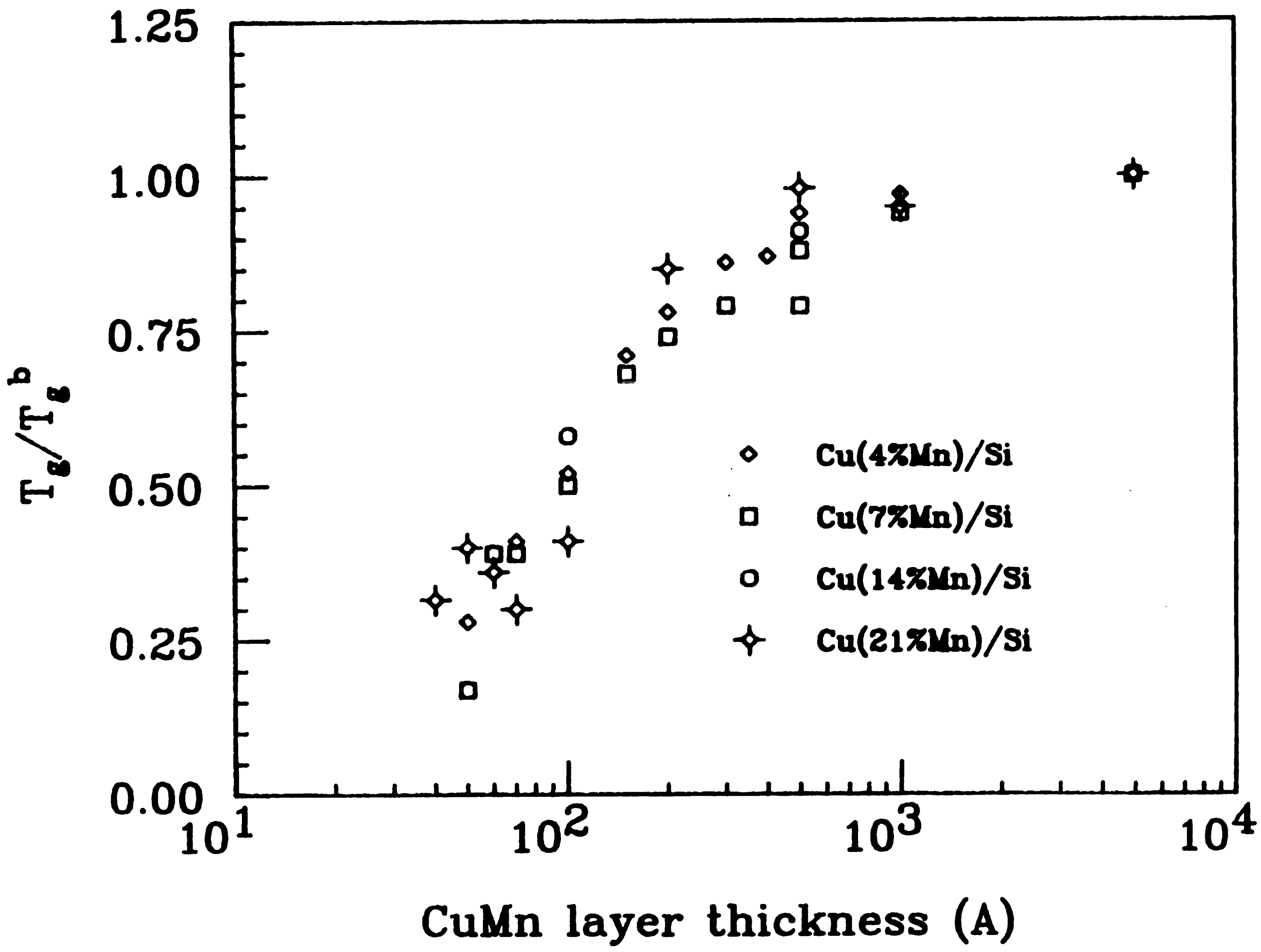

Figure IV-14: Normalized transition temperature $\frac{T_g}{T_g^b}$ vs CuMn layer thickness L_{CuMn} for all of the $CuMn/Si$ MS.

nature of the MS. The structural characterization of these samples, presented in Chapter II, suggests that the layers are polycrystalline and that the diffusion of Mn out of the CuMn layer is small. For the following analysis we will assume that this diffusion is negligible. The data for the three Mn concentrations in CuMn/Cu MS have been fit (Figs.IV-15,16,17) to the form

$$\epsilon = \left(\frac{T_g^b - T_g^L}{T_g^b}\right) \sim AL^{-\lambda}.$$

All three of the critical exponents λ are within error of each other. The non-universal parameters A have values of 5.1, 2.9, and 4.7 (for the 4, 7 and 14 percent Mn samples, respectively). The CuMn thicknesses where $L_{CuMn} \rightarrow 0$ are 12.9 A^o, 8.6 A^o, and 9.3 A^o for the three concentrations (respectively).

Although the only spin glass used in this study was CuMn, in the range of concentrations 4 - 14 percent the material changes a great deal. Statistically, the average number of impurities in the nearest neighbor nn, and next nearest neighbor nnn sites, to a selected impurity increases by 350 percent. If the analysis of Jaganathan et al.[71] is correct, the RKKY interaction should be similar in all of these materials with some deviation due to impurity concentration effects on the Fermi surface. The increase in nn and nnn increases the bulk transition temperature T_g^b by about 300 percent. The amount of frustration felt by each spin increases as the number of nn and nnn neighbors increases. The increase in the nnn will also increase the amount of short range ferromagnetic ordering.

The aforementioned differences in materials of different concentrations coupled with the similarity of the exponents λ leads us to conclude that the exponent λ is a universal critical exponent as postulated.[75] The best value of λ, obtained by fitting all of the data to a single exponent is $\lambda = .7 \pm .05$ (Fig.IV-18). We therefore expect to see similar behaviour in all metallic spin glasses such as AgMn, AuFe etc., which should all belong to the same universality class. The value of $\nu = \frac{1}{\lambda} = 1.72 \pm .15$ that we have obtained is compared with the value of $\nu = 1.3 \pm .2$ obtained by Levy

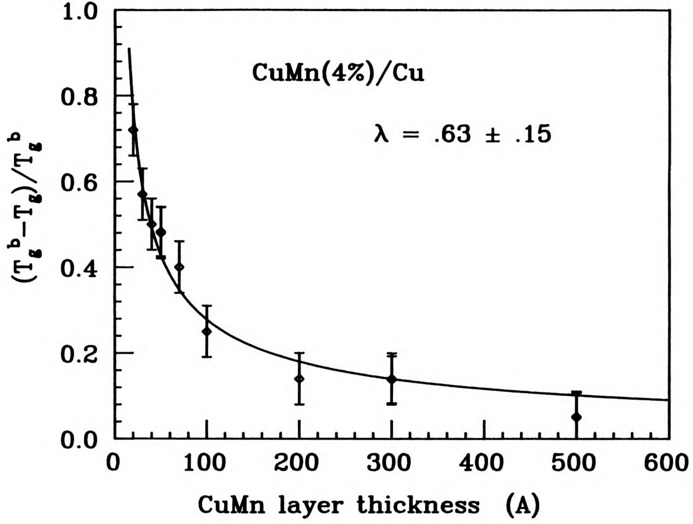

Figure IV-15: Fit of $\epsilon = \frac{T_g^b - T_g}{T_g^b}$ vs L_{CuMn} for $Cu_{.96}Mn_{.04}/Cu$ MS.

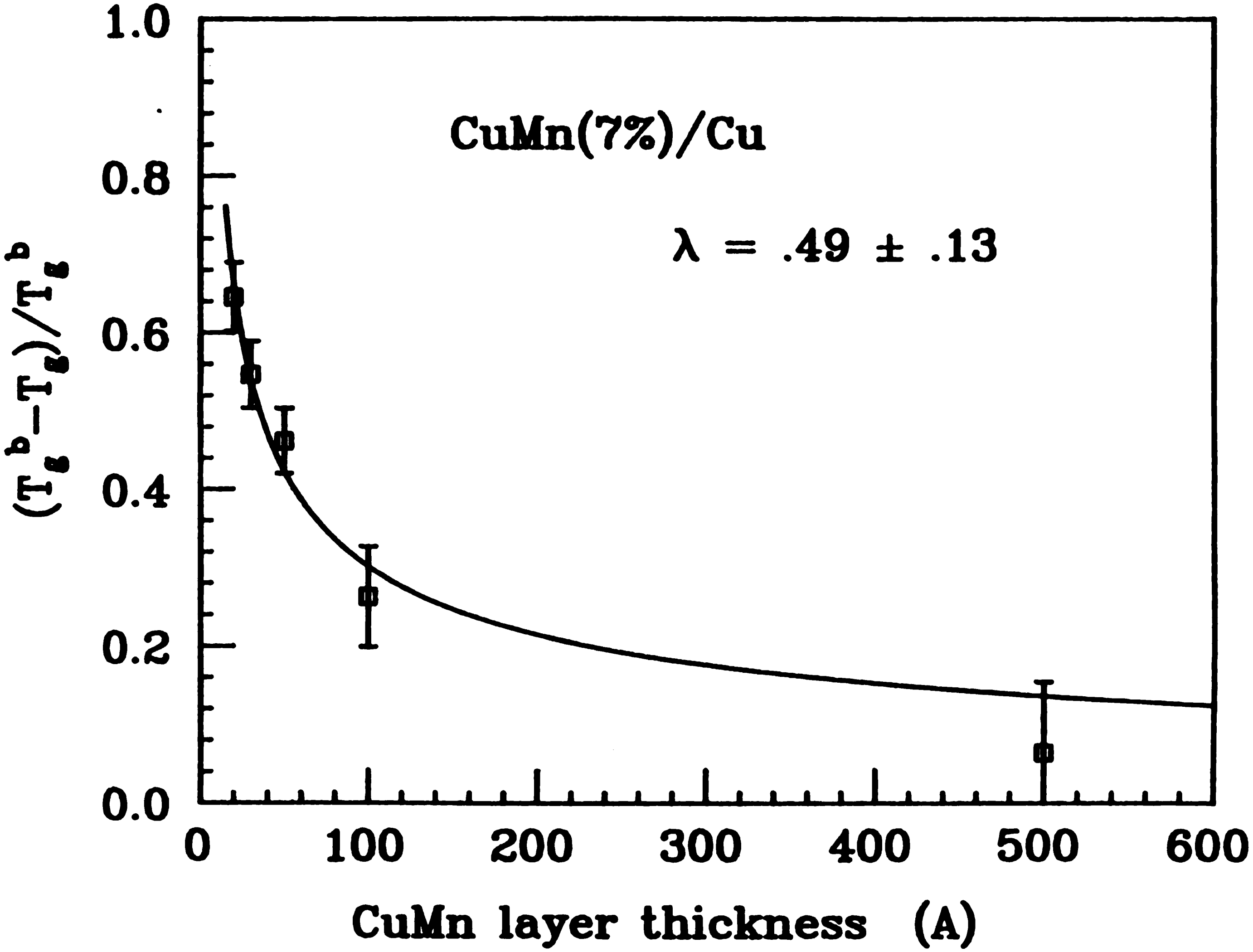

Figure IV-16: Fit of $\epsilon = \frac{T_g^b - T_g}{T_g^b}$ vs L_{CuMn} for $Cu_{.93}Mn_{.07}/Cu$ MS.

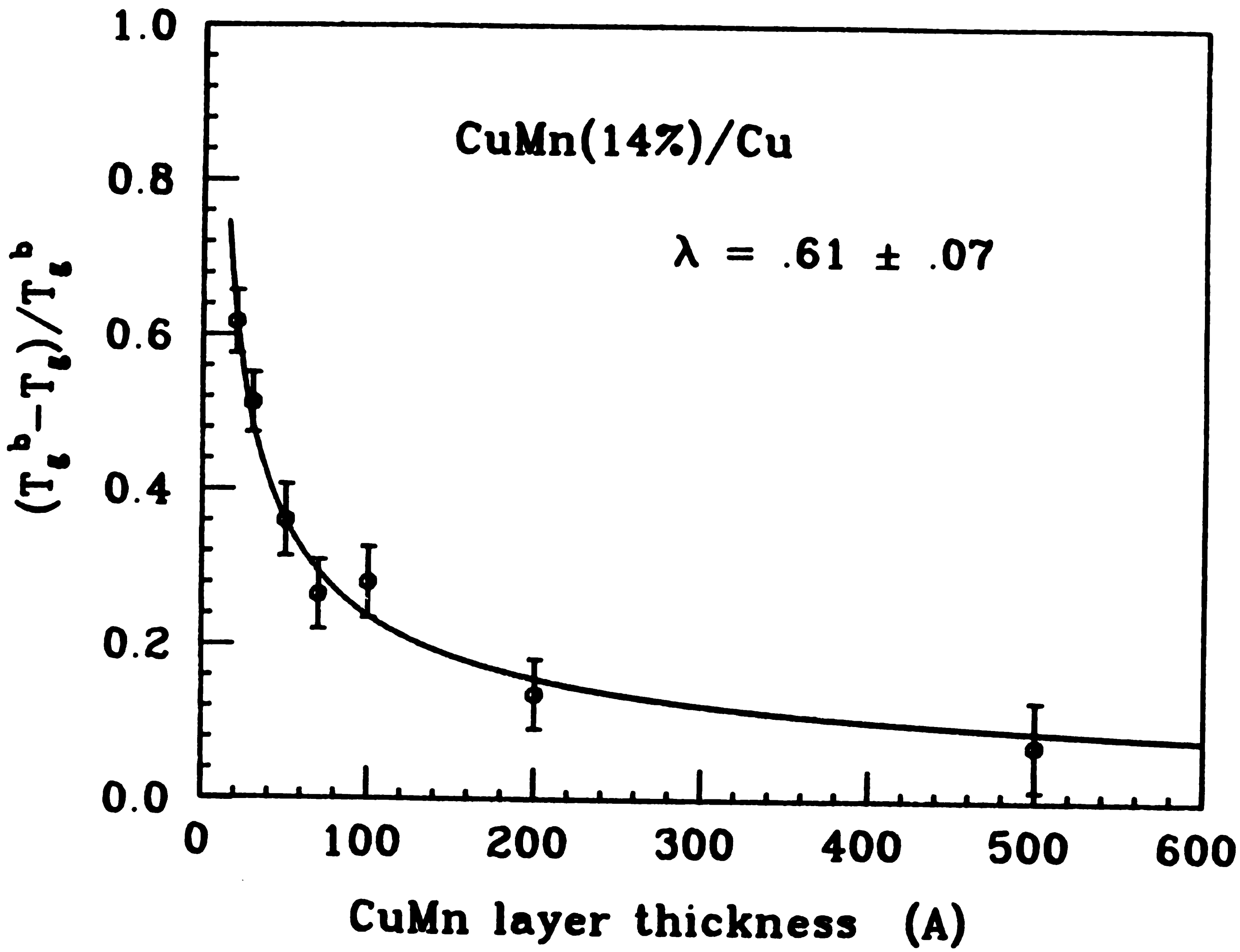

Figure IV-17: Fit of $\epsilon = \frac{T_g^b - T_g}{T_g^b}$ vs L_{CuMn} for $Cu_{.86}Mn_{.14}/Cu$ MS.

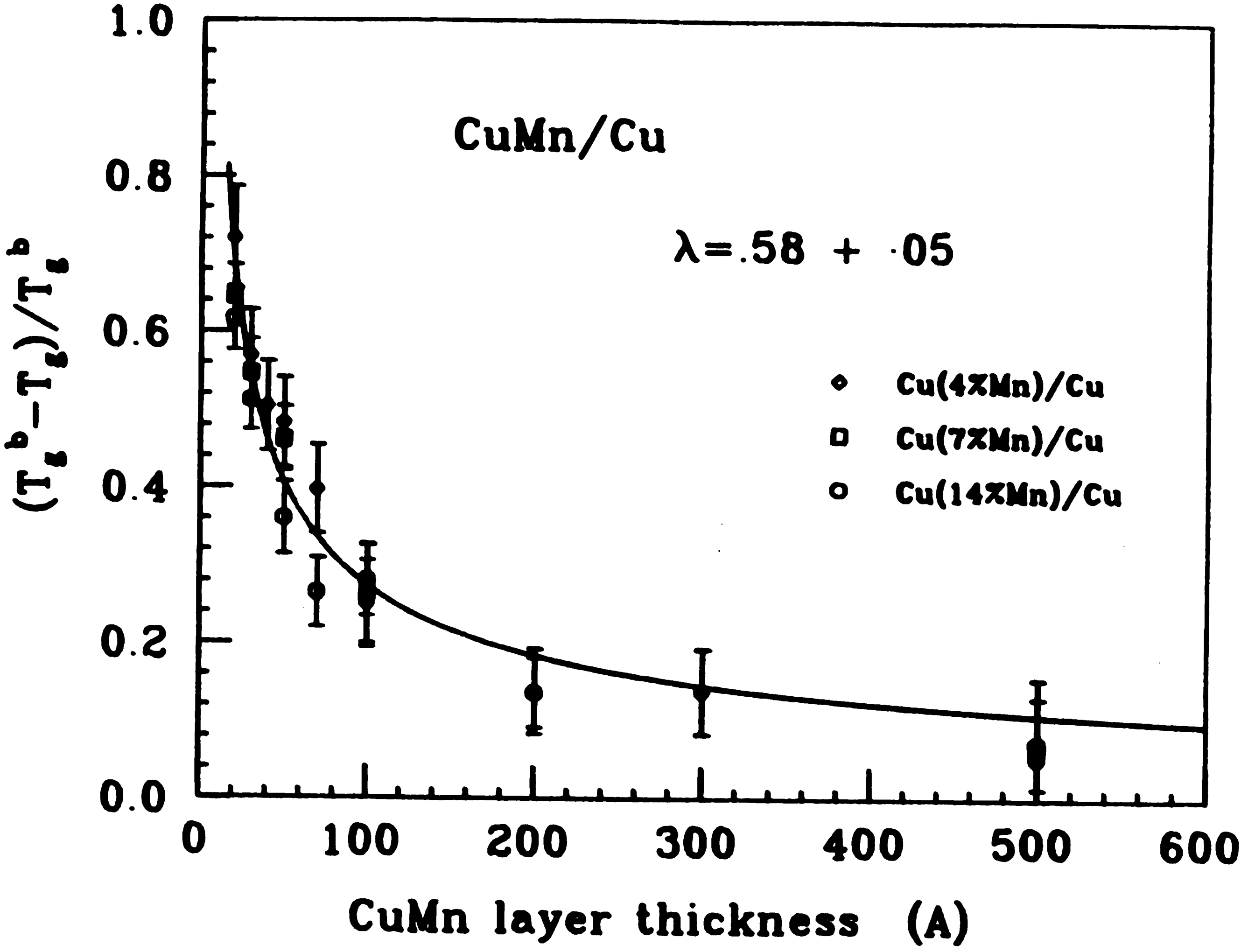

Figure IV-18: Fit of $\epsilon = \frac{T_s^b - T_s}{T_s^b}$ vs L_{CuMn} for all of the $CuMn/Cu$ MS.

et al.[11] from non-linear susceptibility experiments, and the value of $\nu = 1.2 \pm .1$ obtained by Ogielski and Morgenstern[56] on simulations of Ising spin glasses. This similarity to the Ising model is intriguing, but it is not clear that these systems are in the same universality class. Finite size effects should become evident when the correlation length equals the limiting sample size. In our samples this occurs in the region $L_{CuMn} = 500 \rightarrow 1000\ A^o$. This agrees well with the value of $\xi \approx 2000\ A^o$ which Levy and Ogielski[11] have infered from their experiments on AgMn.

Finite size scaling analysis of phase transition systems where the dimensionality is reduced predicts rounding of divergent behaviour, due to restriction of the correlation length in the directions of the reduced dimensions. As mentioned previously we see no evidence of rounding in the widths of the normalized D.C. susceptibility. These peaks however are not divergent even in zero field. A more appropriate experiment to measure rounding behaviour would be be the non-linear susceptibility.

The lack of noticeable rounding in the susceptibility is disconcerting, especially since the exponent which determines rounding behaviour, θ, is postulated to be equal to the shift exponent λ, and we have applied the scaling analysis over a large variation in L_{CuMn}. One possible explanation to the lack of observed rounding is given by the analysis of Fisher and Huse.[54] They suggest that the scaling analysis we have used ($\epsilon \sim L_{CuMn}^{-\lambda}$) is relevant only for our thickest samples.

For an infinite measuring time in a 2D film, the susceptibility should show Curie-like behaviour all the way down to T=0. In the thin film region ($L_{SG} \rightarrow 0$), the peak in the susceptibility is a manifestation of the system falling out of equlibrium with the measuring time scale. In this limit the apparent freezing temperature has been derived as a function of measuring time and film thickness (Ch.III.3.3),

$$\frac{T_f(t_m)}{T_g} \sim \left[\frac{L^{\psi_3 + \psi_2 \nu_2 \theta_3}}{ln(t_m)} \right]^{\frac{1}{1+\nu_2 \psi_2}} .$$

We observe behaviour in Fig. IV-1 reminiscent of the CuMn/Cu MS following similar Curie-like curves and falling away from the Curie curve as a function of

L_{CuMn}. Assuming that $L_{CuMn} \leq 200\ A^o$ is the thin film region and knowing that our measuring times are approximately constant ($\approx 400s$), we obtain a value of

$$\frac{\psi_3 + \psi_2 \nu_2 \theta_3}{1 + \nu_2 \psi_2} = .38 \pm .03\ .$$

Fitting our data to the scaling relation $\epsilon \sim L^{-\lambda}$ in the large L_{CuMn} region ($L_{CuMn} > 200\ A^o$) we obtain a value of $\lambda = 1.1 \pm .3$. Unfortunately we have not been able to measure T_g^L accurately enough to observe the logarithmic corrections predicted for the crossover between the thin and thick film regions.

IV.2.2) CuMn/Si MS

Figs. IV-19, 20, and 21 shows fits to λ of the $Cu_{1-x}Mn_x/Si$ MS for x=.04, .07 and .14. All values of λ obtained in these fits are slightly larger then those determined in the CuMn/Cu MS and within experimental error of each other. The fit to all of the CuMn/Si data is shown in Fig. IV-22. The CuMn thicknesses where $L_{CuMn} \rightarrow 0$ are 36.6 A^o, 37.8 A^o, and 33.3 A^o for x=.04, .07 and .14 (respectively).

We have excluded the $Cu_{.79}Mn_{.21}/Si$ MS from this scaling analysis for the following reasons. 1) After sputtering, the target showed signs of inhomogeneities. 2) The resistivities were extremely dependent on the sputtering run in which they were made. 3) Although the T_g^L show behaviour qualitatively similar to the other CuMn/Si MS, there appears to be a sputtering run dependence.

It has already been established (II.2.4) that the Si in the CuMn/Si MS is entering the CuMn layer. These impurities increase the resistivity of the alloy layer, thereby decreasing the average elastic electron mean free path. To get an estimate of the effects of the increased resistivity on the transition temperature T_g^L we have developed the Uniform Quenched Model (UQM) in a layered geometry (III.3.3.).

It has been shown[70] that the introduction of non-magnetic impurities into an RKKY mediated spin glass reduces the transition temperature from that of the pure alloy. Estimating this reduction can be done by introducing an exponential damping of the form

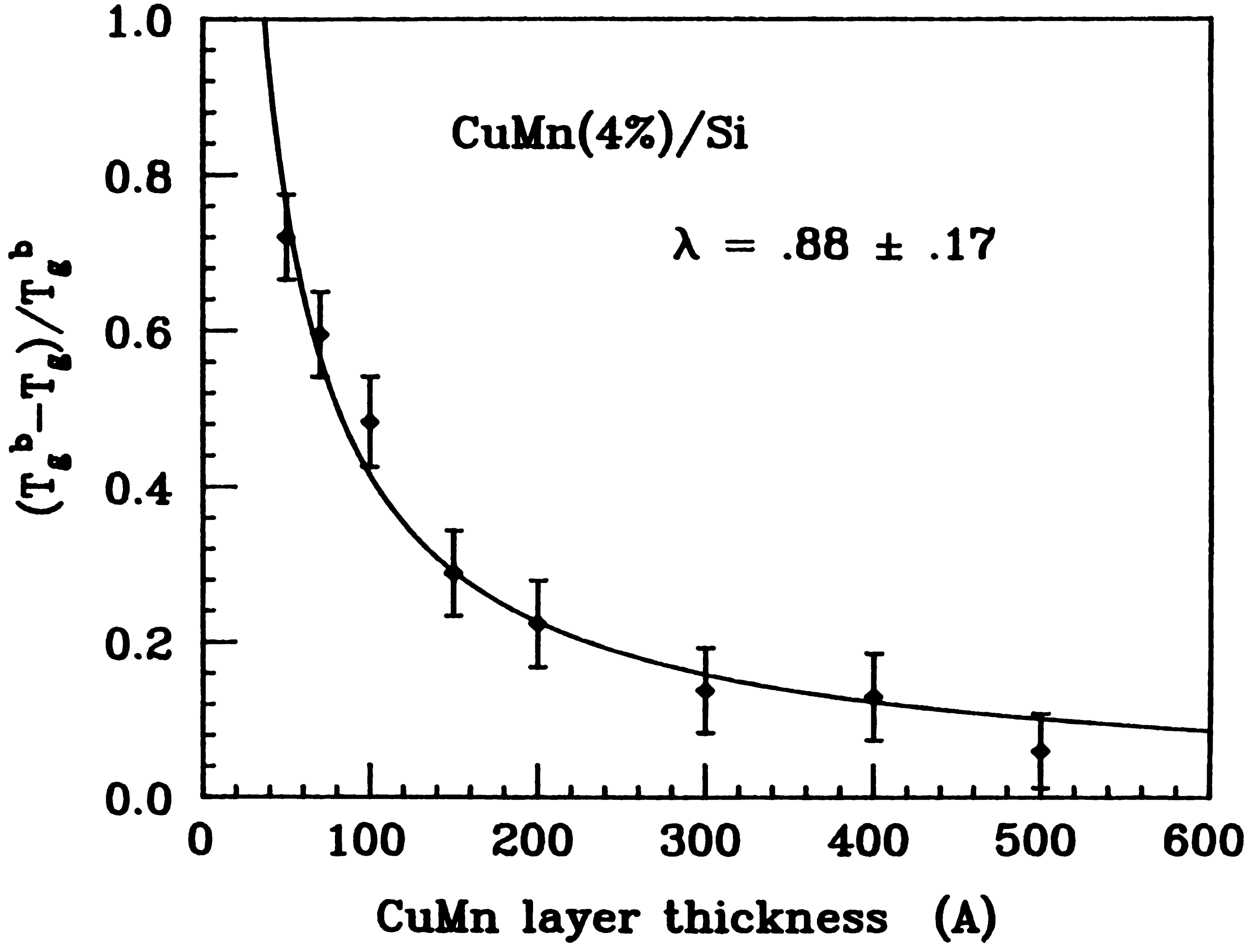

Figure IV-19: Fit of $\epsilon = \frac{T_g^b - T_g}{T_g^b}$ vs L_{CuMn} for $Cu_{.96}Mn_{.04}/Si$ MS.

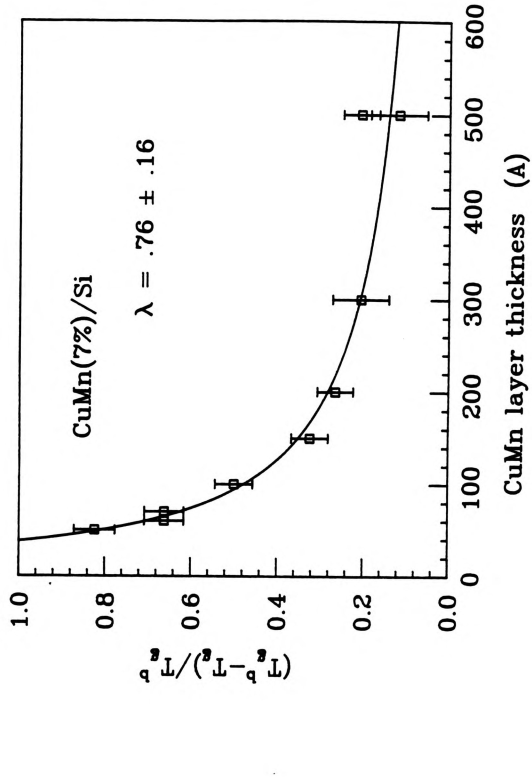

Figure IV-20: Fit of $\epsilon = \frac{T_g^b - T_g}{T_g^b}$ vs L_{CuMn} for $Cu_{.93}Mn_{.07}/Si$ MS.

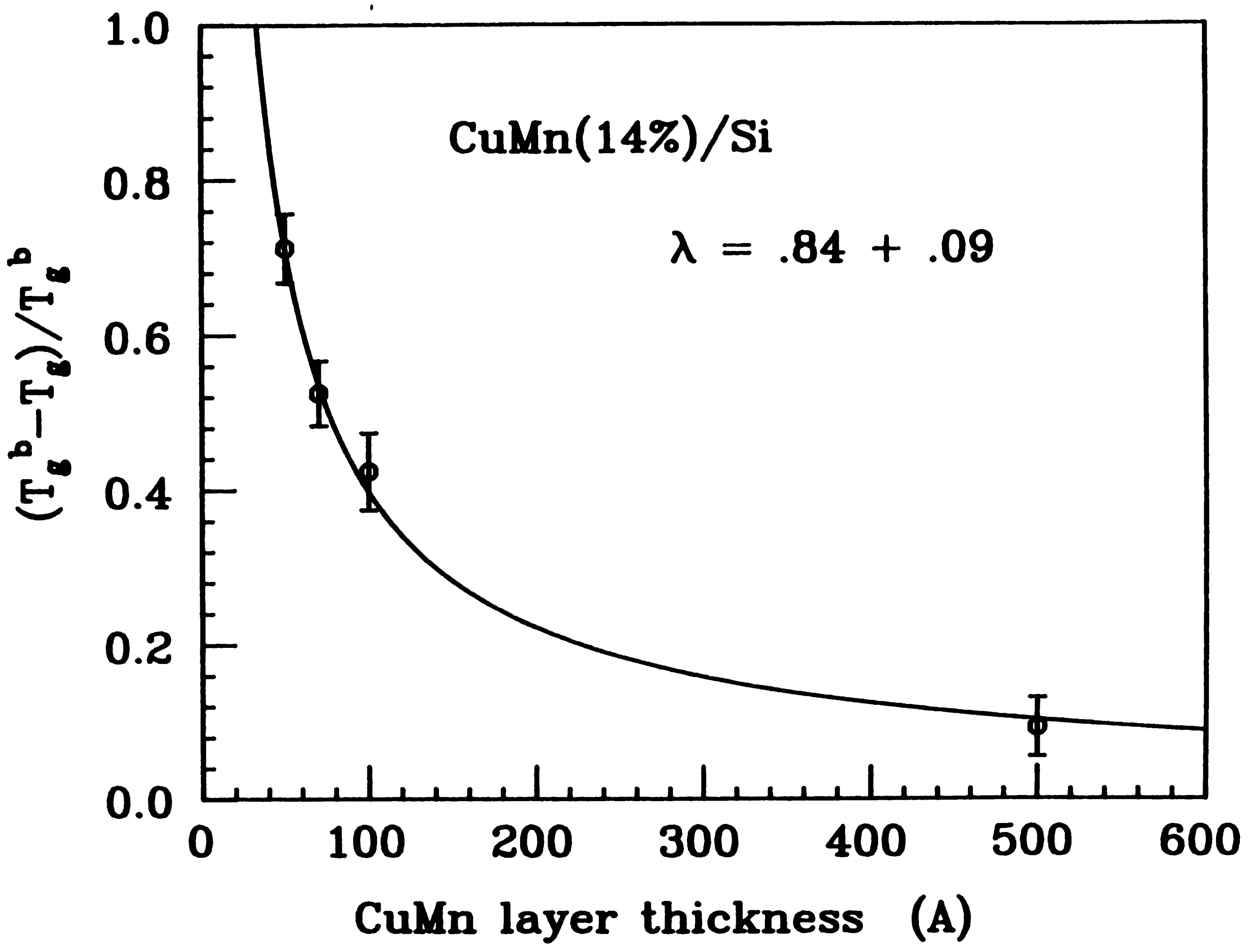

Figure IV-21: Fit of $\epsilon = \frac{T_g^b - T_g}{T_g^b}$ vs L_{CuMn} for $Cu_{.86}Mn_{.14}/Si$ MS.

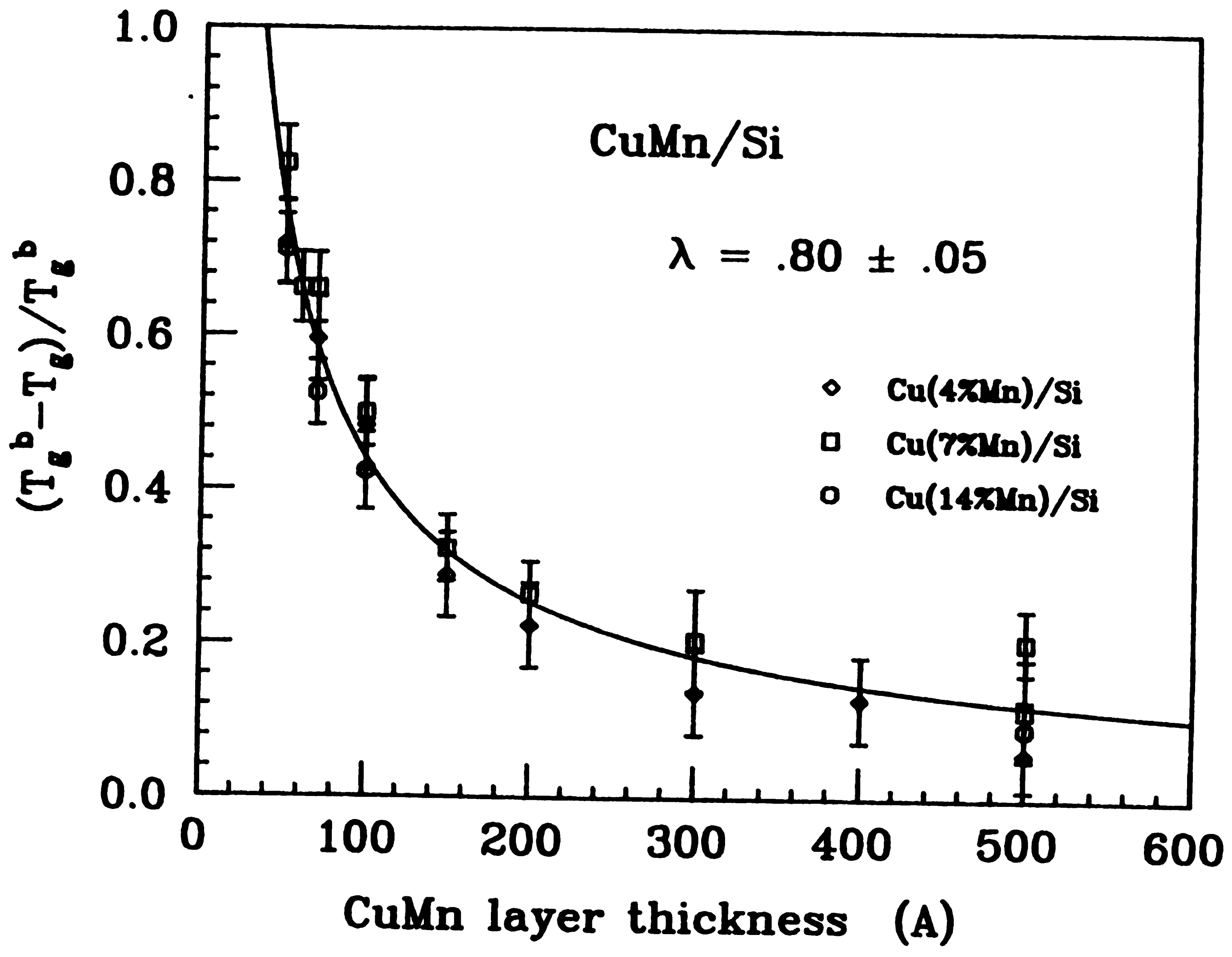

Figure IV-22: Fit of $\epsilon = \frac{T_g^b - T_g}{T_g^b}$ vs L_{CuMn} for all of the $CuMn/Si$ MS.

$$J_{RKKY}(R)^{damped} = J_{RKKY(R)}e^{-\alpha \frac{R}{l}}$$

where l is the mean free path of the conduction electrons, and α is a damping constant which goes to the de Gennes limit (Eq. III.3) for $\alpha = 1$. At this point in time no theoretical estimate of α exists.

The reduction in the layer thickness causes a reduction in the average number of impurity nearest neighbors, per impurity, as the layer thickness is decreased. When this boundary effect is incorporated into the UQM for a non damped RKKY interaction ($\alpha = 0$) it is seen to have negligible effect down to approximately 30 A^o, Fig. IV-23, 24, and 25. The transition temperature begins to decrease at this point and must approach zero as $L_{CuMn} \Rightarrow 0$.

Alternatively, setting $\alpha = 1$, the de Gennes limit, we find that mean free path effects (due to the increasing resistivity as L_{CuMn} decreases in the CuMn/Si MS) significantly reduce the transition temperature from the bulk value. The results of this damping are shown in Figs. IV-23, 24, and 25. These data shows that mean free path effects become significant below about 500 A^o but do not account for the entire decrease in T_g as a function of L_{CuMn}.

If we take the difference between the CuMn/Si data and the estimated reduction in Tg, due to mean free path effects the resulting data are found to fit to the CuMn/Cu data fairly closely (Fig. IV-26). The 4 and 14 percent CuMn/Si MS (with estimated mean free path effects subtracted out) are larger then the CuMn/Cu data in the samples with thinner L_{CuMn}, consistent with the assertion by Jagannathan et al.[71], that the de Gennes limit[69] is an over estimation of the effects of a reduced mean free path on the RKKY interaction.

IV.3) Magnetization vs. Magnetic Field

The magnetization vs. magnetic field was measured by W. Abdul-Razzaq[81] for

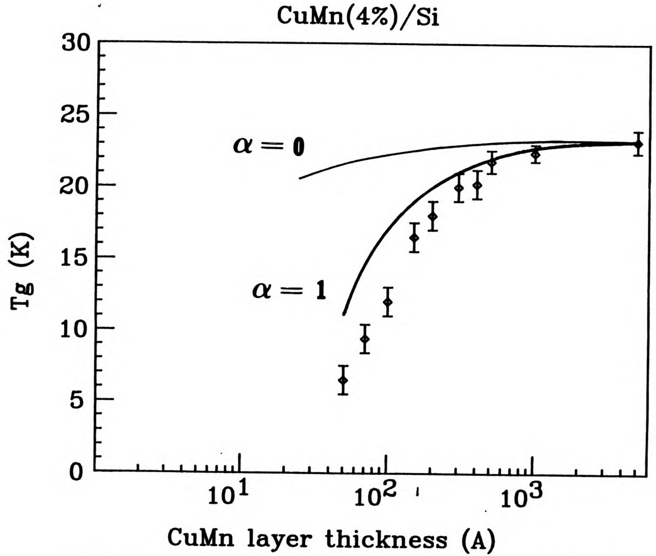

Figure IV-23: Transition temperature T_g vs CuMn layer thickness L_{CuMn} for the $Cu_{.96}Mn_{.04}/Si$ MS. $\alpha = 0$ corresponds to no mean free path effects. $\alpha = 1$ corresponds to mean free path effects.

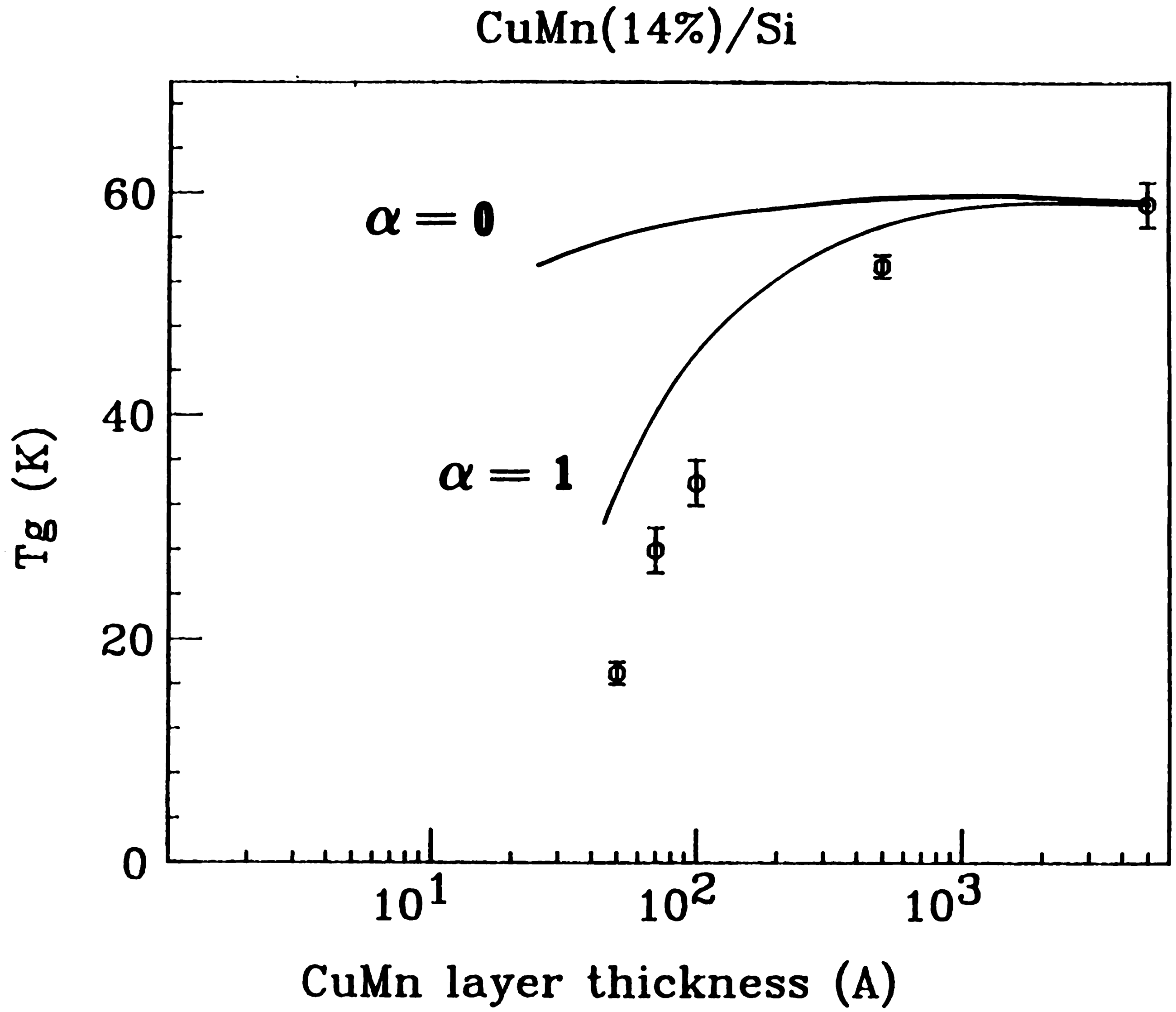

Figure IV-25: Transition temperature T_g vs CuMn layer thickness L_{CuMn} for the $Cu_{.86}Mn_{.14}$/ MS. $\alpha = 0$ corresponds to no mean free path effects. $\alpha = 1$ corresponds to mean free path effects.

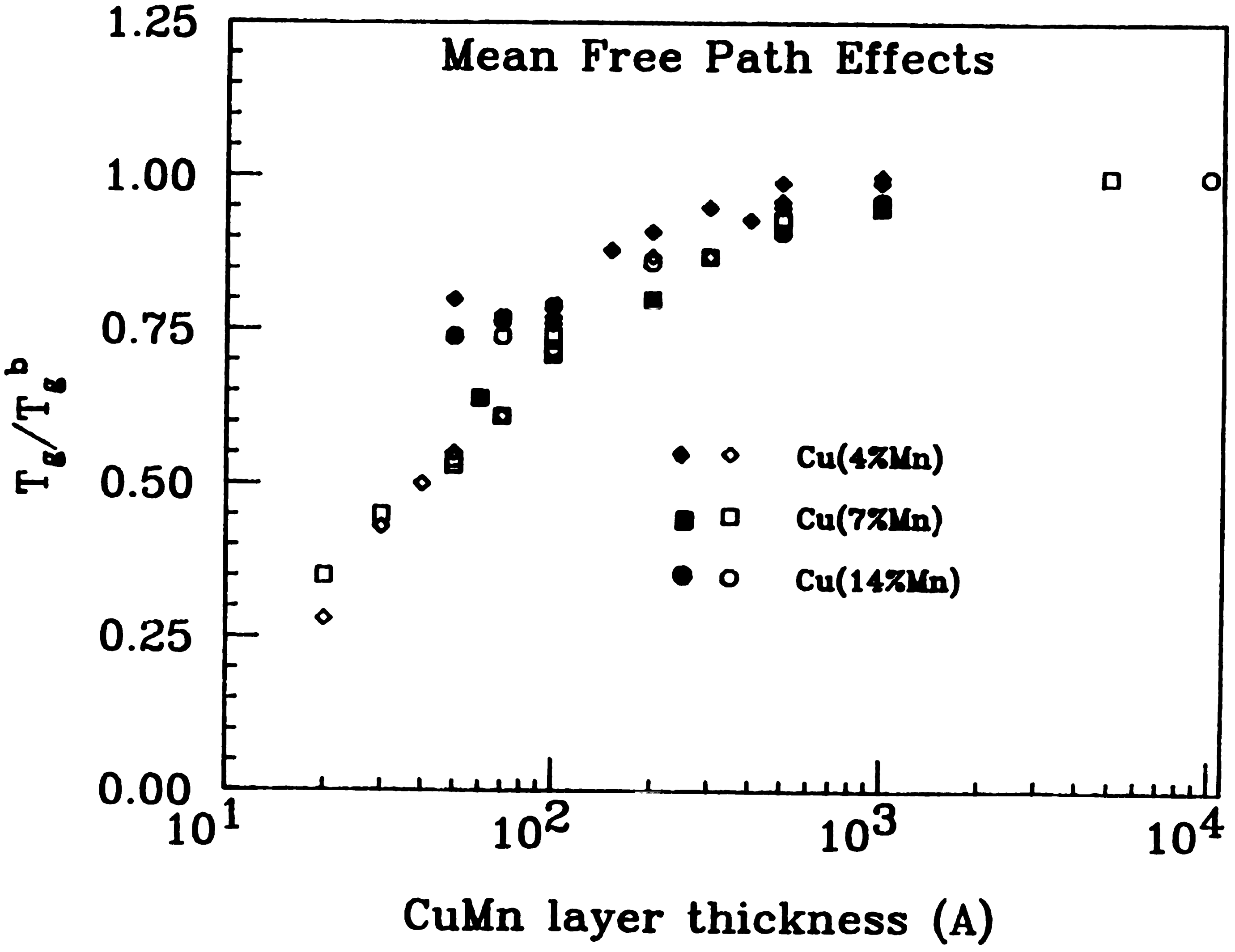

Figure IV-26: Normalized transition temperature $\frac{T_g}{T_g^b}$ vs CuMn layer thickness L_{CuMn} for all of the $CuMn/Cu$ MS (open symbols). The closed symbols correspond to CuMn/Si MS after correction for mean free path effects (see text).

various L_{CuMn} in our $Cu_{.93}Mn_{.07}/Si$ MS. The zfc magnetization of these samples were measured in fields up to 6kG. The magnetization was then measured in fields between 6kG and -6kG, and then in fields between -6kG and 0G. Although the maximum fields were not quite large enough to saturate the anisotropic fields (Abdul-Razzaq has estimated the saturation field of these samples to be ≈8kG) useful information can still be obtained from them.

After 'saturation' the magnetic field is reversed. At a negative field the magnetization displays a rapid reversal. This occurs at a field termed H_{sh}. Although true saturation has not occurred, H_{sh} should display behaviour qualitatively similar to the coercive field needed to flip all of the spins 180°. It is noticed (IV-27) that H_{sh} is finite for all samples measured. We infer from this that the layered samples are qualitatively similar to bulk CuMn (ie. have DM anisotropic interactions). The coercive (IV-28) field remains approximately constant (~ -2kG) down to $L_{CuMn} = 300\ A^{\circ}$ and then decreases rapidly down to a value of ~ -.3kG at $L_{CuMn} = 100\ A^{\circ}$. Abdul-Razzaq has interpreted the reduction in the the coercive field to be due to a reduction in the DM interaction.

IV.4) Universality

From the relationship $\lambda = \frac{1}{\nu}$ we have obtained a value of $\nu = 1.72 \pm .15$ From the exponents β and γ found directly from non-linear susceptibility experiments, Levy and Ogielski[11] deduced from the hyper scaling relationship, $d\nu = 2\beta + \gamma$, a value of $\nu = 1.3 \pm .1$, We expect the material they used (AgMn) to be in the same universality class as CuMn due to the similarities in the materials and their magnetic interactions. These values of ν compares well with values reported for Ising Model simulations (see III.1). Until recently, theoretical Heisenberg like systems in three dimensions have yielded only transition temperatures equal to zero, suggesting a lower critical dimension greater then three. In contrast the recent work by Reger and Young[7] includes the possibility of a non-zero transition temperature and sets a lower bound of $\nu > 2.3$. These simulations were done on small lattices $L^3_{CuMn} \leq 16^3$,

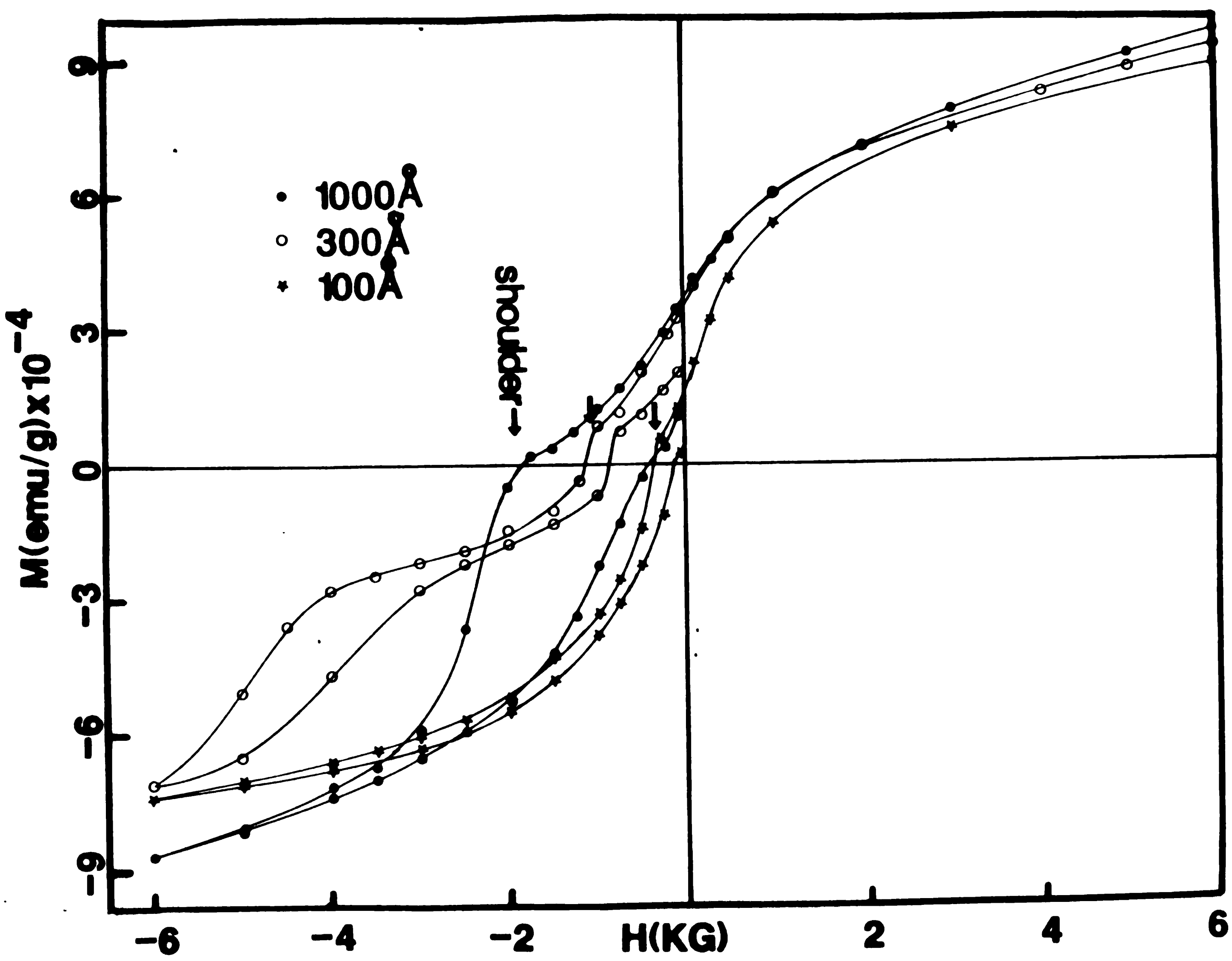

Figure IV-27: The magnetization vs magnetic field in $Cu_{.93}/Mn_{.07}/Si$ MS.

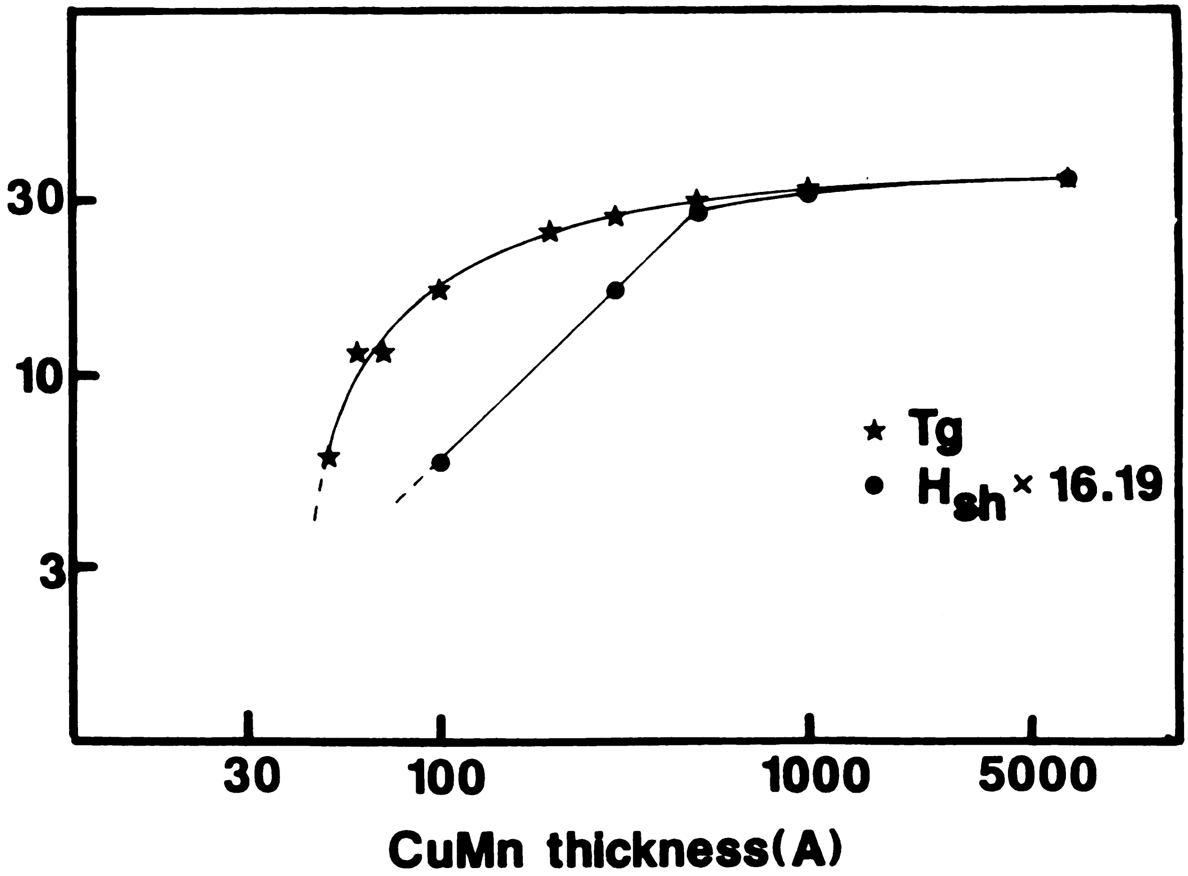

Figure IV-28: H_{sh} vs L_{CuMn} in $Cu_{.93}/Mn_{.07}/Si$ MS.

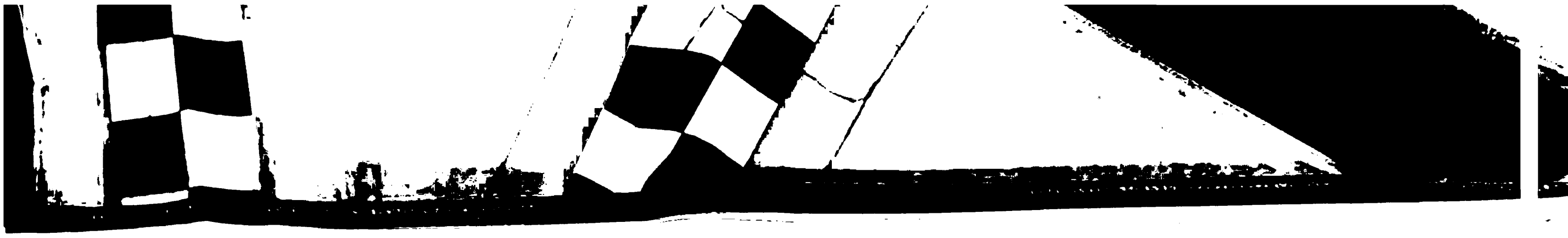

which may be too small for an accurate determination of ν. Walstead and Walker have found a non-zero transition temperature for Heisenberg systems with a dipolar anisotropy. This suggests the possibility that the anisotropy in the real materials causes them to belong to the same universality class as Ising spin glass systems. Levy and Ogielski[11] have also measured the susceptibility exponent, $\gamma = 2.1 \pm .1$, the order parameter exponent, $\beta = .9 \pm .2$, and the dynamic exponent $z\nu = 6 \pm .6$. These compare less well then ν with the values $\gamma = 2.9$[59], $\beta = .5$[59], and $z\nu = 6 \pm 1$[56], obtained from Monte Carlo simulations on Ising spin glasses. The comparison of CuMn with Ising spin glass models is therefore unclear and in need of more experimentation and larger scale simulations. A comparison of the other critical exponents (see Table III-1) should resolve the question; Which universality class does the CuMn spin glass transition belong?

CHAPTER V

CONCLUSIONS

V.1) Structure of Multilayer Systems

Using UHV sputtering we have produced $Cu_{1-x}Mn_x/Cu$ MS with $x = .04$, .07 and .14, and $Cu_{1-x}Mn_x/Si$ MS with $x = .04$, .07, .14 and .21. Imaging and EDX analysis of selected samples indicates chemical layering in both types of samples consistent with thicknesses programmed into the sputtering control system during sample preparation. Quantitative SAXD analysis of the CuMn/Si MS indicates bi-layer thicknesses within a few percent of programed bi-layer thicknesses. SAD, TEM imaging and high angle x-ray studies indicate that the CuMn layers in the CuMn/Si MS are composed of crystallites approximately half the diameter of the layer thickness in the thinner samples ($L_{CuMn} \leq 200\ A^o$) and saturating at a diameter of $\approx 300\ A^o$ in the thickest samples. In contrast, we infer from the lack of superlattice lines in the high angle x-rays, and the lack of observed crystallites in the TEM images that the Si layers are amorphous. The resistivities of the CuMn/Si MS indicate that some Si is entering into the CuMn layers, probably at the grain boundaries. Resistivities of the CuMn/Cu MS support a layered geometry with minimal diffusion of Mn into the Cu interlayer.

V.2) Susceptibility and T_g

We have measured the zero field cooled (zfc) and field cooled (fc) susceptibility curves of all of our samples from 5 K to about 100 K. All zfc and fc susceptibilities show behaviour typical of spin glasses. The susceptibility measurements coupled with the low T ($T << T_g$) hysteresis curves indicate that the CuMn layers in our samples remain spin glass-like to $L_{CuMn} = 20\ A^o$. Following convention we have defined the peak in the zfc susceptibility to be the spin glass transition temperature T_g. We observe, for all concentrations and for both the Cu and Si interlayers, that this transition temperature decreases systematically with decreasing L_{CuMn}. This reduction in T_g begins at layer thicknesses as large as 1000 A^o and apparently goes to zero at $L_{CuMn} \approx 12\ A^o$ in the CuMn/Cu MS and $L_{CuMn} \approx 36\ A^o$ in the CuMn/Si MS. Above T_g absolute values of the fc susceptibility in the CuMn/Cu MS appear to follow similar Curie-like behaviour. Scaling the measured transition temperature T_g^L by the appropriate bulk transition temperature T_g^b we observe that all of the different concentration CuMn/Cu samples follow similar behaviour. This is also true, separately, for the CuMn/Si MS.

V.3) Comparison with Scaling Theory

For each interlayer, we can fit the reduced temperature

$$\epsilon = \left(\frac{T_g^b - T_g^b}{T_g^b}\right) \sim AL_{CuMn}^{-\lambda},$$

over the whole length scale studied. We find values of λ consistent with each other, for all values of x, for a common interlayer. By fitting all of the data for a given interlayer, we obtain values of $\lambda = ..58 \pm .05$ for the CuMn/Cu MS and $\lambda = .8 \pm .05$ for the CuMn/Si MS. The value of the correlation exponent $\nu = 1.72 \pm .15$ obtained through the scaling relation $\lambda = \frac{1}{\nu}$ is compared with the value of $\nu = 1.3 \pm .2$ obtained by Levy and Ogielski from non-linear susceptibility measurements on AgMn.

Within experimental resolution, no change is noticed in the widths of the normalized

zfc peaks, as predicted by finite size scaling theory. Fisher and Huse suggest that finite size scaling should only be valid in the thickest CuMn samples. Applying finite size scaling analysis to CuMn/Cu MS for $L_{CuMn} > 200\ A^o$ we obtain a value of $\lambda = 1.1 \pm .3$ For thinner samples Fisher and Huse predict that the apparent freezing temperature should scale like

$$\frac{T_f(t_m)}{T_g} \sim \left[\frac{L^{\psi_3+\psi_2\nu_2\theta_3}}{ln(t_{exp})}\right]^{\frac{1}{1+\nu_2\psi_2}} .$$

Fitting our data to this form for CuMn/Cu MS with $L_{CuMn} \leq 200\ A^o$ (assuming t_m constant) we obtain a value of

$$\frac{\psi_3 + \psi_2\nu_2\theta_3}{1 + \nu_2\psi_2} = .38 \pm .03 .$$

V.4) Conclusions As we thin down CuMn layers in MS samples, we find that the spin glass transition temperature T_g decreases and apparently approaches zero as the system approaches two dimensions. We believe that this is the first experimental evidence that the Lower Critical Dimension of this universality class of transition is between two and three. The data is generally consistent with finite size scaling theory and we have obtained a value of the critical exponent λ.

REFERENCES

1. See for example: **Phase Transitions and Critical Phenomena**, Vol. 1-12, Ed. Domb and Green,

2. Brout, R. H.: **Phase Transitions**, W. A. Benjamin (1965)

3. Morrish, A.H.: **The Physical Principals of Magnetism**, John Wiley Sons, Inc., (1965).

4. Cannella, V. and J.A. Mydosh: Phys. Rev. B **6**, 4220, (1965).

5. Binder, K. and A.P. Young: Rev. Mod. Phys. **58**, 4, 801, (1986).

6. Kac, M.: **Statistical Physics Phase Transitions and Superfluidity**, vol.1 Gordon and Breach Pub., (1963)

7. Reger, J.D. and A.P. Young: Phys. Rev. B **37**, 10, 5493, (1987).

8. Mydosh J.A.: J. Mag. Mag. Mat. **7**, 237 (1978)

9. Kondo, J.: J. Appl. Phys. **37**, 1117, (1986).

10. Ruderman, M.A., and C. Kittel: Phys. Rev. **96**, 99 (1954).

11. Levy L.P. and A.T. Ogielski: Phys. Rev. Lett. **57**, 26, 3288 (1986).

12. Vogt, E.: **Magnetism and Metallurgy**, Vol. 1, Ed. H. E. Berkowitz and E. Kneller, Acedemic Press, (1969)

13. Bouchart, H. and E. Daryge: J. Physique **43**, 1699, (1982).

14. Levin, K. C.M. Soukoulis, G.S. Grest: J. Appl. Phys. **50**, 3, 1695, (1979).

15. Erickson, R. A.,: Phys. Rev. **90**, 779 (1953)

16. Werner, S.A., J.J. Rhyne, J.A. Gotes: Soild State Comm.**50**, 5, 457, (1985).

17. Cable, J.W., S.A. Werner, G.P. Flecher: Phys. Rev. B **29**, 3, 1268, (1984).

18. Algra, H.A., L. DeJongh and J. Reedijk: Phys. Rev. Lett **42**, 606, (1979).

19. Ford, P.J. and J.A. Mydosh: Phys. Rev. B **14**, 5, 2057 (1976).

20. Mezei F. and A.P. Murani: J. Magn. Magn. Matter **14**, 211, (1979).

21. Mezel, F.: **Recent Developments in Condensed Matter Physics**, Vol. 1, Plenum, 679 (1981).

22. Lauer. J., W. Keune, T. Shigematsu: **Recent Developments in Condensed Matter Physics 2**, Plenum, (1981).

23. Uemura, Y.J. and T. Yamazaki: Physica **109**, 110B, C, 1915 (1982).

24. Heffner, R.H., M. Leon and D.E. MacLaughlin: **Hyperfine Interactions**, 18, 457, (1984).

25. Malozemoff, A.P. and Y. Imrg: Phys. Rev. B **24**, 489, (1981).

26. Bouchiat, H. and P. Monod: J. Magn. Magn. Matter **30**, 175, (1983).

27. Beck, P.A.: Prog. Mater, Sci. **23**, 1, (1978).

28. Awchalom, D. D., J. M. Hong, L.L. Chang, G. Grinstein: Phys. Rev. Lett. **59**, 1733 (1987)

29. S. Jackson: private communication

30. Sherrington, D.: Proc. of Heidolber Col. on Glass Dynamics and Optimization. (1986).

31. Walker, L.R. and R.E. Walstead: J. Magn. Magn. Mater. **31-34**, 1289, (1983).

32. Dzyaloshinskii, I.E.: J. Phys. Chem. Soilds 4, 241, (1958).

33. Moriya, T.: Phys. Rev. Lett. 4, 51, (1960).

34. Prejean, J.J., M.J. Joliclerc and P. Monod: J. Phys. (Paris) **41**, 427 (1980)

35. Ising, E.: Ph.D. Thesis (1925)

36. M^{c}Coy, B.M., and T. T. Wu: **The Two Dimensional Ising Model**, Harvard University Press (1983)

37. Onsager, L.: Phys. Rev. **65**, 3 and 4, 117 (1944)

38. Hofer, W.O.: **Erosion and Growth of Solids Stimulated by Atom and Ion Emission**, Martinus Nijhoff Publishers (1986).

39. Slaughter, J: Ph.D. Thesis, Michigan State University (1988).

40. Fischer, K.H.: Landolt Bornstein Tables **15**, 289, (1982) (and references therein).

41. Handbook of Chemistry and Physics **56**, CRC Press (1976).

42. Sigmund, P.: Phys. Rev. **184**, 2, 383 (1969).

43. Watt, I: **The Principles and Practice of Electron Microscopy**, Cambridge Univ. Press (1985)

44. Thomas, G., and M. Goringe: **Transmission Electron Microscopy of Materials**, John Wiley and Sons, Inc., (1979)

45. Slaughter, J.: private communication.

46. Sheng, T.T., and R.B. Marcus: preprint

47. van de Pauw, L. J.: Philips Res. Rep. **13**, 1, 1 (1958)

48. Sondheimer, E.H.: Phil. Mag. **1**, 1, 1 (1952).

49. Vraken, J. C. Van Haesendonck, and Y. Brugnserazede: Proc. 18th Int. Conf. on Low Temp. Phys., Jap. J. Appl. Phys. **26**, Suppl. 26-3, 777 1987.

50. Van Haesendonck, C., L. Van den dries and Y. Brunsereade: Phys. Rev. B **25**, 8, 5090 (1982)

51. Edwards, S.F., and P.W. Anderson: J. Phys. F, 965 (1975).

52. Sherington, D., and S. Kirkpatrick: Phys. Rev. Lett. **A 62**, 1972 (1975).

53. Fisher, M.E.: **Advanced Course on Critical Phenomena**, Lecture Notes (1982).

54. Fisher, D.S., and D.A. Huse: Phys. Rev. B **36**, 16, 8937 (1987).

55. Marshall, W.: Phys. Rev. **118**, 1519 (1960).

56. Ogielski, O.T., and I. Morgenstein: Phys. Rev. Lett. **54**, 9, 928 (1985).

57. McMillan, W.L.: Phys. Rev. B **31**, 340 (1985).

58. Bray, A., and M.A. Moore: Phys. Rev. B **31**, 631 (1985).

59. Bhatt, R.N., and A.P. Young: Phys. Rev. Lett. **54**, 9, 924 (1985).

60. Southern B.W., and A.P. Young: J. Phys. **C 10**, 2179 (1977).

61. Anderson P.W. and C.W. Pond: Phys. Rev. Lett. **40**, 903 (1978).

62. Fisch R., and A.B. Harris: Phys. Rev. Lett. **38**, 785 (1977).

63. Chakrabarti, A., and C. Dasgupta: Phys. Rev. Lett. **56**, 1404 (1986).

64. Bray, A.J., M.A.Moore and A. P. Young: Phys. Rev. Lett. **56**, 24, 2641 (1986)

65. Larsen, U.: Phys. Rev. B **33**, 7, 4803 (1986).

66. Kasuya, T.: Prog. Theoret. Phys. **16**, 45 (1956).

67. Yosida, K.: Phys. Rev. **106**, 5, 893 (1957).

68. Zhang, Q., and P.M. Levy: Phys. Rev. B **34**, 3, 1884 (1986).

69. deGennes, P.F.: J. Phys. Radium **23**, 630 (1962)

70. Vier, D.C., and S. Schultz: Phys. Rev. Lett. **54**, 150 (1985).

71. Jagannathan, A., E. Abrahams, and M.J. Stephen: Phys. Rev. B **37**, 1, 436 (1988).

72. Kittel, C.: **Introduction to Solid State Physics**, 5^{th} ed., John Wiley and Sons (1980)

73. Sienko M.J.: J. Chem. Phys. **53**, 566 (1970).

74. Widom, B.: **Fundamental Problems in Statistical Mechanics**, Vol. III

Ed. E. V. G. Cohen, North Holland (1975)

75. Barber, M.N.: in **Phase Transitions and Critical Phenomena**, edited by C. Domb and J.L. Lebowitz, Academic Press, Vol. 8, 145 (1983).

76. Fisher, M.E. and A. E. Ferdinand: Phys. Rev. Lett. **19**, 169 (1967)

77. Dekker, C., A.F.M. Arts, and H.W. deWijn: To be published, Phys. Rev. B (1988).

78. Nagata, S., P. H. Keesom and H. R. Harrison: Phys. Rev. B **19**, **3**, 1633 (1979)

79. Aeppli, G., J. J. Hauser, G. Shirane and Y. J. Uemura: Phys. Rev. Lett. **54**, 8, 843 (1985)

80. Moorjani, K. and J. Coe: **Magnetic Glasses**, 299, E. Sevier, (1984).

81. Abdul-Razzaq, W: To be published.

APPENDIX A.1

3D RKKY INTERACTION

The RKKY interaction is an indirect interaction between two magnetic ions with moments $\mathbf{I_i}$ and $\mathbf{I_j}$. These ions are placed in a metal sufficiently far apart so that their local electronic wavefunctions do not overlap. The ions are coupled via the conduction band electrons which have a spin monent **S**. The interaction is therefore calculated as a second order perturbation calculation with the sum over conduction band states. $\Delta_{k'k}$ is the overlap matrix element between conduction band states **k** and $'k$. The second order perturbation expansion is:

$$J(R_{ij}) = -(\mathbf{S}\cdot\mathbf{I_i})(\mathbf{S}\cdot\mathbf{I_j})\int_0^{k_F}\frac{d\mathbf{k}}{(2\pi)^3}\int_{k_F}^{\infty}\frac{d\mathbf{k}'}{(2\pi)^3}\frac{\Delta_{kk'}\,\Delta_{k'k}e^{i(\mathbf{k}-\mathbf{k}')\cdot\mathbf{R_{ij}}}}{E(\mathbf{k}')-E(\mathbf{k})}$$

In a free electron model the fermi surface is spherical. The above integrations can therefore be done in a spherical geometry.

$$= -\frac{\mathbf{I_i}\cdot\mathbf{I_j}\,|\Delta_{kk'}|^2}{(2\pi)^6}\int_0^{k_F}\int_0^{2\pi}\int_0^{\pi} e^{ikRcos\theta}sin\theta d\theta\ d\phi\ k^2dk$$

$$\cdot\quad\int_{k_F}^{\infty}\int_0^{2\pi}\int_0^{\pi}\frac{e^{-ik'Rcos\theta'}sin\theta'}{E(\mathbf{k}')-E(\mathbf{k})}d\theta'd\phi'k'^2dk'$$

The integration over ϕ is trivial.

$$Q = \int_0^{2\pi}\int_0^{\pi} e^{ikRcos\theta}sin\theta d\phi = 2\pi\int_0^{\pi} e^{i}kRcos\theta sin\theta d\theta$$

The integration over the θ of Eq. A-1 can be done by substitution. Letting $u = ikRcos\theta$, $du = -ikRsin\theta d\theta$ and doing the integration we obtain

$$Q = \frac{i2\pi}{kR}\left[\int_0^{k_F} e^{-ikR}k^2dk - \int_0^{k_F} e^{ikR}k^2\ dk\right]$$

Take the first integral $\int_0^{k_F} e^{-ikR}kdk$ and let $k^1 = -k$

$$\Rightarrow \int_0^{k_F} e^{ik^1dk^1}$$

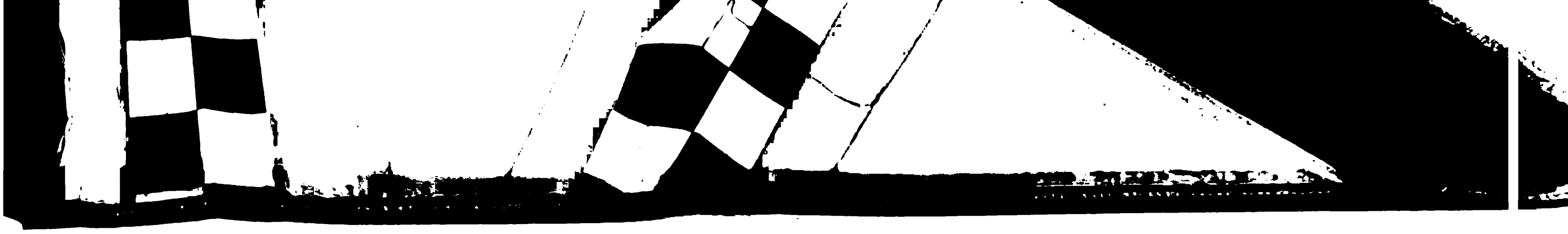

$$\Rightarrow -\int_{-k_F}^{0} e^{ikR}kdk$$

$$= \frac{-2\pi i}{R}\int_{-k_F}^{k_F} e^{ikR}kdk$$

Therefore Eq. A-1 becomes

$$J(R_ij = -\frac{\mathbf{I_i}\cdot\mathbf{I_j}\;|\Delta_{kk'}|^2}{(2\pi)^4R_{ij}^2}\int_{-k_F}^{k_F} e^{ikR_{ij}}\;kdk\int_{-\infty}^{k_F}\int_{k_F}^{\infty}\frac{e^{-ik'R_{ij}}}{E(\mathbf{k}')-E(\mathbf{k})}k'dk'$$

Using the argument of RK[10] this becomes

$$J(R_{ij}) = -\frac{\mathbf{I_i}\cdot\mathbf{I_j}\;|\Delta_{kk'}|^2}{(2\pi)^4R_{ij}^2}\int_{-k_F}^{k_F} e^{ikR_{ij}}\;kdk\left[\int_{-\infty}^{\infty}\frac{e^{-ik'R_{ij}}}{E(\mathbf{k}')-E(\mathbf{k})}k'dk'\right]$$

In a free electron model $E(k) = \frac{h^2k^2}{2m}$. Therefore we obtain

$$J(R_{ij}) = -\frac{\mathbf{I_i}\cdot\mathbf{I_j}\;|\Delta_{kk'}|^2 2m}{(2\pi)^4R_{ij}^2h^2}\int_{-k_F}^{k_F} e^{ikR_{ij}}\;kdk\left[\int_{-\infty}^{\infty}\frac{e^{-ik'R_{ij}}}{k'^2-k^2}k'dk'\right]$$

The integral in brackets can be evaluted by using the identity

$$\frac{1}{k'^2-k^2} = \frac{1}{2k}\left[\frac{1}{k'-k}-\frac{1}{k'+k}\right]$$

$$\int_{-\infty}^{\infty}\frac{e^{-ik'R_{ij}}}{k'^2-k^2}k'dk' = \frac{1}{2k}\int_{-\infty}^{\infty}\frac{e^{-ik'R_{ij}}}{k'-k}k'dk' - \frac{1}{2k}\int_{-\infty}^{\infty}\frac{e^{-ik'R_{ij}}}{k'+k}k'dk'$$

Evaluate the first integral by letting $z = k'R_{ij}$

$$\int_{-\infty}^{\infty}\frac{e^{-ik'R_{ij}}}{k'-k}k'dk' = \frac{1}{R}\int_{-\infty}^{\infty}\frac{e^{-iz}}{z-kR}zdz$$

Jordan's Lemma states that the line integral around an analytic region in the complex plane is zero (ie. $\int\ = 0$) Therefore

$$\int\ \frac{e^{-iz}}{z-kR}zdz = \int_{C_2}\frac{e^{-iz}}{z-kR}zdz + P\int_{-\infty}^{\infty}\frac{e^{-iz}}{z+kR}zdz$$

where P is the principal part of the integral.

$$P\int_{-\infty}^{\infty}\frac{e^{iz}}{z-kR}zdz=-\pi ie^{iz}z\Big|_{kR}=\pi ie^{ikR}(kR)$$

$$P\int_{-\infty}^{\infty}\frac{e^{iz}}{z+kR}zdz=\pi ie^{iz}z\Big|_{-kR}=-\pi ie^{-ikR}(kR)$$

Therefore

$$\int_{-\infty}^{\infty}\frac{e^{-ik'R_{ij}}}{k'+k}k'dk'=\frac{-\pi}{2}(e^{ikR}-e^{-ikR})$$

and

$$\frac{\pi i}{2}\left[\int_{-k_F}^{k_F}e^{2ikR}kdk-\int_{k_F}^{k_F}kdk\right]=\frac{\pi i}{2}\int_{-k_F}^{k_F}e^{2ikR}kdk$$

$$=\frac{\pi i}{2}\left[\frac{ke^{2ikR}}{(2iR)}-\frac{e^{2ikR}}{(2iR)^2}\right]_{-k^F}^{k_F}=\frac{\pi}{2}\left[\frac{kcos(2kR)}{4}-\frac{sin(2kR)}{8R}\right]_{k_F}^{k_F}$$

$$=\frac{\pi}{4R}\left[2k_Fcos(2k_FR-\frac{\pi sin(2k_FR)}{R}\right]$$

Therefore the RKKY interaction in 3D is:

$$=J(R_{ij})=-\frac{\mathbf{I_i}\cdot\mathbf{I_j}\;|\Delta_{kk'}|^2}{(2\pi)^3R_{ij}^4}\frac{m}{4h^2}\left[2k_Fcos(2k_FR_{ij})-\frac{\pi sin(2k_FR_{ij})}{R_{ij}}\right]$$

APPENDIX A.2

2D RKKY INTERACTION

The following is a derivation for the RKKY interaction in a metal with a two dimension conduction band. The sum in the second order perturbation expansion is now over a two dimensional fermi surface.

$$J(R_{ij}) = -(\mathbf{S}\cdot\mathbf{I_i})(\mathbf{S}\cdot\mathbf{I_j})\int_0^{k_F}\frac{d\mathbf{k}}{(2\pi)^2}\int_{k_F}^{\infty}\frac{d\mathbf{k}'}{(2\pi)^2}\frac{\Delta_{kk'}\;\Delta_{k'k}e^{i(\mathbf{k}-\mathbf{k}')\cdot\mathbf{R_{ij}}}}{E(\mathbf{k}')-E(\mathbf{k})}$$

$$= -\frac{\mathbf{I_i}\cdot\mathbf{I_j}\;|\Delta_{kk'}|^2}{(2\pi)^4}\int_0^{k_F}\int_0^{2\pi}e^{ikRcos\theta}d\theta\;k^2dk\int_{k_F}^{\infty}\int_0^{2\pi}\frac{e^{-ik'Rcos\theta'}}{E(\mathbf{k}')-E(\mathbf{k})}d\theta' k'^2dk'$$

The integral over θ is a Bessel function:

$$J_o(z) = \frac{1}{2\pi}\int_0^{2\pi}e^{-kRcos\theta}d\theta$$

Therefore

$$J(R_{ij}) = -\frac{\mathbf{I_i}\cdot\mathbf{I_j}\;|\Delta_{kk'}|^2 2m}{(2\pi)^2h^2}\int_0^{k_F}J_o(kR)k^2dk\int_{k_F}^{\infty}\frac{J_o(k)}{k'^2}-k^2dk'$$

Using the asymptotic expansion for $J_o(k'R)$ for $kR >> 1$

$$J_o(x) = \sqrt{\frac{2}{\pi x}}cos(x-\frac{\pi}{4})$$

.

$$J(R_{ij}) = -\frac{\mathbf{I_i}\cdot\mathbf{I_j}\;|\Delta_{kk'}|^2 2m}{(2\pi)^2h^2}\sqrt{\frac{2}{\pi}}\int_0^{k_F}J_o(kR)k^2dk\int_{k_F}^{\infty}\frac{cos(k'-\frac{\pi}{4}\sqrt{k'}}{\sqrt{R}k')-k}k'^2dk'$$

This expression was analyzed numerically. The results are plotted in Fig. A-1. The RKKY interaction in 2D is found to decay as $J(R) \sim \frac{1}{R^2}$.

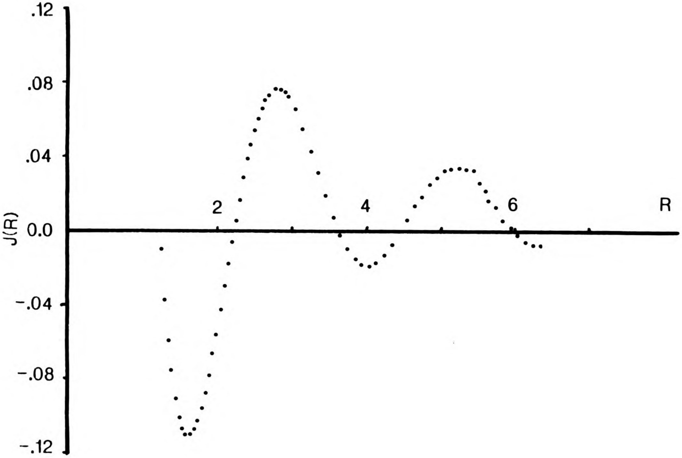

FIGURE A-1: 2D RKKY interaction as a function of radial distance.